Ultra-Fast Photonic Signal Processors Based On Photonic Integrated Circuits

Weilin Liu

A Thesis submitted in partial fulfillment of the requirements for the Doctoral in Philosophy degree in Electrical and Computer Engineering

Ottawa-Carleton Institute of Electrical and Computer Engineering
School of Electrical Engineering and Computer Science
University of Ottawa

uOttawa

ACKNOWLEDGEMENTS

First of all, I would like to express my great gratitude to my thesis advisor, Professor Jianping Yao, for providing me with excellent research environment, valuable directions and delicate guidance throughout this research work. His meticulous scholarship impresses me. His great passion towards scientific research work inspires me to work hard. His rich knowledge has made him as a constant source of ideas. Without his encouragement and patience, this work would have never been finished.

I would also like to thank the present and former colleagues in the Microwave Photonics Research Laboratory: Bruno Romeira, Chao Wang, Honglei Guo, Hiva Shahoei, Jiejun Zhang, Ming Li, Wangzhe Li, Weifeng Zhang, and Xiang Chen; and the colleagues from the University of California, Santa Barbara: Erik J. Norberg, Prof. Larry A. Coldren, Robert S. Guzzon, and John S. Parker. Their strong supports and generous help greatly improved my research work. The memory of working with them is one of the precious treasures in my life.

Finally I am greatly indebted to my beloved family: my father Fanping Liu, my mother Suying Zuo, my sister Yihua Liu, my wife Zhi Li. They have always been the biggest support, physically and mentally, to my life and study.

TABLE OF CONTENTS

LIST OF ACRONYMS

A

ADC	analog-to-digital conversion
ASE	amplified spontaneous emission

C

CMOS	complementary metal-oxide-semiconductor
CTL-OQW	confinement tuning layer offset quantum well

D

DLP	discrete layer peeling
DSB	double-sideband
DSP	digital signal processing

E

EMI	Electromagnetic interference
EO	Electrical optical

F

FBG	Fiber Bragg grating
FHT	fractional Hilbert transformer
FP	Fabry-Pérot
FPGA	field-programmable gate array
FSR	increasing free spectral range
FWHM	full-width at half-maximum

I

InP	Indium phosphide

L

LCFBG	linearly chirped fiber Bragg grating
LPFG	long-period fiber grating
LTI	linear time-invariant

M

MLL	mode-locked laser
MMI	multi-mode interference
MZI	Mach-Zehnder interferometer

O

OSA	optical spectrum analyzer
OTDM	optical time division multiplexed

P

PC	polarization controller
PD	photodetector

PIC	photonic integrated circuit
PM	phase modulator
PMD	polarization mode dispersion
PSP	photonic signal processing

Q

QW	quantum well

R

RoF	radio-over-fiber

S

SMU	source measurement unit
SOA	semiconductor amplifiers
SOI	silicon-on-insulator
SOS	silica-on-silicon
SSB	single-sideband

T

TBWP	time-bandwidth product
TC	tunable couplers
TEC	thermoelectric cooler
TPS	temporal pulse shaping

W

WDM	wavelength division multiplexing

LIST OF FIGURES

Number *Page*

ABSTRACT

Photonic signal processing has been considered a promising solution to overcome the inherent bandwidth limitations of its electronic counterparts. Over the last few years, an impressive range of photonic integrated signal processors have been proposed with the technological advances of III-V and silicon photonics, but the signal processors offer limited tunability or reconfigurability, a feature highly needed for the implementation of programmable photonic signal processors.

In this thesis, tunable and reconfigurable photonic signal processors are studied. Specifically, a photonic signal processor based on the III-V material system having a single ring resonator structure for temporal integration and Hilbert transformation with a tunable fractional order and tunable operation wavelength is proposed and experimentally demonstrated. The temporal integrator has an integration time of 6331 ps, which is an order of magnitude longer than that provided by the previously reported photonic integrators. The processor can also provide a continuously tunable fractional order and a tunable operation wavelength.

To enable general-purpose signal processing, a reconfigurable photonic signal processor based on the III-V material system having a three-coupled ring resonator structure is proposed and experimentally demonstrated. The reconfigurability of the processor is achieved by forward or reverse biasing the semiconductor optical

amplifiers (SOAs) in the ring resonators, to change the optical geometry of the processor which allows the processor to perform different photonic signal processing functions including temporal integration, temporal differentiation, and Hilbert transformation. The integration time of the signal processor is measured to be 10.9 ns, which is largely improved compared with the single ring resonator structure due to a higher Q-factor. In addition, 1st, 2nd, and 3rd of temporal integration operations are demonstrated, as well as a continuously tunable order for differentiation and Hilbert transformation. The tuning range of the operation wavelength is 0.22 nm for the processor to perform the three functions.

Compared with the III-V material system, the CMOS compatible SOI material system is more cost effective, and it offers a smaller footprint due to the strong refractive index contrast between silicon and silica. Active components such as phase modulators (PMs) can also be implemented. In this thesis, two photonic temporal differentiators having an interferometer structure to achieve active and passive fractional order tuning are proposed and experimentally demonstrated. For both the active and passive temporal differentiators, the fractional order can be tuned from 0 to 1. For the active temporal differentiator, the tuning range of the operation wavelength is 0.74 nm. The use of the actively tunable temporal differentiator to perform high speed coding with a data rate of 16 Gbps is also experimentally demonstrated.

LIST OF PUBLICATIONS

For all publications if listed as the first author, I conceived the original idea, designed and implemented the experiment demonstration, processed and analyzed the experimental data, and generated the text and figures. Prof. Yao supervisor provided important suggestions and comments on the proposal and publication manuscript. Other contributing authors participated the related discussions and provided valuable suggestions.

A. Publications Directly Used in the Thesis

Chapter 4

1. **W. Liu**, M. Li, R. S. Guzzon, E. J. Norberg, J. S. Parker, L. A. Coldren, and J. P. Yao, "A photonic temporal integrator with an ultra-long integration time window based on an InP-InGaAsP integrated ring resonator," *J. Lightw. Technol.*, vol. 32, no. 20, pp. 3654-3659, Oct. 2014.
2. **W. Liu**, M. Li, R. S. Guzzon, E. J. Norberg, L. A. Coldren, and J. P. Yao, "A photonic integrated fractional Hilbert transformer with continuous tunability," Optical Fiber Communication Conference (OFC) 2014, Tu2A, 8-14 Mar. 2014, San Francisco, California, USA.

Chapter 5

3. **W. Liu**, M. Li, R. S. Guzzon, E. J. Norberg, J. S. Parker, M. Lu, L. A. Coldren, and J. P. Yao, "A fully reconfigurable photonic integrated signal processor," ***Nature Photon.***, vol. 10, no. 3, pp. 190-195, Mar. 2016.

Chapter 6

4. **W. Liu** and J. P. Yao, "Silicon-based integrated tunable fractional order photonic temporal differentiators," *J. Lightw. Technol.*, vol. 35, no. 12, pp. 2487-2493, May 2017.

B. Other Publications

Journal Papers:

[1] **W. Liu**, M. Li, R. S. Guzzon, E. J. Norberg, J. S. Parker, M. Lu, L. A. Coldren, and J. P. Yao, "A photonic integrated parity-time symmetry wavelength-tunable single-mode microring laser," *Nature Comm.*, 15389, May 2017.

[2] **W. Liu**, B. Romeira, M. Li, R. S. Guzzon, E. J. Norberg, J. S. Parker, L. A. Coldren, J. P. Yao, "A wavelength tunable optical buffer based on self-pulsation in an active microring resonator," *IEEE/OSA J. Lightw. Technol.*, vol. 34, no. 14, pp. 3466-3472, Jul. 2016.

[3] X. Han, E. Xu, **W. Liu**, and J. P. Yao, "Tunable dual-passband microwave photonic filter using orthogonal polarization modulation," *IEEE Photon. Technol. Lett.*, vol. 27, no. 20, pp.2209-2212, Oct. 2015.

[4] W. Zhang, N. Ehteshami, **W. Liu**, and J. P. Yao, "Silicon-based on-chip electrically tunable sidewall Bragg grating Fabry–Perot filter," *Opt. Lett.*, vol. 40, no. 13, pp. 3153-3156, Jul. 2015.

[5] **W. Liu**, J. Zhang, M. Rioux, J. Viens, Y. Messaddeq, and J. P. Yao, "Frequency tunable continuous THz wave generation in a periodically poled fiber," *IEEE Trans. THz Sci. Technol.*, vol. 5, no. 3, pp. 470-477, May 2015.

[6] M. Li, **W. Liu**, N. Huang, R. S. Guzzon, N. Zhu, J. Azaña, L. A. Coldren and J. P. Yao, "Advances in all-optical circuits," *Opt. Photonics News*, vol. 26, no. 3, pp. 18-19, Mar. 2015.

[7] W. Zhang, **W. Liu**, H. Shahoei, and J. P. Yao, "Independently tunable multichannel fractional-order temporal differentiator based on a silicon-photonic symmetric Mach–Zehnder interferometer incorporating cascaded microring resonators," *J. Lightw. Technol.*, vol. 33, no. 2, pp. 361-367, Jan. 2015.

[8] **W. Liu**, J. P. Yao, "Photonic generation of microwave waveforms based on a polarization modulator in a Sagnac loop," *J. Lightw. Technol.*, vol. 32, no. 20, pp. 3637-3644, Oct. 2014.

[9] J. Zhang, **W. Liu**, F. Kong, and J. P. Yao, "Microwave photonic Hilbert transformer based on a single passband microwave photonic filter for simultaneous channel selection and signal processing," *J. Lightw. Technol.*, vol. 32, no. 17, pp. 2996-3001, Sep. 2014.

[10] **W. Liu**, J. P. Yao, "Ultra-wideband microwave photonic phase shifter with a 360o tunable phase shift based on an erbium-ytterbium co-doped linearly chirped FBG," *Opt. Lett.*, vol. 39, no. 4, pp. 922-924, Feb. 2014.

[11] L. Gao, **W. Liu**, J. P. Yao, "Photonic-assisted microwave frequency multiplication with a tunable multiplication factor," *Opt. Lett.*, vol. 38, no. 21, pp. 4487-4490, Oct. 2013.

[12] **W. Liu**, T. Shao, and J. P. Yao, "UWB and 60-GHz generation and transmission over a WDM-PON," *J. Opt. Commun. Netw.*, vol. 5, no. 9, pp. 1076-1082, Sep. 2013.

[13] **W. Liu**, W. Li, and J. P. Yao, "An ultra-wideband microwave photonic phase shifter with a full 360o phase tunable range," *IEEE Photon. Technol. Lett.*, vol. 25, no. 12, pp. 1107-1110, Jun. 2013.

[14] **W. Liu**, M. Wang, and J. P. Yao, "Tunable microwave and sub-terahertz generation based on frequency quadrupling using a single polarization modulator," *J. Lightw. Technol.*, vol. 31, no. 10, pp. 1636-1644, May 2013.

[15] **W. Liu**, M. Li, C. Wang, and J. P. Yao, "Real-time interrogation of a linearly chirped fiber Bragg grating sensor based on chirped pulse compression with improved resolution and signal-to-noise ratio," *J. Lightwave Technol.*, vol. 29, no. 9, pp. 1239-1247, May 2011.

[16] **W. Liu**, W. Li, J. P. Yao, "Real-time interrogation of a linearly chirped fiber Bragg grating sensor for simultaneous measurement of strain and temperature," *IEEE Photon. Technol. Lett.*, vol. 23, no. 18, pp. 1340-1342, Sep. 2011.

Conference Papers:

[17] **W. Liu**, W. Zhang, and J. P. Yao, "A bandstop microwave photonic delay-line filter with both tunable stop-band rejection ratio and tunable frequency," IEEE MTTS International Microwave Symposium (IMS) 2015, TU3G-1, 17-22 May 2015, Phoenix, Arizona, USA.

[18] **W. Liu**, M. Li, R. S. Guzzon, E. J. Norberg, J. S. Parker, L. A. Coldren, and J. P. Yao, "A microwave photonic temporal integrator based on an InP-InGaAsP integrated tunable coupled ring," IEEE International Topical Meeting on Microwave Photonics (MWP) 2013, 28-31 Oct. 2013, Alexandria, Virginia, USA. (One of the two post-deadline papers.)

[19] **W. Liu**, L. Gao, and J. P. Yao, "Photonic generation of triangular waveforms based on a polarization modulator in a Sagnac loop," IEEE International Topical Meeting on Microwave Photonics (MWP) 2013, 28-31 Oct. 2013, Alexandria, Virginia, USA.

[20] **W. Liu**, J. P. Yao, "UWB and 60-GHz RF generation and transmission over WDM-PON based on bidirectional asymmetric polarization modulation and

frequency multiplication," Photonics North 2013, 3-5 Jun. 2013, Ottawa, Ontario, Canada.

[21] **W. Liu**, J. P. Yao, "Real-time interrogation of a linearly chirped fiber Bragg grating sensor based on chirped pulse compression using a Sagnac loop interferometer," Photonics North 2011, 16-18 May 2011, Ottawa, Ontario, Canada.

[22] M. Li, **W. Liu**, and J. P. Yao, "Continuously tunable chirped microwave pulse generation using an optically pumped linearly chirped fiber Bragg grating," IEEE MTTS International Microwave Symposium (IMS) 2011, WEPL-1, 5-10 Jun. 2011, Baltimore, Maryland, USA.

Statement of Original Contributions

In this section, my original contributions are summarized.

- Chapter 2: I presented a background review about ultrafast photonic signal processing. Three fundamental building blocks in photonic signal processing, including temporal integration, temporal differentiation, and Hilbert transformation, are theoretically analyzed. Methods of implementing those functions are introduced. All text and figures were generated by me. A discussion about two material systems, InP and Silicon-on-Insulator, for implementing photonic signal processors was also addressed.

- Chapter 3: In this chapter, I performed a detailed theoretical study of implementing a photonic integrator, differentiator, and Hilbert transformer. I proposed to use cascaded ring resonators coupled by a bus waveguide as a processing unit to implement a photonic integrator, a differentiator, and a Hilbert transformer. I also developed a study of the structure based on its signal flow graphs, which gave a theoretical approximation to its ideal transfer function of the targeted processing operation including temporal integration, differentiation, and Hilbert transformation.

- Chapter 4: In this chapter, I proposed and experimentally demonstrated a photonic temporal integrator and a Hilbert transformer based on a photonic integrated circuit in an III-V material system. The device consists of a ring resonator with active components, such as SOAs and PMs, to achieve improved performance and a tunable operating wavelength in a temporal photonic integrator and Hilbert transformer. The device was fabricated in the UCSB Nano Fab. The experiment was designed and implemented by me. The text and figures were also generated by me. This work was implemented to explore the capabilities of chip-scale photonic signal processing based on an InP material system.

- Chapter 5: In this chapter, I proposed and experimentally demonstrated a fully reconfigurable photonic integrated signal processor based on a photonic integrated circuit. I conceived the idea of using cascaded ring resonators coupled by a bus waveguide as a processing unit to implement a reconfigurable photonic signal processor to achieve temporal photonic integration, differentiation, and Hilbert transform. The device was fabricated in the UCSB Nano Fab. The experiment was designed and implemented by me. Prior the experiment, a setup dedicated for PIC test with a DC probing and controlling system was developed by me. The text

and figures were also generated by me. Record high performance was achieved by using the proposed processor. In particular, a photonic temporal integrator over a bandwidth of 0.22 nm with an integration time of 10.9 ns was achieved, which was the longest integration time ever reported. Application examples were also developed and demonstrated using either the device or simulation by me. This work represents an important step towards the realization of a fully programmable high speed and wideband general-purpose photonic signal processors that can overcome the inherent speed limitation of electronic signal processors.

- Chapter 6: In this chapter, I proposed and experimentally demonstrated two photonic integrated tunable fractional order temporal differentiators in a CMOS compatible SOI platform. I designed and simulated a passive and an active photonic temporal differentiator and simulated prior to fabrication in the IME. An experiment based on the fabricated devices was designed and implemented by me. The text and figures were also generated by me. The active photonic temporal differentiator was also evaluated for high speed coding. In the experiment, a coded signal with a data rate of 16 Gbps was generated. The coding system can find important applications in secure communications.

Chapter 1

Introduction

1.1 Background

Signal processing is a key function in modern electronic systems [1]. Paralleled in time with the rapid development of electronics, signal processors initially implemented based on bulky discrete devices have evolved to chip-scale integrated digital signal processing (DSP) systems [2]. As a critical technology in digital processing of real-world (analog) signals, DSP is contributing to an ever-increasing range of applications, such as aviation [3], defense [4], communications [5], finance [6], biomedical, and engineering [7].

However, DSP has limitations in processing signals with a large bandwidth. One of the fundamental challenges of DSP is the limited speed, largely restricted by the electronic sampling rate [8]. In a real time signal processing system implemented based on DSP, such as a digital oscilloscope, the speed of the system is limited by the speed of the electronic analog-to-digital conversion (ADC). The world's fastest ADC is 1 GSp/s at present announced by the Texas Instruments Ltd [9], which corresponds to an analog bandwidth of 500 MHz. As a result, to apply DSP for large bandwidth signal processing, multiple ADCs have to be used in parallel with

each ADC sampling a small bandwidth of signal sliced by a bandwidth filter, which increases the system complexity and cost. A brief comparison between the electronic and photonic signal processing can be find in Table I-I.

Table I-I. A Comparison between electronic and photonic signal processing

Electronic Signal Processing	Photonic Signal Processing
Limited processing bandwidth (< a few GHz).	Ultra-large processing bandwidth intrinsic to optics. (> 1 THz)
Need OE/EO conversions in an optical network.	Signals are processed directly in optics without OE/EO conversions
EMI	Immunity of EMI
Interleave multiple ADCs to increase processing bandwidth but with increased system complexity and cost.	Low cost for massive production using CMOS

A solution to overcome the inherent electronic speed limitations is to use photonic signal processing [10] [11]. A photonic signal processing system performs signal processing operations directly in the optical domain, which provides a cost effective, high-speed and high power-efficient signal processing alternative [12] [13] [14]. To date, numerous photonic signal processors have been reported based on either discrete components or photonic integrated circuits [12] [13] [14] [15] [16] [17] [18] [19] [20] [21]. A photonic signal processor based on discrete

components usually has decent programming abilities but it is usually more bulky and less power efficient, while a photonic integrated signal processor has a much smaller footprint and higher power efficiency [22] [23]. A photonic signal processor can be used to implement fundamental signal generation and processing functions such as optical pulse shaping and arbitrary waveform generation [12], optical dispersion compensation [18], temporal integration [19], temporal differentiation [20], and Hilbert transformation [21]. These functions are basic building blocks of a general-purpose signal processor for signal generation and fast computing [24] [25]. Among these essential functions, fast computing operations such as temporal integration, temporal differentiation, and Hilbert transformation have been extensively investigated [21] [26] [27] [28] [29] [30] [31] [32] [33] [34] [35] [36] [37] [38] [39] [40] [41], which can find numerous applications.

1.1.1 Temporal Photonic Integration

A photonic integrator is a device that is able to perform time integral of an optical signal, which can find applications such as in dark soliton generation [27], optical memory [28], and optical analog-to-digital conversion [29]. A photonic temporal integrator, as a fundamental building unit for all-optical signal processing, overcomes the speed limitation of its electronic counterparts. One of the most important characteristic parameters of a photonic integrator is the integration time

[42]. A long integration time means a better integration capability. An ideal photonic temporal integrator should have an infinite integration time.

Recently, the implementation of a temporal integrator based on photonic techniques has been widely investigated, such as the implementation using a fiber Bragg grating (FBG) [19, 30-33] or a microring resonator [34, 35]. In [30], Asghari *et al.* introduced a single uniform FBG incorporating phase shifts along its axial profile to realize an all-optical arbitrary-order temporal integrator. By simply propagating an input optical waveform through the FBG, the cumulative time integral of the complex field envelope of the input waveform can be obtained. The proposed integrator was investigated numerically and optimized by maximizing its power efficiency [31], and a second-order complex-field temporal integrator was experimentally demonstrated with a single apodized uniform-period FBG [32, 33]. To compensate for the insertion loss in the FBG, Slavík *et al.* proposed an all-optical gain-assisted temporal integrator based on a superimposed FBG made in an Er-Yb co-doped optical fiber [19]. A photonic temporal integrator was experimentally demonstrated using the active resonant cavity in the superimposed FBG operating at the exact lasing threshold condition. In these approaches, although the main component is an FBG, the implementation of the system needs multiple discrete components, which makes the system bulky. In addition, the system cannot be reconfigured once the FBG is fabricated. To solve the problems, Ferrera *et al.*

proposed an on-chip complementary metal-oxide-semiconductor (CMOS) technology compatible all-optical integrator based on an add-drop ring resonator [34]. The key component in the integrator is a passive micro-ring resonator. The 1st-order temporal integration of a complex-field optical waveform, with a time resolution of ~8 ps over an integration time exceeding 800 ps, was achieved. However, the throughput of the device was reduced by its very narrow resonance linewidth. The trade-off between the integration bandwidth and overall power efficiency by performing all-optical integration in a micro ring resonator was explored [35]. An input to output power efficiency of 1.5% and an integration time window of ~12.5 ps was achieved. For many applications, however, an integration time as long as a few nanoseconds is needed. To achieve such a long integration time, the insertion loss must be precisely compensated to obtain a high *Q*-factor, which is very challenging especially for a stable operation without causing lasing. Another figure of merit for an integrator is the TBWP. The TBWP is a value representing the throughput limit of a system. For a given system with a known TBWP, there is a tradeoff between the frequency bandwidth and time bandwidth. A larger TBWP is always desire for high bandwidth applications. In addition, an integrator with a fractional or higher order is also needed, which is more difficult to implement [35].

1.1.2 Temporal Photonic Differentiation

A photonic temporal differentiator [36] is a device that performs temporal differentiation of an optical signal, which can find important applications such as all-optical Fourier transform [37, 38], temporal pulse characterization [39], and the demultiplexing of an optical time division multiplexed (OTDM) signal [43]. In addition to a first order differentiator, an *n*-th order photonic differentiator can provide the *n*-th order time derivative of the complex envelope of an input optical signal, and *n* could be a positive integer or fraction. To date, numerous techniques have been proposed to perform an all-optical temporal differentiator, which can be classified into two categories. The first is to design the spectral response of a FBG corresponding to a target differentiator, and the second is to implement differentiators based on optical interferometers such as a Michelson or Mach-Zehnder interferometer (MZI).

In the first category, a photonic temporal differentiator is implemented by a FBG based on a spectral-domain design approach. The transmission spectral response of the FBG is closely matched to the frequency response of a target differentiator by designing the grating period, apodization, or introducing a π phase shift exactly at the signal's central frequency. For example, a uniform long-period fiber grating (LPFG) working in the linear regime inherently behaves as an ultrafast optical temporal differentiator [44], and the output temporal waveform in the core mode of

a LPFG is proportional to the first derivative of the input optical temporal signal. Slavík *et al.* also demonstrated the direct differentiation of a temporal waveform in the sub-picosecond regime using an LPFG [45]. By using apodization techniques in the fabrication of a linearly chirped FBG (LCFBG), an arbitrary order temporal differentiator can also be implemented with a bandwidth of a few hundreds of GHz [46], the operating wavelength and bandwidth can also be tuned by packaging the LCFBG in a digital thermal print head [47]. In addition to using the transmission spectral response of a FBG, a temporal photonic differentiator can also be implemented by an asymmetrical π phase-shifted FBG operated in reflection [48]. The main advantage of the realized device is the relatively short grating length, which could be easily transferred to integrated optics platforms, such as a sidewall phase-shifted Bragg grating in a silicon chip [49].

In the second category, a photonic temporal differentiator is implemented by a conventional two-arm interferometer based on the spectral domain design approach. A conventional interferometer, such as a Michelson interferometer or an MZI, can provide the spectral characteristics that are required for first-order time differentiation over a certain limited bandwidth around each of the destructive-interference wavelengths [41]. In this implementation, both the operation wavelength and bandwidth of the differentiator can be independently tuned by properly adjusting the relative time delay between the interferometer arms. In

addition, a tunable fractional order differentiator can be achieved by tuning the coupling coefficient at the input or output of the interferometer. The implementation can also be transferred into a silicon platform for compact size, potential low cost, and robustness [50], however, the lack of high speed tunability in this design limited the applications of a photonic temporal differentiator.

1.1.3 Temporal Hilbert Transform

A photonic Hilbert transformer is a device that derives the analytic representation of a signal [21], and has been widely used for single-sideband (SSB) modulation. Optical SSB modulation is particularly useful in a radio-over-fiber (RoF) link to avoid dispersion-induced power fading [40]. A Hilbert transformer includes a classical Hilbert transformer (with an order of 1) and a fractional Hilbert transformer (FHT) (with a fractional order). The Hilbert transformer is usually implemented in the electrical domain using digital electronics, but with limited bandwidth and operation frequency. Due to the advantages of high speed and broad bandwidth offered by optics, the implementation of a microwave FHT using photonic techniques has been widely investigated recently [51-60]. These approaches can be classified into three categories. In the first category, an FHT was achieved based on a phase shifted FBG [51-53]. In [51] , Asghari *et al.* proposed a uniform FBG with a single π phase shift in the middle of the grating to perform the HT. To obtain an FHT, Li *et al.* proposed to use the discrete layer peeling (DLP)

method by which the FBG was directly designed based on the target response in the frequency domain corresponding to an FHT transmission function with a phase jump less or greater than π [52, 53]. The major limitation of the FBG-based FHT is that the fractional order is not tunable. Once the FBG is fabricated, the order of the FHT is fixed. In the second category, an FHT was achieved in a photonic temporal pulse shaping (TPS) system. In [54], an FHT with tunable fractional order based on TPS was proposed and experimentally demonstrated. The fractional order of the proposed FHT was realized by applying a step function to a phase modulator to introduce a phase jump. Although a tunable fractional order was achieved, the system is complicated and costly due to the requirement of a high speed pattern generator to provide a fast step function. In the third category, an FHT was achieved by using a photonic microwave delay-line filter. A continuously tunable FHT can be implemented based on a multitap uniformly spaced or a nonuniformly spaced photonic microwave delay-line filter [55, 56]. The multitap uniformly spaced filter should have negative coefficients which was realized based on polarization-modulation and polarization-modulation to intensity-modulation conversion in an optical polarizer [55]. The tunability of the fractional order was achieved by tuning the coefficient of the zero-th tap. Compared with the multitap uniformly spaced filter, a nonuniformly spaced delay-line filter is easier to implement and less costly since the negative coefficients can be equivalently realized through nonuniform

sampling [56]. However, FHTs implemented in the three categories did not provide a tunable fractional order or the capability to integrate into a chip-scale device.

Although the photonic implementations of these functions have been reported based on photonic integrated circuits [19-21, 34, 36], a signal processor is usually designed to perform a specific function with limited application performance, such as a small integration time for temporal integration, and the limited tunability for a temporal differentiator and Hilbert transformer, which is an important step of photonic signal processors towards real applications. For general-purpose signal processing, however, a photonic signal processor should be able to perform multiple functions with high application performance.

1.2 Major contributions

Reconfigurable photonic signal processors capable of performing temporal integration, differentiation, and Hilbert transformation have been designed and experimentally demonstrated both in the III-V and SOI material system.

First, an add-drop ring resonator consisting of semiconductor optical amplifiers and current injection PMs is designed and fabricated in the InP-InGaAsP material system, which is also experimentally demonstrated with functions of photonic temporal integration and tunable fractional Hilbert transformation. The proposed add-drop ring resonator processing unit employs a single ring structure coupled

with two bypass waveguides. The tunable coupling between the ring and the waveguides is realized by a multi-mode interference (MMI) MZI coupler. Within the ring, two SOAs are incorporated to compensate for the insertion loss. In addition, there is a current injection PM in the ring for wavelength tuning. The device can be configured to perform photonic temporal integration with an integration time window and a tunable operation wavelength in a single PIC. The integration time window as wide as 6331 ps is achieved, which is an order of magnitude longer than that provided by the previously reported photonic integrators. The device can also be configured to perform fractional Hilbert transformation with a tunable operation wavelength. The device for Hilbert transformation is experimentally demonstrated with a working bandwidth of 27.2 GHz and a continuously tunable fractional order from 0 to 1.

Second, a fully reconfigurable photonic signal processor is designed, fabricated and experimental demonstrated to perform the mentioned photonic temporal integration, differentiation, and Hilbert transformation. The photonic signal processor consists of three active microring resonators and a bypass waveguide as a processing unit cell. To obtain on-chip reconfigurability, nine SOAs and twelve current-injection PMs are incorporated in the unit cell. The tunable coupling in the unit cell is realized using four tunable couplers (TCs) with each consisting of two MMI couplers and two PMs. The coupling ratio in each TC can be tuned by adjusting the injection currents to the two PMs in the TC. Within each ring, there

are two SOAs used to compensate for the insertion loss. When an SOA is forward biased, it can create an optical gain. On the other hand, an SOA can operate as an optical absorber when it is reverse biased, which is the key to achieve the configurability of the processor. Consequently, with the SOAs utilized in this design, a waveguide path could effectively be on or off to facilitate the synthesis of various circuit geometries. The signal processing functions including temporal integration, temporal differentiation, and Hilbert transformation can be implemented by configuring the unit cell with a specific geometry. In addition, there is a current-injection PM in each ring resonator, and a PM in the bypass waveguide, which are used to achieve wavelength tunability. Furthermore, the order of the signal processor, either a fractional or higher order, can be tuned by tuning the coupling ratio of the TC. The actually fabricated device is well prepared and wire-bonded to a carrier to enable an easy access to the SOAs and PMs for test and experiments.

Third, a passive and an active photonic temporal differentiator based on SOI platform are also designed and experimentally demonstrated. The passive photonic temporal differentiator employs an MMI coupler as one of the two 3 dB couplers of the MZI. By changing the input polarization state, the coupling coefficient in the MZI is changed. Correspondingly, the phase shift in the destructive interference wavelength is changed which leads to a tunable fractional order of the photonic temporal differentiator. The active photonic temporal differentiator uses two

cascaded MZIs, a balanced MZI and an unbalanced MZI. A PM is incorporated in one of the two arms of each MZI, as a result, the balanced MZI with a PM in one of its two arm forms a tunable coupler, which can be used to tune the fractional order of the active differentiator. The PM in the unbalanced MZI can be used to tune the operating wavelength. The two photonic differentiators are designed and fabricated in a CMOS compatible SOI platform. A Gaussian pulse is temporally differentiated by the two differentiators with a tunable fractional order from 0 to 1. A high-speed coding system based on the active differentiator is also proposed and experimentally demonstrated with a data rate of 16 Gbps.

1.3 Organization of this thesis

The thesis consists of seven chapters. In Chapter 1, a brief introduction to photonic temporal signal processing is presented. A review of the recently proposed approaches for photonic temporal integration, differentiation, and Hilbert transformation is also discussed. Then, the major contributions of this research are addressed. In Chapter 2, a review of ultrafast photonic signal processing is given. In Chapter 3, the principle of implementing photonic temporal signal processing functions based on ring resonators and interferometers is presented. A theoretical study of implementing temporal integrators, differentiators, and Hilbert transformers based on a coupled ring resonator structure is developed and the design of optical geometry for a reconfigurable photonic signal processor is

provided. In Chapter 4, a photonic integrator and a photonic Hilbert transformer are experimentally demonstrated based on a single ring resonator fabricated in an InP-InGaAsP material system. A temporal integration time of 6331 ps with a bandwidth of 0.12 nm is obtained, and a tunable fractional Hilbert transformer is achieved based on a single ring resonator. In Chapter 5, a reconfigurable photonic signal processor based on a coupled ring resonator structure is experimentally demonstrated. The reconfigurable photonic signal processor can be configured to perform photonic temporal integration, differentiation, and Hilbert transformation. An integration time of 10.9 ns with a bandwidth of 0.22 nm is achieved in the proposed photonic signal processor, and the integration time is more than one order of magnitude longer than the previously reported results. Application examples, such as image processing, single sideband modulation, and WDM filtering, are demonstrated. In Chapter 6, a passive and an active fractional order photonic temporal differentiator implemented by MZIs based on a CMOS compatible SOI platform are proposed and experimentally demonstrated. A high-speed coding system based on the active differentiator is also proposed and experimentally demonstrated with a data rate of 16 Gbps. Finally, a conclusion is drawn in Chapter 7.

Chapter 2

Review of Ultrafast Photonic Signal Processing

2.1 Photonic Signal Processing (PSP) Functions

Photonic signal processing manipulates an input signal in the optical domain, which offers large processing bandwidth intrinsic to optics. A photonic signal processor can be used to implement fundamental signal generation and processing functions such as temporal integration [19], temporal differentiation [20], and Hilbert transformation [21]. These functions are basic building blocks of a general-purpose signal processor for signal generation and fast computing. With a reconfigurability, a photonic signal can also be used as an optical FPGA for dedicated applications, such as image processing and optical single side-band modulation in an all-optical network.

2.1.1 Integration

A photonic integrator is a device that is able to perform time integral of an optical signal, which can find applications in data processing [61], optical memory [62], and optical computing [63, 64].

Mathematically, a temporal integrator can be implemented using a linear time-invariant filter with a transfer function given by [35]

$$H(\omega) = \frac{1}{j(\omega - \omega_0)} \tag{2-1}$$

where $j = \sqrt{-1}$, ω is the angular optical frequency and ω_0 is the carrier frequency of the signal to be processed. The magnitude and phase response of a photonic temporal integrator are shown in Fig. 2-1. In addition, an *n*-th order integrator can be implemented by cascading n first order integrators. And the transfer function of an *n*-th order temporal integrator can then be written as

$$H_n(\omega) = \left[\frac{1}{j(\omega - \omega_0)} \right]^n \tag{2-2}$$

where *n* is the order of the photonic temporal integrator.

A photonic temporal integrator, as a fundamental building unit for all-optical signal processing, overcomes the speed limitation of its electronic counterparts. One of the most important characteristic parameters of a photonic integrator is the integration time. A long integration time means a better integration capability. An ideal photonic temporal integrator should have an infinite integration time. In Fig. 2-2, the temporal integrations of a Gaussian pulse, an in-phase doublet pulse, an

out-of-phase doublet pulse, and a monocycle pulse have been given. The offset axis refers to the distance from the central time/frequency of interest.

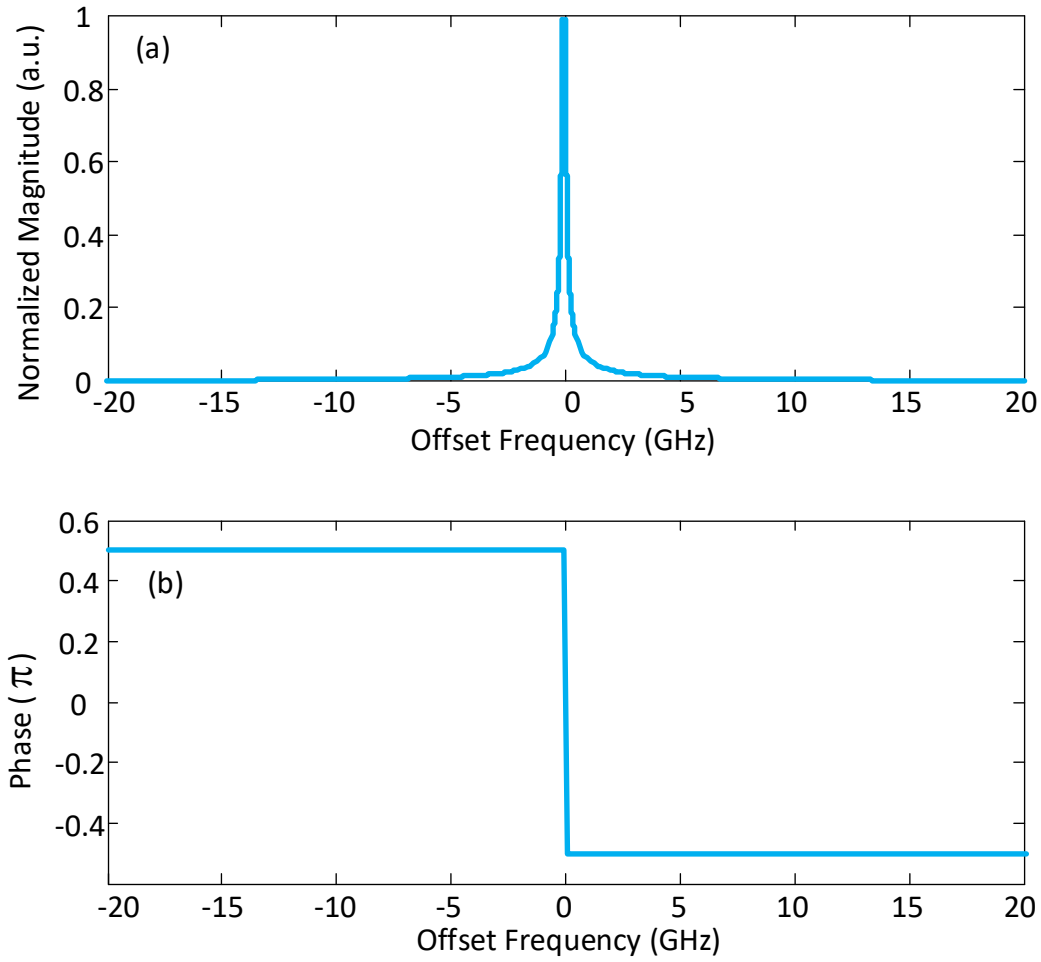

Fig. 2-1. (a) Magnitude and (b) phase of the transfer function of a photonic temporal integrator (2-1).

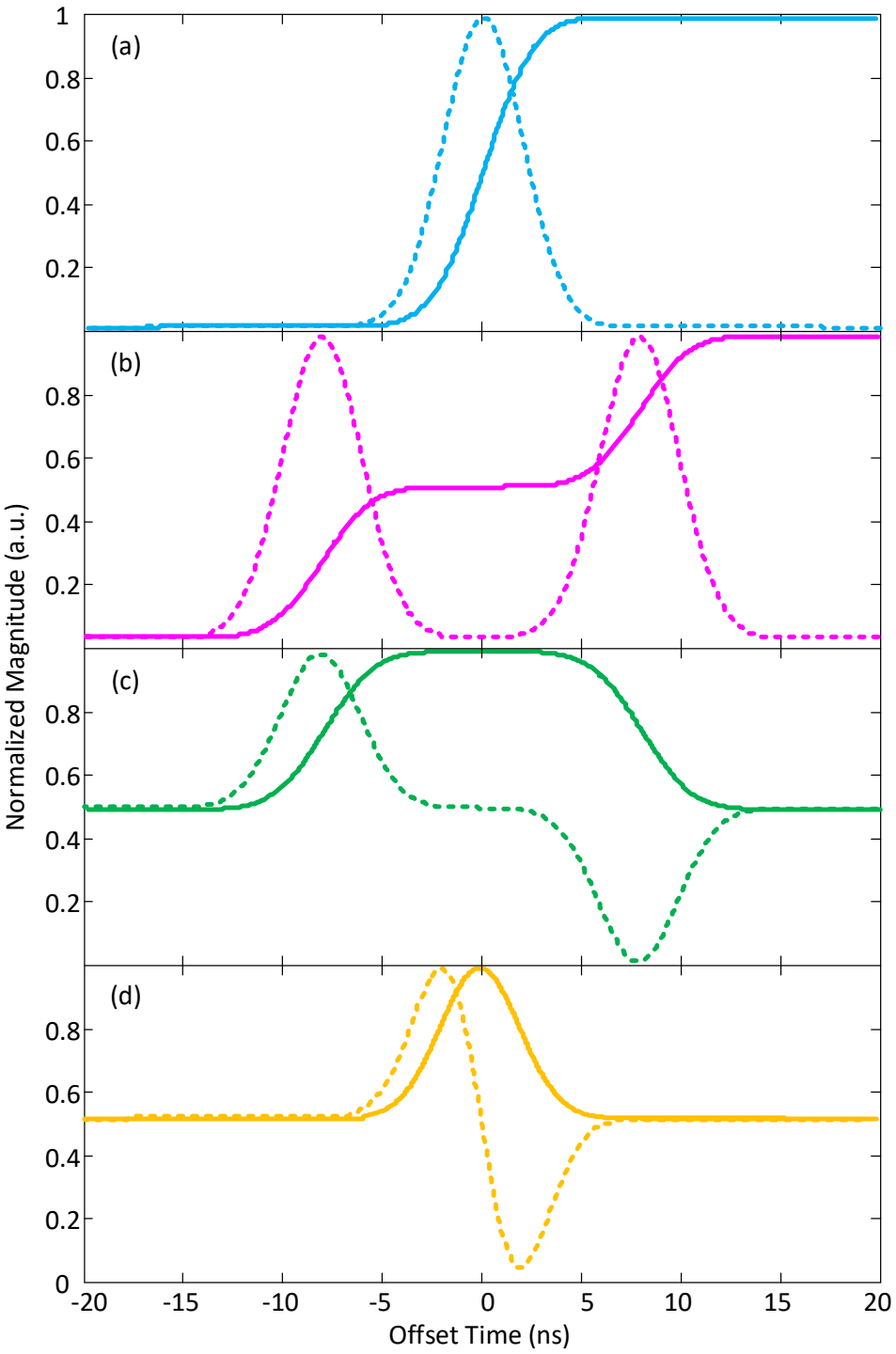

Fig. 2-2. Solid line in each subplot shows the temporal integration of an input signal with a dashed line. (a) a Gaussian pulse, (b) an in-phase doublet pulse, (c) an out-of-phase doublet pulse, (d) a monocycle pulse.

Recently, the implementation of a temporal integrator based on photonic techniques has been widely investigated, among which there are major techniques, one is using an FBG [19, 30-33, 65, 66], and the other is using a resonator [34, 35].

In the first technique, a customized FBG such as an apodized uniform-period FBG [65] or a phase-shifted FBG [30] is designed to have a spectral response with a close match to the transfer function of a photonic integrator as given in (2-1). In [65], Asghari *et al.* introduced a single uniform FBG with customized apodization to realize an all-optical temporal integrator. By using an inverse scattering algorithm, a uniform-period FBG can have a decreased-exponential spectral response in reflection to implement a photonic temporal integrator [65], which is given in Fig. 2-3.

By simply propagating an input optical waveform coupled into the FBG, the cumulative time integral of the complex field envelope of the input waveform can be obtained from the reflection. The proposed integrator was investigated numerically [65]. In addition, a phase shifted FBG, which usually has a π phase shift located in the middle of the grating, can also be used to implement a photonic temporal integrator [30]. In these approaches, although the main component is an FBG, the implementation of the system needs multiple discrete components, which

makes the system bulky. In addition, the system cannot be reconfigured once the FBG is fabricated.

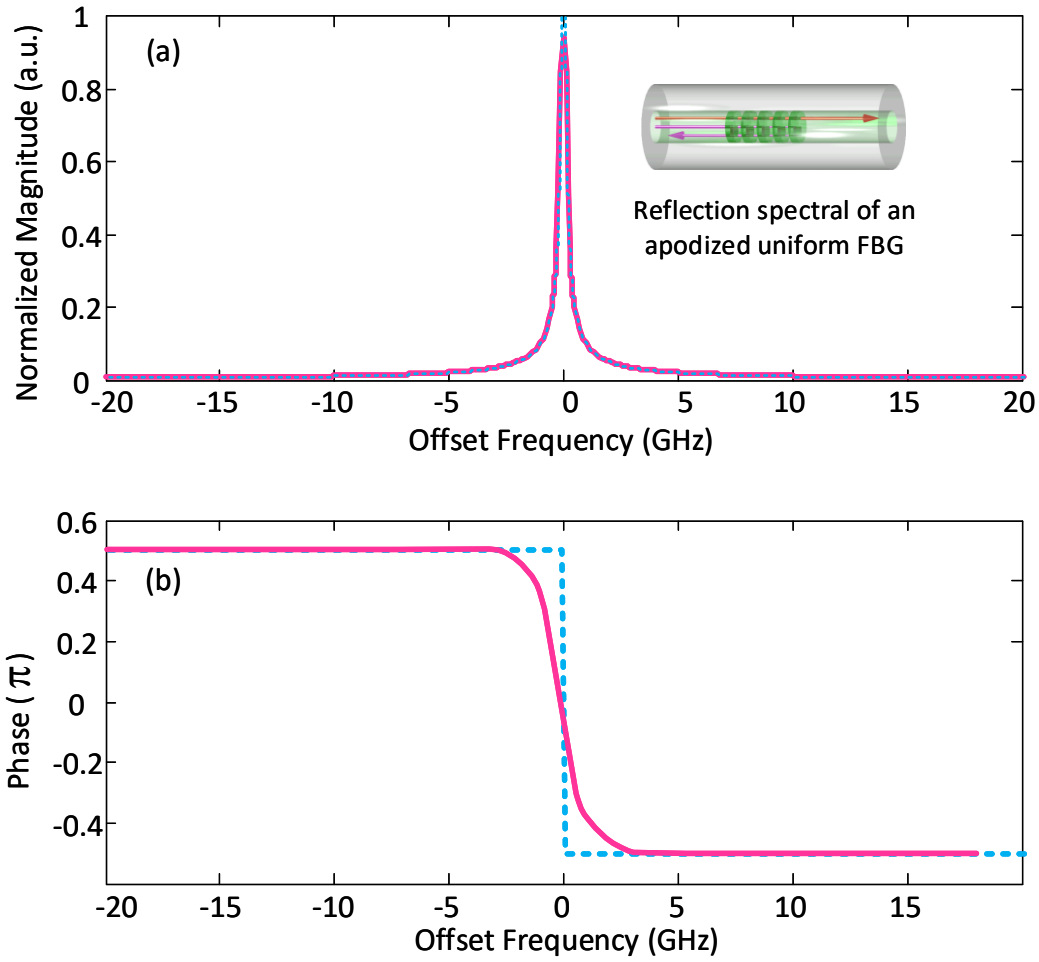

Fig. 2-3. Magnitude and phase of the spectral response corresponding to the customized FBG (solid line) and to an ideal integrator (dashed line).

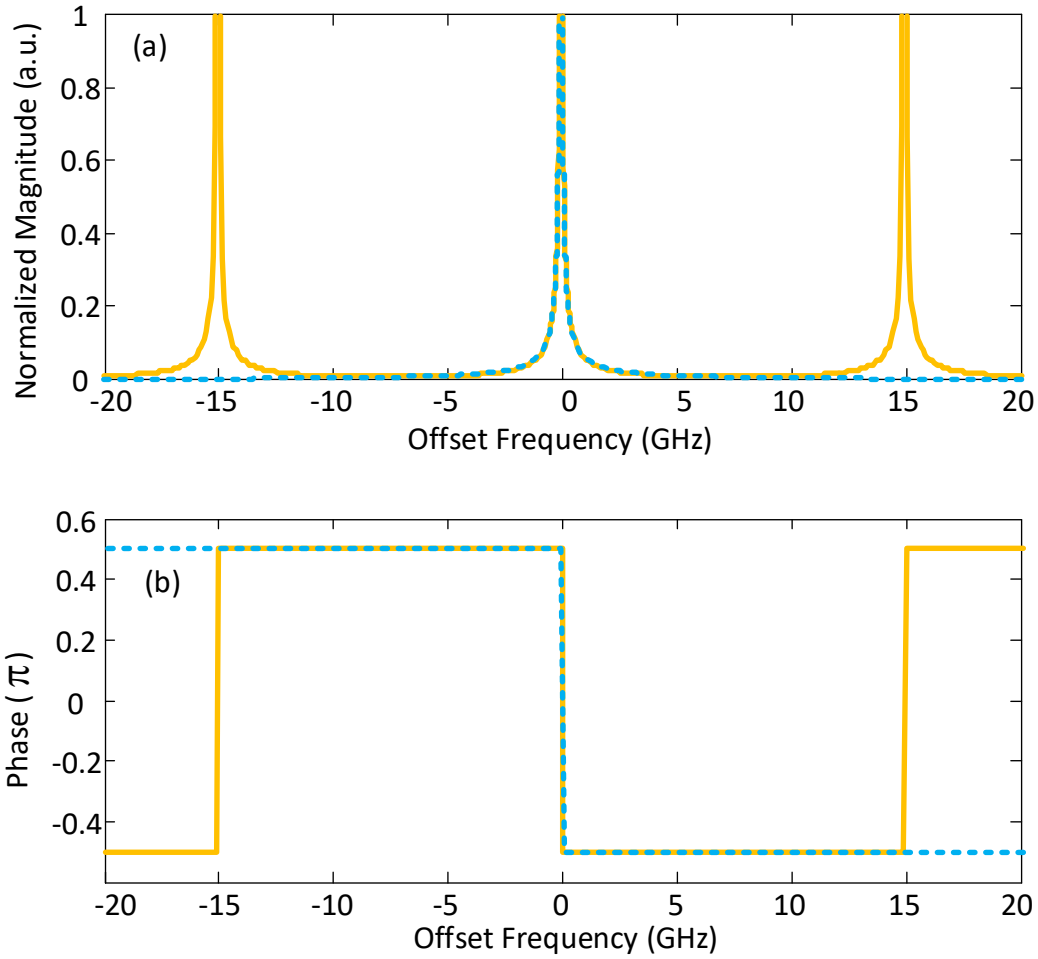

Fig. 2-4. Magnitude and phase of the spectral response corresponding to an add drop ring resonator (solid line) and to an ideal integrator (dashed line).

In the second technique, a resonator such as a Fabry-Pérot (FP) cavity or a microring resonator is used to implement a photonic temporal integrator. The magnitude and phase responses of a ring resonator (FP cavity has similar responses) present close match to a photonic integrator as shown in Fig. 2-4. In [19], Slavík *et*

al. proposed an all-optical gain-assisted temporal integrator based on a FP cavity implemented by a superimposed FBG made in an Er-Yb co-doped optical fiber. The integration function was experimentally demonstrated using the active resonant cavity in the superimposed FBG operating at the exact lasing threshold condition. Ferrera *et al.* also proposed an on-chip CMOS technology compatible all-optical integrator based on an add-drop ring resonator [34]. The key component in the integrator is a passive micro-ring resonator. The 1st-order temporal integration of a complex-field optical waveform, with a time resolution of ~8 ps over an integration time exceeding 800 ps, was achieved. However, the throughput of the device, which is the input-output energy efficiency, was reduced by its very narrow resonance linewidth. Time resolution is determined by the bandwidth (loop length), which is related to the Q factor. Resolution reflects the processing bandwidth, which is very important. Throughput is the input – output energetic efficiency, which is described in Ref. [34]. It is an important metric for an integrator. Higher throughput means higher energy efficiency and less loss, and then higher Q factor which eventually leads to longer integration time. The trade-off between the integration bandwidth and overall power efficiency by performing all-optical integration in a micro ring resonator was explored [35]. An input to output power efficiency of 1.5% and an integration time window of ~12.5 ps was achieved. For many applications, however, an integration time as long as a few nanoseconds is needed. To achieve such a long integration time, the insertion loss must be precisely compensated to

obtain a high *Q*-factor, which is very challenging especially for a stable operation without causing lasing. In principle, a photonic temporal integrator can have 0 loss with the gain from the SOAs, however, a resonator/cavity is very easy to lase when loss is fully compensated. Therefore, a stable operation of integration should always avoid lasing while keeping a minimum insertion loss for higher Q-factor, longer integration time. In addition, an integrator with a fractional or higher order is also needed, which is more difficult to implement [35].

2.1.2 Differentiation

A photonic temporal differentiator [36] is a device that performs temporal differentiation of an optical signal, which can find important applications such as all-optical Fourier transform [37, 38], temporal pulse characterization [39], and the demultiplexing of an OTDM signal [43]. In addition to a first order differentiator, an *n*-th order photonic differentiator can provide the *n*-th order time derivative of the complex envelope of an input optical signal, and *n* could be a positive integer or fraction. A tunable fractional order differentiator can provide better flexibility in signal processing, such as signal coding [41] and tunable image enhancement [67].

An *n*th-order temporal differentiator can be considered as an LTI system with a transfer function given by

$$H_n(\omega) = \left[j(\omega - \omega_0) \right]^n = \begin{cases} e^{jn\frac{\pi}{2}} |\omega - \omega_0|^n & \omega > \omega_0 \\ e^{-jn\frac{\pi}{2}} |\omega - \omega_0|^n & \omega < \omega_0 \end{cases} \quad (2\text{-}3)$$

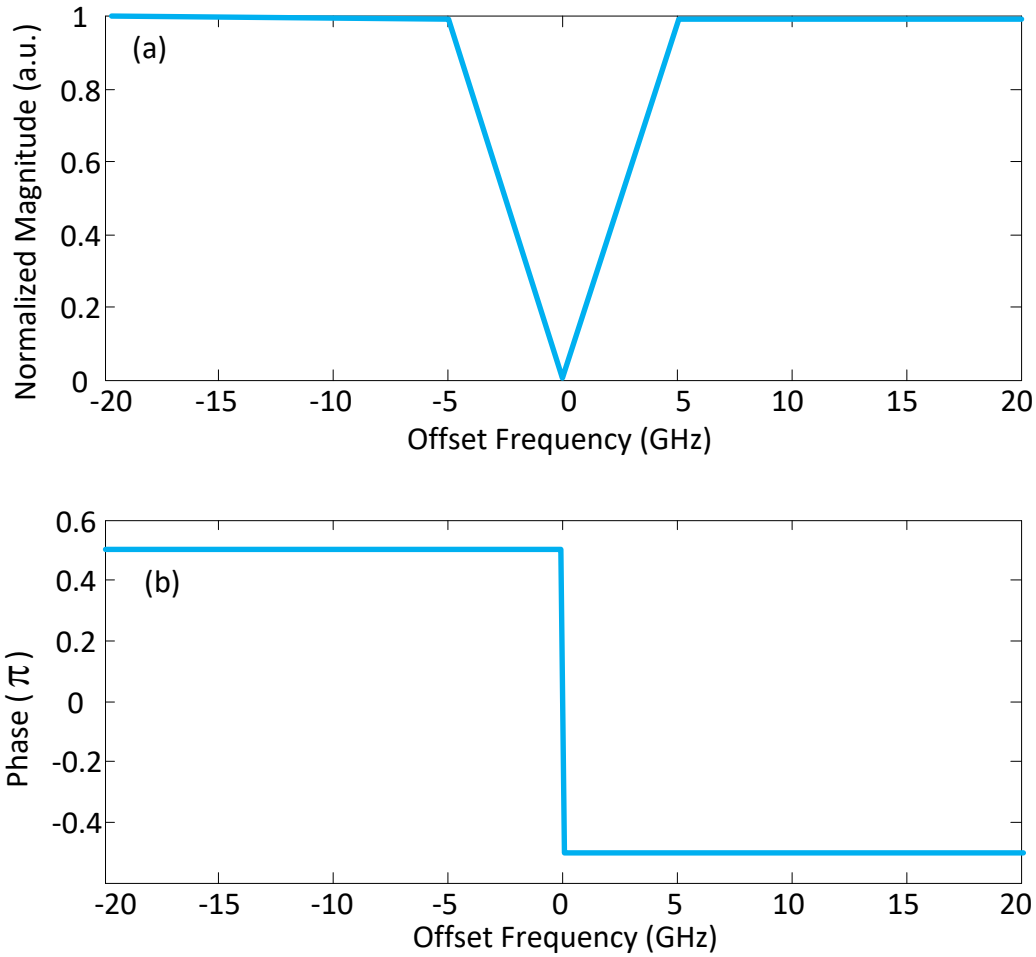

Fig. 2-5. (a) Magnitude and (b) phase of the transfer function of a first-order photonic temporal differentiator (2-3).

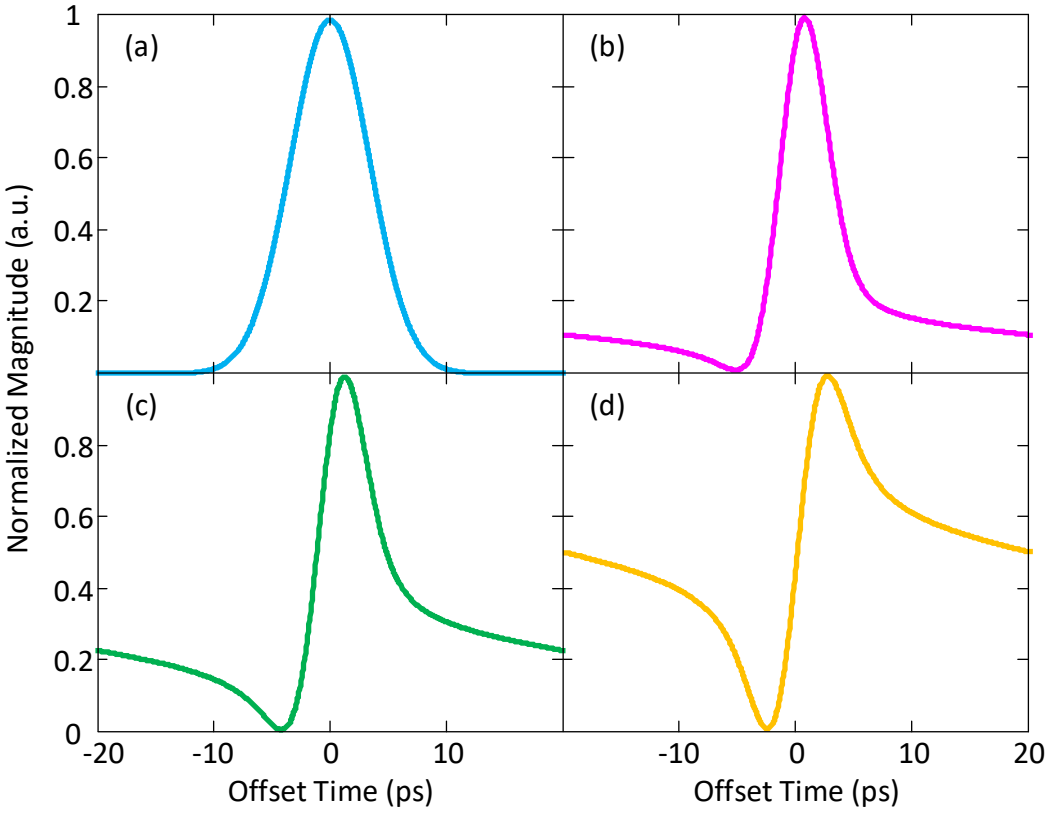

Fig. 2-6. Temporal differentiation of (a) a Gaussian profile pulse with a differentiation order of (b) 0.5, (b) 0.75, and (c) 1.

As can be seen an *n*th-order temporal differentiator has a magnitude response of $|\omega-\omega_0|^n$ and a phase jump of $n\pi$ at ω_0. The magnitude and phase response of a first-order temporal differentiator is shown in Fig. 2-5 In Fig. 2-6, the temporal differentiation of a Gaussian pulse with a fractional order of 0.5, 0.75, and 1 is given. In real applications, an optical filter with a frequency response given by (2-3) can be implemented using an FBG or an optical interferometer [41]. For example,

an MZI can be used to implement an optical temporal differentiator. By controlling the coupling coefficients of the input and output couplers in an MZI, a tunable phase shift from 0 to 2π can be achieved, thus a temporal differentiator with a tunable fractional order can be implemented.

To date, numerous techniques have been proposed to perform an all-optical temporal differentiator, which can be classified into two categories. The first is to design the spectral response of an FBG corresponding to a target differentiator, and the second is to implement differentiators based on optical interferometers such as a Michelson or an MZI.

In the first category, a photonic temporal differentiator is implemented by a FBG based on a spectral-domain design approach. The transmission spectral response of the FBG is closely matched to the frequency response of a target differentiator by designing the grating period, apodization, or introducing a π phase shift exactly at the signal's central frequency. For example, a uniform long-period FBG working in the linear regime inherently behaves as an ultrafast optical temporal differentiator as shown in Fig. 2-7 [44], and the output temporal waveform in the core mode of a LPFG is proportional to the first derivative of the input optical temporal signal. Slavík *et al.* also demonstrated the direct differentiation of a temporal waveform in the sub-picosecond regime using an LPFG [45]. By using apodization techniques in the fabrication of an LCFBG, an arbitrary order temporal differentiator can also

be implemented with a bandwidth of a few hundreds of GHz [46], the operating wavelength and bandwidth can also be tuned by packaging the LCFBG in a digital thermal print head [47]. In addition to using the transmission spectral response of a FBG, a temporal photonic differentiator can also be implemented by an asymmetrical π phase-shifted FBG operated in reflection [48], the main advantage of the realized device is the relatively short grating length, which could be easily transferred to integrated optics platforms, such as a sidewall phase-shifted Bragg grating in a silicon chip [49].

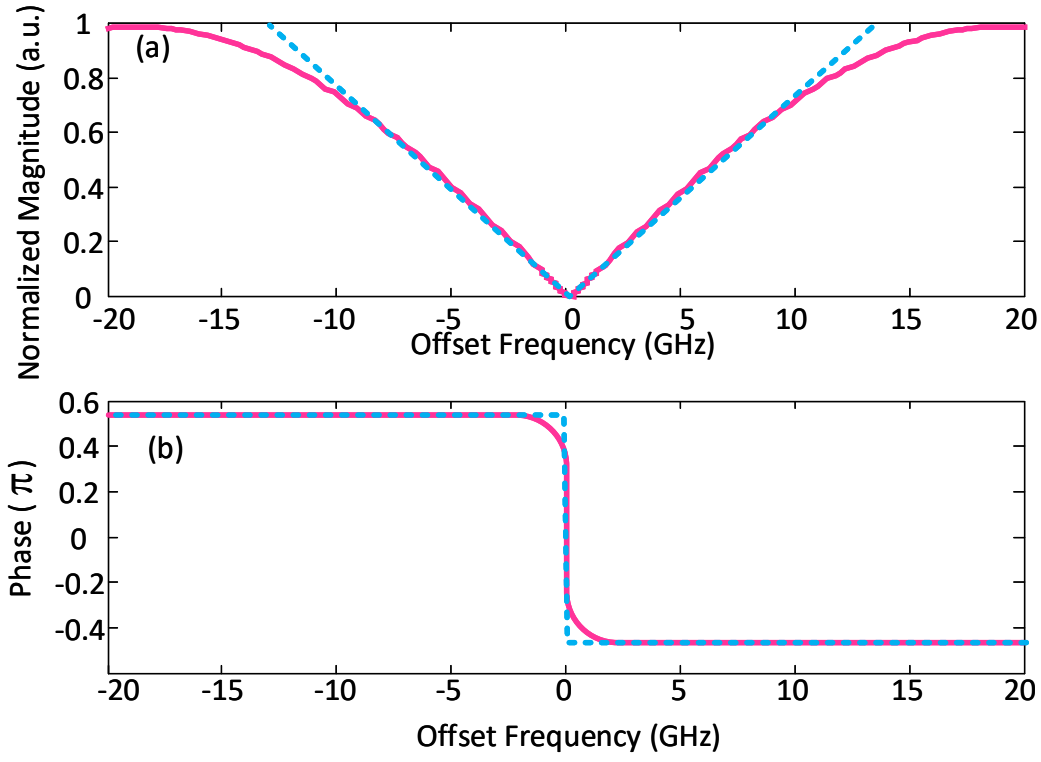

Fig. 2-7. Magnitude and phase of the spectral response corresponding to the customized LPFG (solid line) and to an ideal differentiator (dashed line).

In the second category, a photonic temporal differentiator is implemented by a conventional two-arm interferometer based on the spectral domain design approach. A conventional interferometer, such as a Michelson interferometer or an MZI, can provide the spectral characteristics that are required for first-order time differentiation over a certain limited bandwidth around each of the destructive-interference wavelengths as shown in Fig. 2-8 [41]. In this implementation, both the operation wavelength and bandwidth of the differentiator can be independently tuned by properly adjusting the relative time delay between the interferometer arms. In addition, a tunable fractional order differentiator can be achieved by tuning the coupling coefficient at the input or output of the interferometer. The implementation can also be transferred into a silicon platform for compact size, potential low cost, and robustness [50], however, the lack of high speed tuning in this design limits its applications for high-speed reconfigurable signal processing.

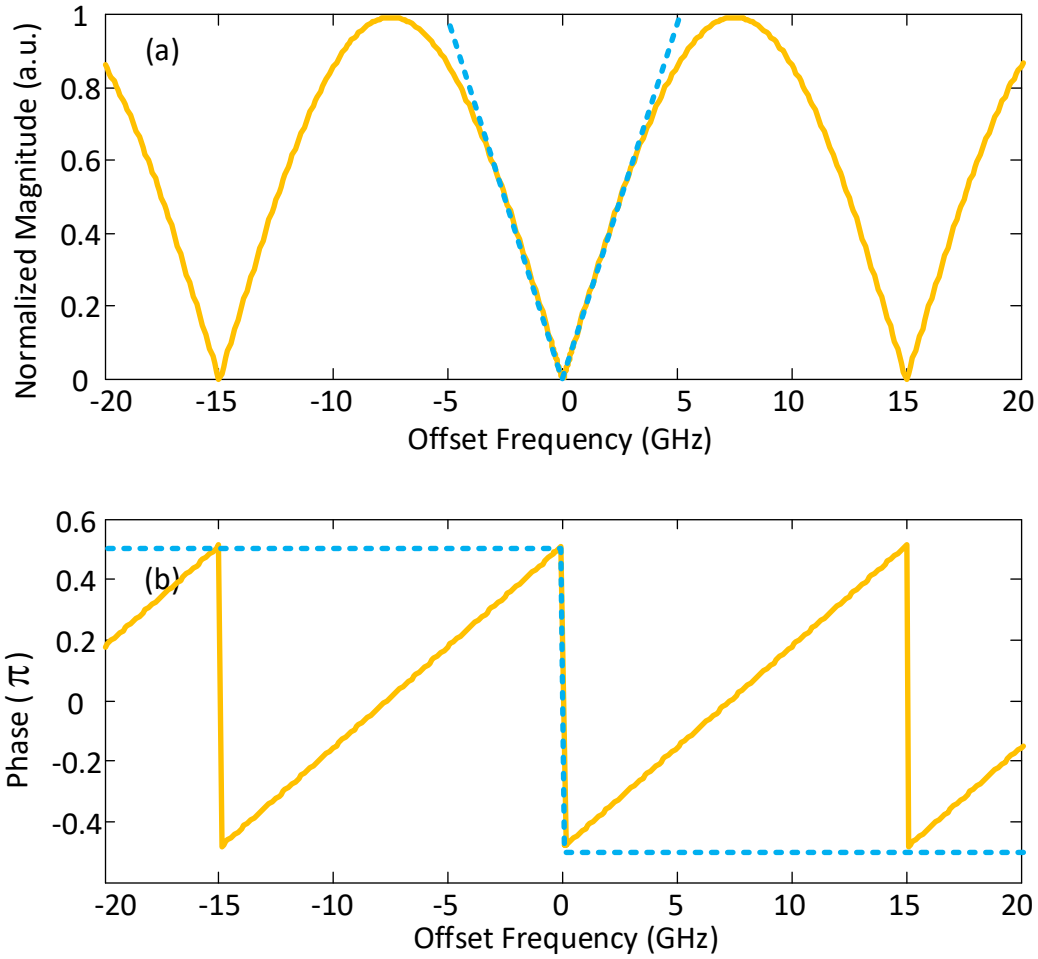

Fig. 2-8. Magnitude and phase of the spectral response corresponding to an MZI (solid line) and to an ideal differentiator (dashed line).

2.1.3 Hilbert Transformation

A photonic Hilbert transformer is a device that performs Hilbert transform of a signal [21], and has been widely used for SSB modulation. Optical SSB modulation is particularly useful in a radio-over-fiber (RoF) link to avoid dispersion-induced power fading [40]. A Hilbert transformer includes a classical Hilbert transformer

(with an order of 1) and an FHT (with a fractional order). The fractional order Hilbert transformer can be used to construct a secure communication system [68], in which the fractional order *n* is used as a secret key for demodulation.

A *n*th order Hilbert transformer is an LTI system with a transfer function given by [68]

$$H_n(\omega)=\begin{cases} e^{-jn\frac{\pi}{2}} & \omega>0 \\ \cos\left(n\frac{\pi}{2}\right) & \omega>0 \\ e^{jn\frac{\pi}{2}} & \omega<0 \end{cases} \tag{2-4}$$

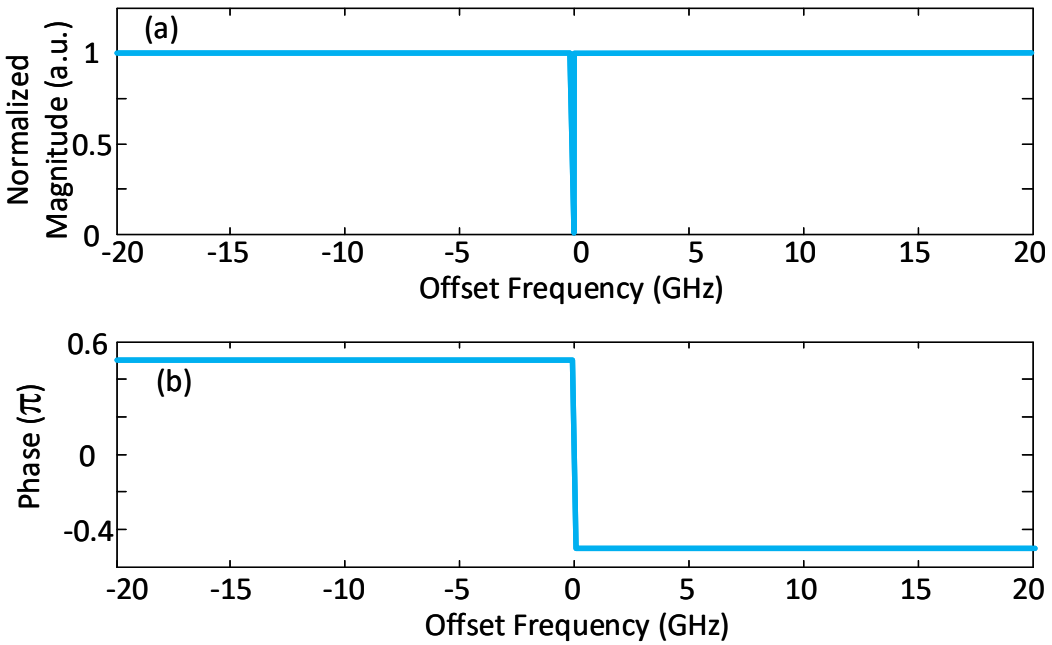

Fig. 2-9. (a) Magnitude and (b) phase of the transfer function of a first-order photonic temporal Hilbert transformer (2-4).

As can be seen an nth-order Hilbert transformer has a magnitude response of 1 and a phase jump of $n\pi$ at ω_0 as shown in Fig. 2-9. A fractional Hilbert transformer becomes a conventional Hilbert transformer when n = 1. For n = 0, we have $H_0(\omega)=1$, which is an all-pass filter. For 0 < n < 1, the output is a weighted sum of the input signal and its conventionally Hilbert transformed signal as shown in Fig. 2-10.

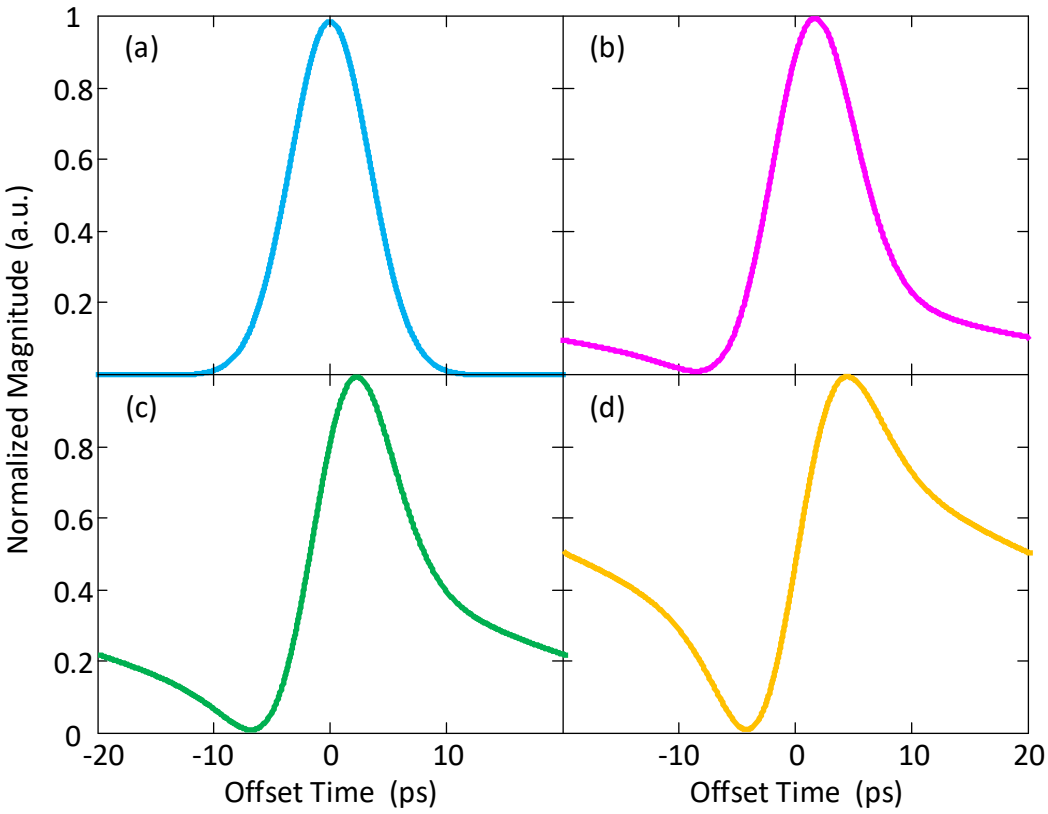

Fig. 2-10. Temporal Hilbert transformation of (a) a Gaussian profile pulse with a fractional order of (b) 0.5, (b) 0.75, and (c) 1.

The Hilbert transformer is usually implemented in the electrical domain using digital electronics, but with limited bandwidth and operation frequency. Due to the advantages of high speed and broad bandwidth offered by optics, the implementation of a microwave FHT using photonic techniques has been widely investigated recently [51-56]. These approaches can be classified into three categories.

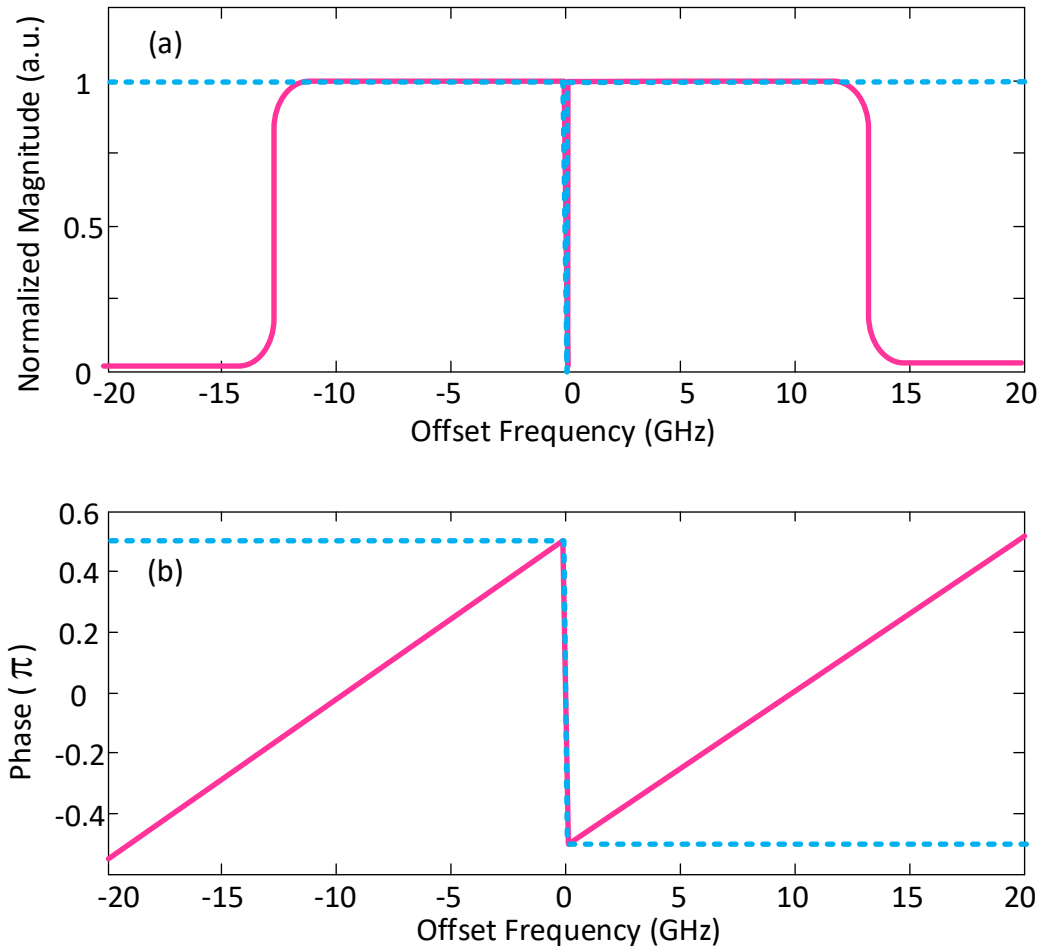

Fig. 2-11. Magnitude and phase of the spectral response corresponding to the customized phase-shifted FBG (solid line) and to an ideal Hilbert transformer (dashed line).

In the first category, an FHT was achieved based on a phase shifted FBG [51-53]. In [51] , Asghari *et al.* proposed a uniform FBG with a single π phase shift in the middle of the grating to perform the HT. To obtain an FHT, Li *et al.* proposed to use the DLP method by which the FBG was directly designed based on the target response in the frequency domain corresponding to an FHT transmission function with a phase jump less or greater than π as shown in Fig. 2-11 [52, 53]. The major limitation of the FBG-based FHT is that the fractional order is not tunable. Once the FBG is fabricated, the order of the FHT is fixed.

In the second category, an FHT was achieved by using a ring resonator as shown in Fig. 2-12. In [21], an FHT with tunable fractional order based on a high-contrast germanium-doped silica-on-silicon microring resonator was proposed and experimentally demonstrated. Based on the polarization dependency of the microring resonator, the fractional order of the proposed FHT was realized by changing the polarization direction of the incident light to the microring resonator using a polarization controller. Although a tunable fractional order was achieved, the tunability depends on the induced polarization dependency which has been considered a drawback in silica planar optical waveguides. In addition, tuning of the polarization using a polarization controller is difficult to integrate in a photonic integrated circuit.

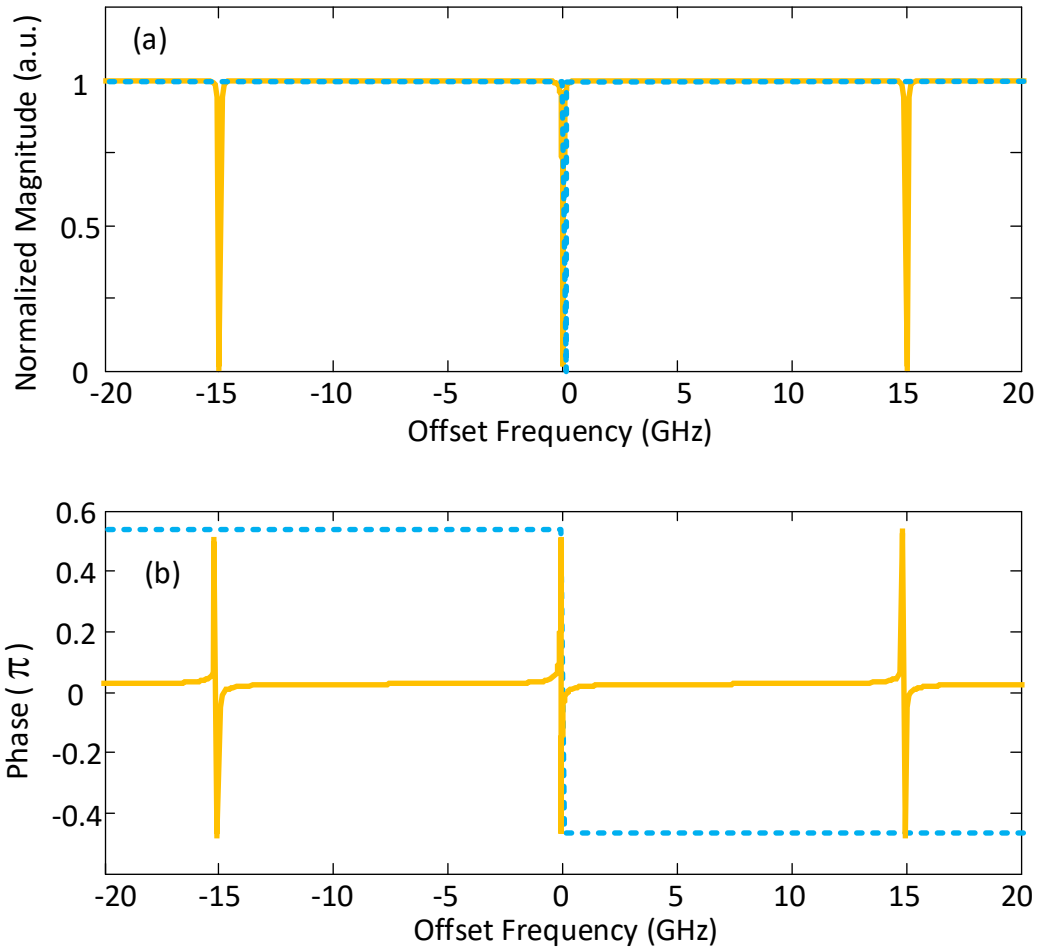

Fig. 2-12. Magnitude and phase of the spectral response corresponding to a ring resonator (solid line) and to an ideal Hilbert transformer (dashed line).

In the third category, an FHT was achieved by using a microwave photonic delay-line filter. A continuously tunable FHT can be implemented based on a multitap uniformly spaced or a nonuniformly spaced photonic microwave delay-line filter [55, 56]. The multitap uniformly spaced filter should have negative coefficients which was realized based on polarization-modulation and polarization-modulation to intensity-modulation conversion in an optical polarizer [55]. The tunability of

the fractional order was achieved by tuning the coefficient of the zero-th tap. Compared with the multitap uniformly spaced filter, a nonuniformly spaced delay-line filter is easier to implement and less costly since the negative coefficients can be equivalently realized through nonuniform sampling [56]. However, FHTs implemented in the three categories are either lacking capability of tunable fractional order or difficult to integrate into a chip-scale device.

2.2 Photonic Integration Platforms

The current photonic signal processing systems based on discrete devices is bulky, costly, and it needs high power consumption for temperature control in each device and insertion loss compensation for multiple device-to-device connections, which reduces the power efficiency. However, photonic integrated circuits (PICs) are devices on which several or even more optical components are integrated. In such an integrated device, only a single temperature controller for a small chip is required, and the insertion loss can be largely reduced due to less device-to-device connections, thus less optical gain is needed to compensate for the loss, which reduces the power consumption. Due to the compact size and low power consumption, PICs can provide very powerful benefits for photonic systems in size, reliability, and ultimately low cost. PICs are already enabling technology for some applications and will be compellingly so in the future. PICs are usually fabricated

with a wafer-scale technology on substrates of InP or silicon. The substrate material, InP or silicon, determines a number of features and limitations of the technology.

2.2.1 III-V Photonic Integration Platform

III-V photonic integrated circuits are built based on an InP wafer, which is comparable for growth of direct band-gap semiconductors from compounds of elements from groups III and V of the periodic table (III-V semiconductors), such as GaAs. In direct-gap materials, an electron is dropping down directly from the conduction band to the valence band, which can be used to make an efficient semiconductor light source or amplifier. The insertion losses in such a material system is low which is suitable for developing large scale complex photonic integrated circuits. Due to scattering and absorption, the waveguide propagation loss in an InP-InGaAsP material system is 2.3 dB/cm.

2.2.2 Silicon-on-Insulator Photonic Integration Platform

Silicon-on-Insulator (SOI) or Silica-on-silicon (SOS) photonic integrated circuits are built on silicon wafers, which provides a strong confinement in waveguides due to the large refractive index contrast between silicon and silica. Therefore, SOI photonic integrated circuits offer a smaller footprint than that of III-V photonic integrated circuits. In addition, the fabrication of SOI photonic integrated circuits

is CMOS comparable, which is an industrial mature technology for massive production chips with low cost. Comparing with III-V photonic integrated circuits, SOI waveguides has lower insertion loss, typically 0.27 dB/cm. However, light sources and amplifiers are not available in SOI due to the indirect band-gap of silicon.

2.3 Summary

Compared with conventional bulky optical processing systems, photonic signal processors based on PICs have a number of distinguishing advantages and significant progress has been made in the last few years. In this chapter, a systematic overview of photonic signal processing and implementation techniques was performed. The key limitations of the current photonic signal processing systems are the bulky size, low power efficiency, and lack of reconfigurability. In many applications, a general purpose photonic signal processor with small footprint and high power efficiency is needed, such as in an all optical network. A solution to achieve compact size, high power efficiency, and reconfigurability is to design a reconfigurable photonic signal processor based on PICs using state-of-the-art photonic integration techniques in III-V and SOI material systems.

Chapter 3

Theoretical Model: Photonic Temporal Signal Processing Using Resonators and Interferometers

3.1 Introduction

A detailed theoretical study of implementing a photonic integrator, differentiator, Hilbert transformer is performed in this chapter. As the photonic integrator and Hilbert transformer can be achieved by ring resonators, and higher order integrator can be implemented by cascading multiple ring resonators, a single ring resonator, two coupled ring resonators, and three coupled ring resonators are studied based on their signal flow graphs. A MZI structure to implement a photonic differentiator is also studied. The transfer function of each optical geometry is given with a theoretical approximation to its ideal transfer function of the targeted processing operation including temporal integration, differentiation, and Hilbert transformation.

3.2 Photonic Integrators

3.2.1. First order integrator

A first order integrator can be implemented using a single add/drop ring resonator in the proposed signal processor, as shown in Fig. 3-1(a). The transfer function is given by [69]

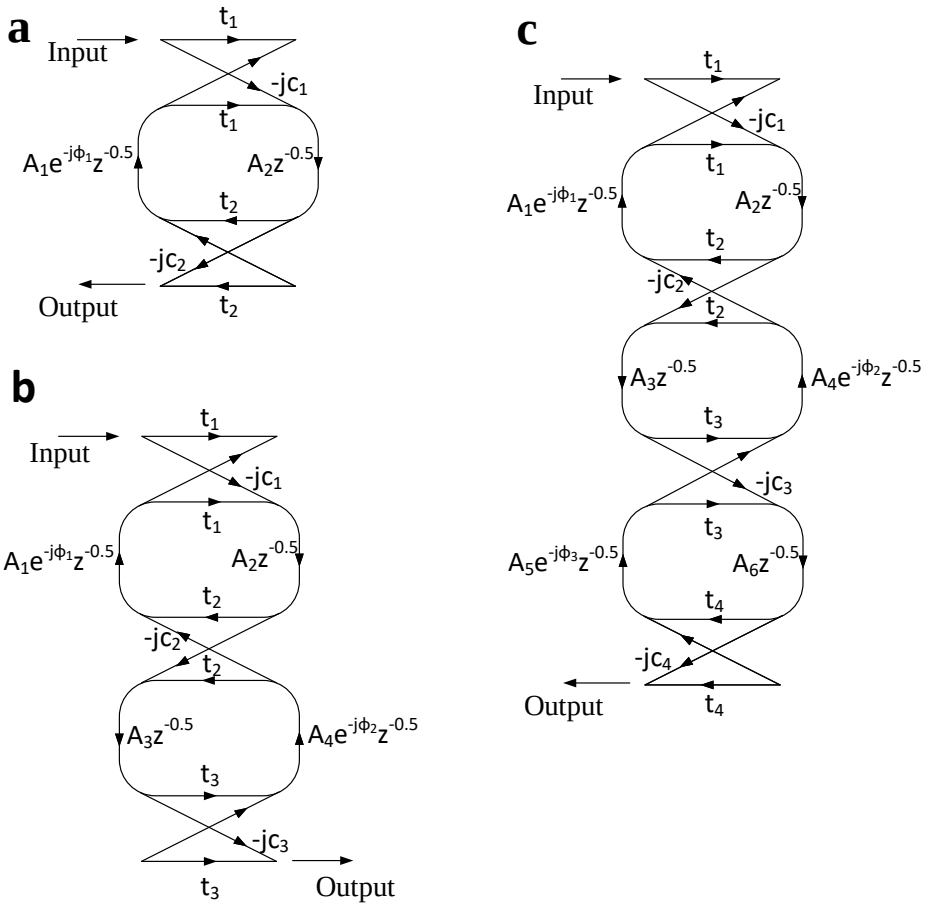

Fig. 3-1. Signal flow graphs of (a) single add/drop ring, (b) two coupled rings, and (c) three coupled rings [69].

$$
\begin{aligned}
H_1(z) &= -\frac{c_1 c_2 A_2 z^{-1/2}}{1 - t_1 t_2 A_1 A_2 z^{-1}} \\
&= \frac{c_1 c_2 A_2 e^{-\frac{1}{2} j\omega\tau}}{1 - t_1 t_2 A_1 A_2 e^{-j\omega\tau}} \\
&= \frac{c_1 c_2 A_2}{e^{\frac{1}{2} j\omega\tau} - t_1 t_2 A_1 A_2 e^{-\frac{1}{2} j\omega\tau}}
\end{aligned}
\tag{3-1}
$$

where $z^{-1} = e^{-j\omega\tau}$, ω is the angular frequency, $\tau = n_{eff} L/c$ is a time constant, n_{eff} is the effective refractive index of the waveguide, L is the length of the ring resonator, c_i is the amplitude coupling value of the i^{th} coupler, $t_i = \sqrt{1 - c_i^2}$ is the cross coupling value assuming that there is no coupler insertion loss, φ_i is the phase introduced by the phase modulator in the i^{th} ring, and A_i is the fractional amplitude loss/gain in each waveguide segment.

By tuning the gain in the ring resonator to make $t_1 t_2 A_1 A_2 \approx 1$ and assuming m=0, we have

$$
\begin{aligned}
H_1(\omega) &= \frac{c_1 c_2 A_2}{e^{\frac{1}{2} j\omega\tau} - e^{-\frac{1}{2} j\omega\tau}} \\
&= \frac{c_1 c_2 A_2}{2j \sin\left[\frac{1}{2}(\omega - \omega_0)\tau + m\pi\right]} \\
&\approx \frac{c_1 c_2 A_2/\tau}{j(\omega - \omega_0)}
\end{aligned}
\tag{3-2}
$$

where $\omega_0 = 2m\pi/\tau$ is the frequency of interests in one of the resonance frequencies, *m* is an arbitrary integer. As can be seen that a single add/drop ring resonator with a transfer function of (3-2) can be used to implement a first order integrator.

3.2.2. Second order integrator

A second order integrator can be implemented using two coupled add/drop ring resonators in the proposed signal processor, as shown in Fig. 3.1(b). The transfer function is given by [69]

$$\begin{aligned} H_2(z) &= \frac{jc_1c_2c_3A_2A_3z^{-1}}{1-B_1z^{-1}+B_2z^{-2}} \\ &= \frac{jc_1c_2c_3A_2A_3e^{-j\omega\tau}}{1-B_1e^{-j\omega\tau}+B_2e^{-2j\omega\tau}} \end{aligned} \tag{3-3}$$

where

$$B_1 = t_1t_2A_1A_2e^{-j\varphi_1} + t_2t_3A_3A_4e^{-j\varphi_2} \tag{3-4}$$

$$B_2 = t_1t_3A_1A_2A_3A_4e^{-j(\varphi_1+\varphi_2)} \tag{3-5}$$

By tuning the gain, coupling, and phase in each ring resonator we can have (3-3) written as

$$
\begin{aligned}
H_2(\omega) &= \frac{jc_1c_2c_3A_2A_3}{\left[e^{-\frac{1}{2}j\omega\tau} - e^{\frac{1}{2}j\omega\tau}\right]^2} \\
&= \frac{jc_1c_2c_3A_2A_3}{\left\{2j\sin\left[\frac{1}{2}(\omega-\omega_0)\tau + m\pi\right]\right\}^2} \\
&\approx \frac{jc_1c_2c_3A_2A_3/\tau^2}{\left[j(\omega-\omega_0)\right]^2}
\end{aligned}
\tag{3-6}
$$

As can be seen that two coupled add/drop ring resonators with a transfer function of (3-6) can be used to implement a second order integrator.

3.2.3. Third order integrator

A third order integrator can be implemented using three coupled add/drop ring resonators in the proposed signal processor, as shown in Fig. 3.1(c). The transfer function is given by [69],

$$
H_3(z) = \frac{c_1c_2c_3c_4A_2A_3A_6z^{-3/2}}{1 - D_1z^{-1} + D_2z^{-2} + D_3z^{-3}} \tag{3-7}
$$

where

$$D_1 = t_1 t_2 A_1 A_2 e^{-j\varphi_1} + t_2 t_3 A_3 A_4 e^{-j\varphi_2} + t_3 t_4 A_5 A_6 e^{-j\varphi_3} \tag{3-8}$$

$$D_2 = t_1 t_3 A_1 A_2 A_3 A_4 e^{-j(\varphi_1+\varphi_2)} + t_2 t_4 A_3 A_4 A_5 A_6 e^{-j(\varphi_2+\varphi_3)} + t_1 t_2 t_3 t_4 A_1 A_2 A_5 A_6 e^{-j(\varphi_1+\varphi_3)} \tag{3-9}$$

$$D_3 = -t_1 t_4 A_1 A_2 A_3 A_4 A_5 A_6 e^{-j(\varphi_1+\varphi_2+\varphi_3)} \tag{3-10}$$

Similarly, by tuning the gain, coupling, and phase in each ring resonator to achieve $t_1,\ t_2,\ t_3,\ t_4 \approx 1$ and $A_1,\ A_2,\ A_3,\ A_4 \approx 1$ we can rewrite (3-7) as

$$H_3(\omega) \approx \frac{c_1 c_2 c_3 c_4 A_2 A_3 A_6 / \tau^3}{\left[j(\omega - \omega_0) \right]^3} \tag{3-11}$$

As can be seen that three coupled add/drop ring resonators with a transfer function of (3-11) can be used to implement a third order integrator.

3.3 Photonic Fractional Differentiators

A fractional differentiator can be implemented using an MZI. Assuming that τ is the relative time delay between the two MZI arms, the transfer function can be written as [41]

$$H(z) = 1 + z^{-1} = 1 + e^{-j\omega\tau} \tag{3-12}$$

where $z^{-1} = e^{-j\omega\tau}$. By setting the interferometer to operate at a minimum transmission at the frequency of interest ($H(\omega_0) = 0$), we have

$$\tau = \frac{(2m+1)\pi}{\omega_0} \tag{3-13}$$

where *m* is an arbitrary integer. (3-12) can then be rewritten as

$$
\begin{aligned}
H\left(\omega-\omega_0\right) &= 1+e^{-j\omega\tau} \\
&= 1+e^{-j\left(\omega-\omega_0\right)\tau}e^{j\omega_0\tau} \\
&= 1-e^{-j\left(\omega-\omega_0\right)\frac{(2m+1)\pi}{\omega_0}} \\
&= 1-e^{-j(2m+1)\pi\frac{\omega-\omega_0}{\omega_0}} \\
&= 1-\cos\left[\left(2m+1\right)\pi\frac{\omega-\omega_0}{\omega_0}\right]+j\sin\left[\left(2m+1\right)\pi\frac{\omega-\omega_0}{\omega_0}\right]
\end{aligned}
\tag{3-14}
$$

The above function can be approximated over a sufficiently narrow bandwidth $\Delta\omega$ centered at $\omega=\omega_0$ to the following ($\frac{\omega}{\omega_0}\approx 1$, $\sin\left[\left(2m+1\right)\pi\frac{\omega-\omega_0}{\omega_0}\right]\approx\left(2m+1\right)\pi\frac{\omega-\omega_0}{\omega_0}$, and $\cos\left[\left(2m+1\right)\pi\frac{\omega-\omega_0}{\omega_0}\right]\approx 1$.)

$$
\begin{aligned}
H\left(\omega-\omega_0\right) &\approx j\frac{\left(2m+1\right)\pi}{\omega_0}\left(\omega-\omega_0\right) \\
&= j\tau\left(\omega-\omega_0\right)
\end{aligned}
\tag{3-15}
$$

As can be seen an MZI with a transfer function of (3-15) can be used to implement a differentiator (2-3).

3.4 Photonic Hilbert Transformers

A fractional Hilbert transformer can be implemented using a single ring resonator, as shown in Fig. 3-2. The transfer function is given by [69],

$$H_{1t}(z) = \frac{t_1 - t_2 A_1 A_2 z^{-1}}{1 - t_1 t_2 A_1 A_2 z^{-1}} = \frac{t_1 - t_2 A_1 A_2 e^{-j\omega\tau}}{1 - t_1 t_2 A_1 A_2 e^{-j\omega\tau}} \tag{3-16}$$

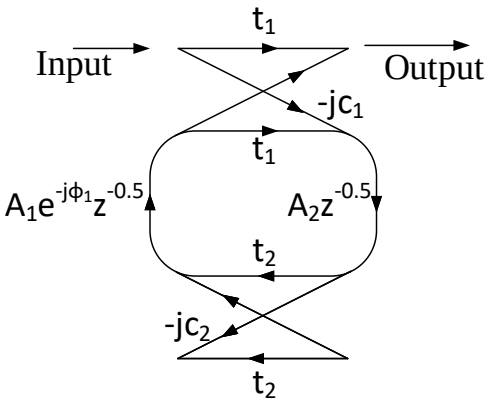

Fig. 3-2. Signal flow graphs of a single ring rings [69].

Since the loss in the ring resonator can be compensated by the gain provided by the SOAs, $t_2 A_1 A_2$ is close to unity, thus we have (3-16) rewritten as

$$
\begin{aligned}
H_{1t}(\omega) &\approx \frac{t_1 - e^{-j\omega\tau}}{1 - t_1 e^{-j\omega\tau}} \\
&= -\frac{e^{-\frac{1}{2}j\omega\tau} - t_1 e^{\frac{1}{2}j\omega\tau}}{e^{\frac{1}{2}j\omega\tau} - t_1 e^{-\frac{1}{2}j\omega\tau}} \\
&= \left|H_{1t}(\omega)\right| e^{j\Psi(\omega)}
\end{aligned}
\tag{3-17}
$$

As can be seen from (3-17), the numerator, $e^{-\frac{1}{2}j\omega\tau} - t_1 e^{\frac{1}{2}j\omega\tau}$, in the transfer function is the complex conjugate of the denominator, $e^{\frac{1}{2}j\omega\tau} - t_1 e^{-\frac{1}{2}j\omega\tau}$. Therefore, its magnitude response can be given as

$$
\left|H_{1t}(\omega)\right| = 1 \tag{3-18}
$$

and its phase response is written as

$$
\begin{aligned}
\Psi(\omega) &= \pi + 2\tan^{-1}\frac{(1+t_1)\sin\frac{1}{2}\omega\tau}{(1-t_1)\cos\frac{1}{2}\omega\tau} \\
&= \pi + 2\tan^{-1}\frac{(1+t_1)\sin\frac{\omega}{\omega_0}m\pi}{(1-t_1)\cos\frac{\omega}{\omega_0}m\pi}
\end{aligned}
\tag{3-19}
$$

For simplicity, we set *m*=1, and we rewrite (3-19) as

$$\Psi(\omega) = \pi + 2\tan^{-1}\frac{(1+t_1)\sin\frac{\omega}{\omega_0}\pi}{(1-t_1)\cos\frac{\omega}{\omega_0}\pi} \tag{3-20}$$

When $\omega \approx \omega_0$ with $\omega < \omega_0$, we have

$$\tan^{-1}\frac{(1+t_1)\sin\frac{\omega}{\omega_0}\pi}{(1-t_1)\cos\frac{\omega}{\omega_0}\pi} < 0 \tag{3-21}$$

When $\omega \approx \omega_0$ with $\omega > \omega_0$, we have

$$\tan^{-1}\frac{(1+t_1)\sin\frac{\omega}{\omega_0}\pi}{(1-t_1)\cos\frac{\omega}{\omega_0}\pi} > 0 \tag{3-22}$$

As can be seen from (3-20), (3-21), and (3-22), there is a phase change at frequency $\omega = \omega_0$, and the phase change amount can be controlled by t_1. Therefore, the through port of the ring resonator can be used to implement a fractional Hilbert transformer (2-4). By varying the coupling coefficient t_1, different values of the fractional order are achieved.

3.4 Summary

In this chapter, the principle of implementing a photonic temporal integrator based on a single or couple ring resonator, a photonic temporal differentiator based on an MZI, and a Hilbert transformer based on a single ring resonator was presented. The expressions for the transfer functions of the above mentioned functions were developed and the design of optical geometries for implementing such photonic signal processors was also provided.

Chapter 4

Photonic Temporal Signal Processing Based on a III-V Single Ring Resonator

4.1 Single Ring Signal Processing Introduction

In this chapter, a photonic temporal integrator with an ultra-wide integration time window implemented based on a PIC in an III-V material system consisting of SOAs and current-injection PMs is proposed and experimentally demonstrated. The proposed photonic integrated integrator employs a ring structure coupled with two bypass waveguides. The tunable coupling between the ring and the waveguides is realized by a MMI MZI coupler. Within the ring, two SOAs are incorporated to compensate for the insertion loss. In addition, there is a current injection PM in the ring for wavelength tuning. The use of the device provides a photonic temporal integrator with an ultra-wide integration time window and a tunable operation wavelength in a single PIC. The proposed integrator is fabricated and experimentally verified. The integration time window as wide as 6331 ps is achieved, which is an order of magnitude longer than that provided by the previously reported photonic integrators. A continuously tunable fractional Hilbert transformer based on the single ring resonator is also proposed and experimentally demonstrated.

4.2 Photonic Temporal Integration

4.2.1 Principle

Mathematically, a temporal integrator can be implemented using a linear time-invariant filter with a transfer function given by (2-1). A general approach to realizing a photonic integrator is to use an optical resonant cavity, for example, a FP filter [19] or a ring resonator [34, 35]. Fig. 4-1 shows a photonic temporal integrator based on a microring resonator. Three output temporal waveforms corresponding to three input waveforms of a Gaussian pulse, an in-phase doublet, and an out-of-phase doublet are shown to demonstrate the integration operation. The detailed theoretical analysis of using ring resonators to implement an optical integrator can be found in [27]. However, the integration time window of such an integrator is limited, and its operation wavelength is usually fixed. To implement a photonic integrator with an ultra-long integration time window and a tunable operation wavelength, we propose to use an active ring resonator incorporating SOAs and current injection PMs, as shown in Fig. 4-2.

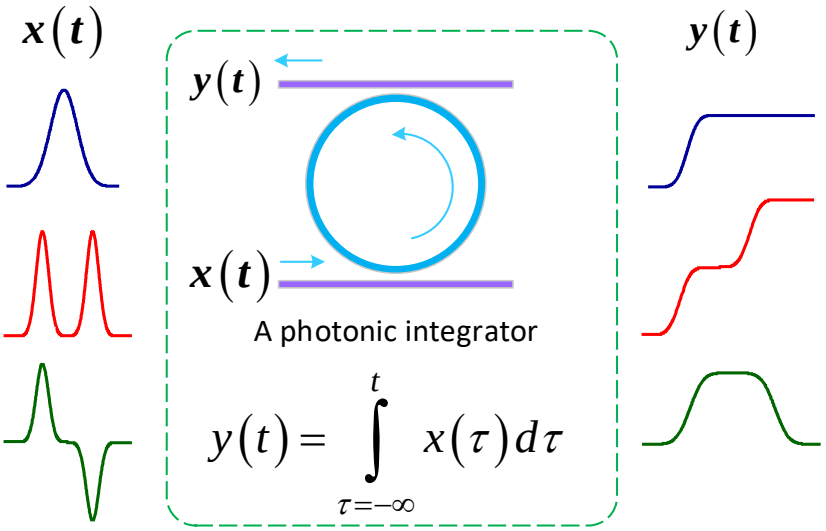

Fig. 4-1. The schematic diagram of a photonic temporal integrator based on a microring resonator.

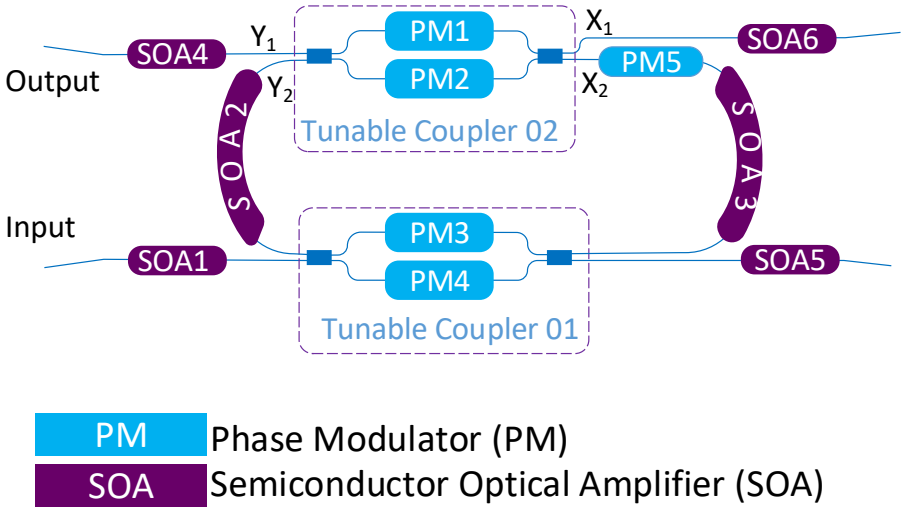

Fig. 4-2. The schematic of the proposed on-chip photonic temporal integrator based on a microring resonator.

The frequency response at the drop port of the ring resonator as shown in Fig. 4-2 consists of a series of narrow passbands (transmission peaks) with two neighboring passbands separated by a free spectral range (FSR) determined by the length of the ring [70]. By locating the central frequency of the input signal at the center of one of the narrow passband, the temporal integral of the input signal can be obtained at the output of the ring. In our design, to achieve temporal integration with an ultra-long integration time window and a tunable working wavelength, two active SOAs (SOA2 and SOA3) and a current injection PM (PM5) are incorporated into the ring. By applying injection currents to the SOAs (SOA2 and SOA3), the insertion loss in the device can be totally compensated. By changing the injection current to the PM (PM5) in the ring resonator, the spectral response is laterally shifted, thus making the operating wavelength be tuned. In addition, the coupling between the ring and the bypass waveguides is achieved by two tunable couplers, with each having an MMI MZI structure consisting of one PM in each of the two arms (PM1 and PM2 for tunable coupler 01, and PM3 and PM4 for tunable coupler 2, as shown in Fig. 4-2). By changing the injection currents to the PMs in the tunable couplers, the coupling coefficients can be continuously tuned from 0% to 100%. To compensate for the fiber coupling losses, two other active SOAs (SOA1 and SOA4) are incorporated into the device at the input and output waveguides, respectively. In this way, a photonic temporal integrator with a high power efficiency and a continuously tunable operating wavelength can be achieved.

TABLE IV-I
PARAMETERS FOR THE SIMULATION

Symbol	Description	Value
λ	Central wavelength	1558 nm
c_1	Coupling coefficient of the input coupler	90% (0 - 100%)
c_2	Coupling coefficient of the output coupler	90% (0 - 100%)
l	Length of the ring	3 mm
n	Refractive index of the waveguide	3.67
α	Waveguide loss	2.3 dB/cm
ρ	Insertion loss of the tunable coupler	2 dB
g	Gain of each SOA	0 – 9.6 dB

Coupler coefficients are tunable from 0 to 100%, which are considered as the coupling coefficient from X_2 to Y_2 as shown in Fig. 4-2.

Theoretically, the transfer function of the proposed ring resonator through the drop port as shown in Fig. 4-2 is given by [71]

$$H(Z) = -\frac{c_1 c_2 \sqrt{\rho} Z^{-1}}{1 - t_1 t_2 \rho Z^{-1}} \tag{4-1}$$

where c_1 and c_2 are the field coupling coefficients of the two tunable couplers, t_1 and t_2 are the field transmission factors of the two tunable couplers, and ρ is the loss in the ring. If the insertion losses in the ring are completely compensated,

the *Q*-factor of the ring is infinite, and the integration time is infinitely long. For real implementations, however, it is too difficult to achieve a complete compensation for the losses without reaching the lasing threshold ($t_1 t_2 \rho = 1$). Thus, we discuss the integration time window when the *Q*-factor of the ring is tuned by changing the injection currents to the SOAs on the chip, to achieve a large *Q*-factor while ensuring the ring is not lasing. The *Q*-factor of the ring is given by [72]

$$Q = \omega_r \frac{\mathrm{T}_r}{\alpha L} = \omega_r \mathrm{NT}_r \tag{4-2}$$

where ω_r is the resonant angular frequency of the ring resonator, T_r is the round trip time in the ring, α is the power attenuation coefficient, L is the optical length of the ring, and *N* is the number of round trips required to reduce the optical power to $1/e$. The integration time window is defined as the time duration for the output power to drop by 20% from its maximum value [35]. A simulation is performed to analyze the integration performance for the ring to be configured to operate far from the lasing condition to close to the lasing condition. In the simulation, the integration time window is calculated based on the output temporal waveform, which is obtained by an inverse Fourier transform of the product of the input Gaussian pulse spectrum and the transfer function of the ring resonator with different *Q*-factors. The parameters in the simulation are given in Table IV-I. As shown in Fig. 4-3, the integration time window increases with the *Q*-factor. When

the ring is approaching to the lasing threshold or the *Q*-factor is approaching to infinity, the integration time window is then approaching to infinity. However, for practical implementation the ring resonator is very unstable when the gain is close to the lasing threshold, which prevents the proposed integrator from having an infinite integration time window.

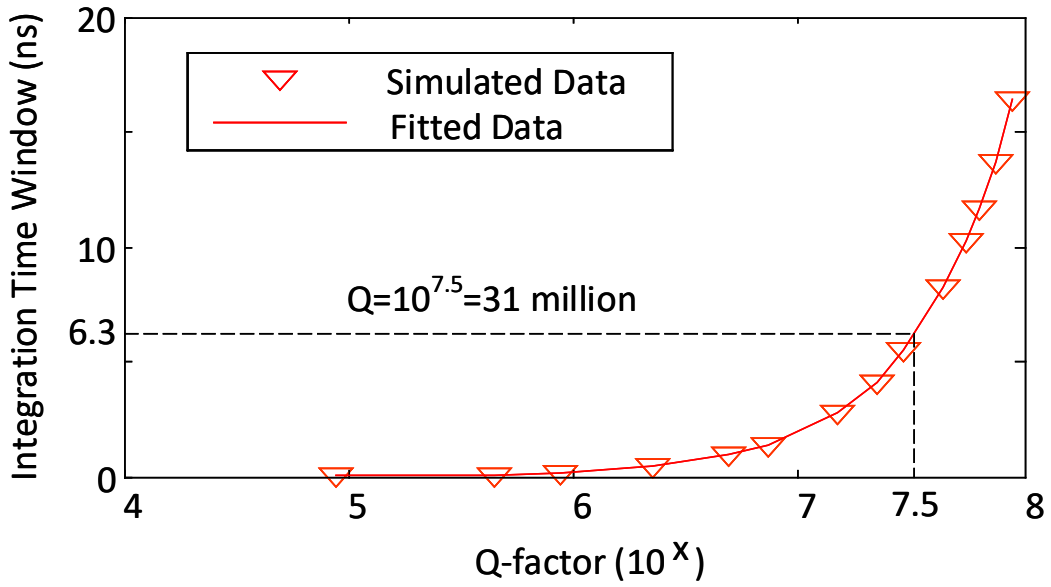

Fig. 4-3. Simulation results. The integration time window for different *Q*-factors of the ring.

4.2.2 Experimental Results

The proposed photonic temporal integrator is fabricated in an InP-InGaAsP material system by the UCSB nanofabrication facility, as shown in Fig. 4-4(a), which is wire-bonded to a carrier for experimental demonstration, as shown in Fig. 4-4(b). The device epitaxial structure is described in the following. An n-doped layer is grown on top of the InP substrate, and a waveguide layer is then grown on

top of the n-doped layer, which has a thickness of 300 nm, on top of which there is a confinement tuning layer (CTL) with a thickness of ~250 nm. For an SOA, there are 5 quantum wells (QWs) grown on top of the CTL, which pushes the QWs away from the waveguide layer to reduce the confinement factor and improve the saturation power. The QW layer is covered by a Zn p-doped layer with a thickness of 1.7 μm. For a passive waveguide, the CTL is covered by the p-doped layer without the QWs. For a PM, the p-doped layer is grown on top of the waveguide layer without the CTL and the QWs. For both the active and passive regions, there is a 150-nm contact layer on top of the p-doped layer, the contact layer is covered by a p-cap layer for the passive waveguides and by a metal layer for the active regions.

The chip size is 1 mm x 2 mm, and the comparison of its size with a Canadian penny is shown in Fig. 4-4(c). In the prototype, the length of the deeply etched waveguide ring is 3 mm. Two 400-μm SOAs (SOA2 and SOA3) with a confinement tuning layer offset quantum well (CTL-OQW) [73] structure are fabricated in the ring to provide a peak gain of 9.6 dB per SOA. With 3 mm of ring length subtracting the length of two SOAs (400 μm each) and 2.3 dB/cm of passive waveguide loss, the total waveguide propagation loss is 1.6 dB. For a ring with a coupling coefficient of 90% and 0.5 dB MMI insertion loss, the couplers add about 2 dB of loss for a total round-trip loss of 3.6 dB, which is compensated for by the two SOAs. Two

additional active SOAs (SOA1 and SAO4) are incorporated into the system at both the input and output waveguides to compensate for the fiber coupling losses, as shown in Fig. 4-4(a). In addition, the facets of the waveguides are angled at 7^{o} to minimize the reflections. The phase modulation in the ring and the tuning of the MMI MZI coupler are accomplished by forward bias currents via current injection and free carrier absorption through the carrier plasma effect in the PMs. The PMs (PM01-PM05) in the chip are fabricated with a standard length of 300 μm.

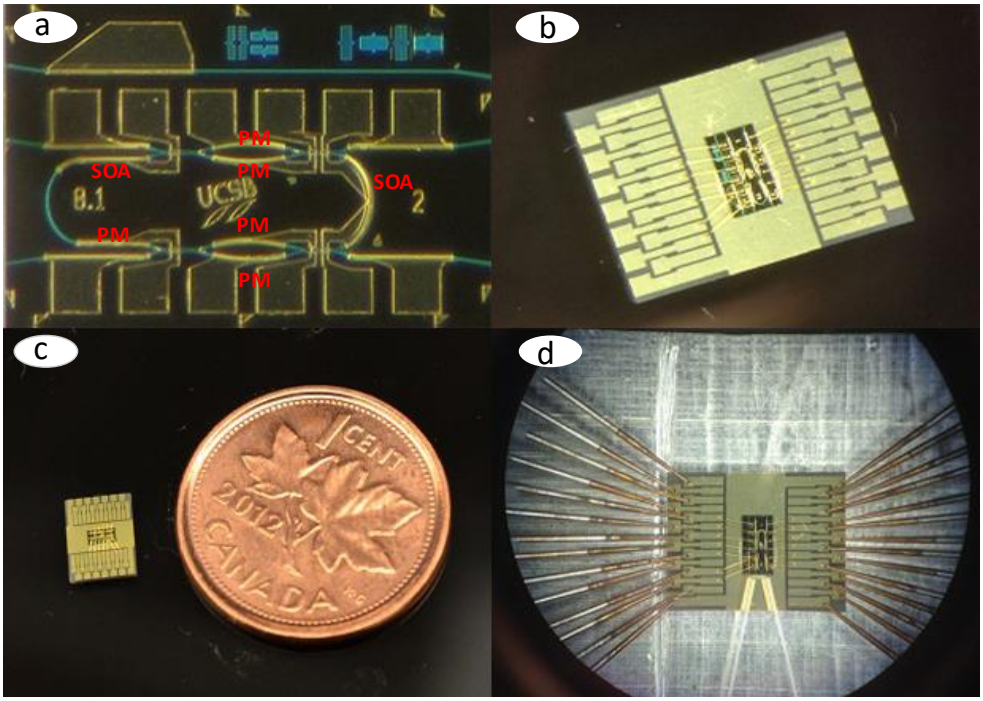

Fig. 4-4. (a) The fabricated on-chip photonic temporal integrator prototype. (b) Wire bonded to a carrier. (c) Comparison with a Canadian penny. (d) Experimental setup for optical coupling with two lensed fibers.

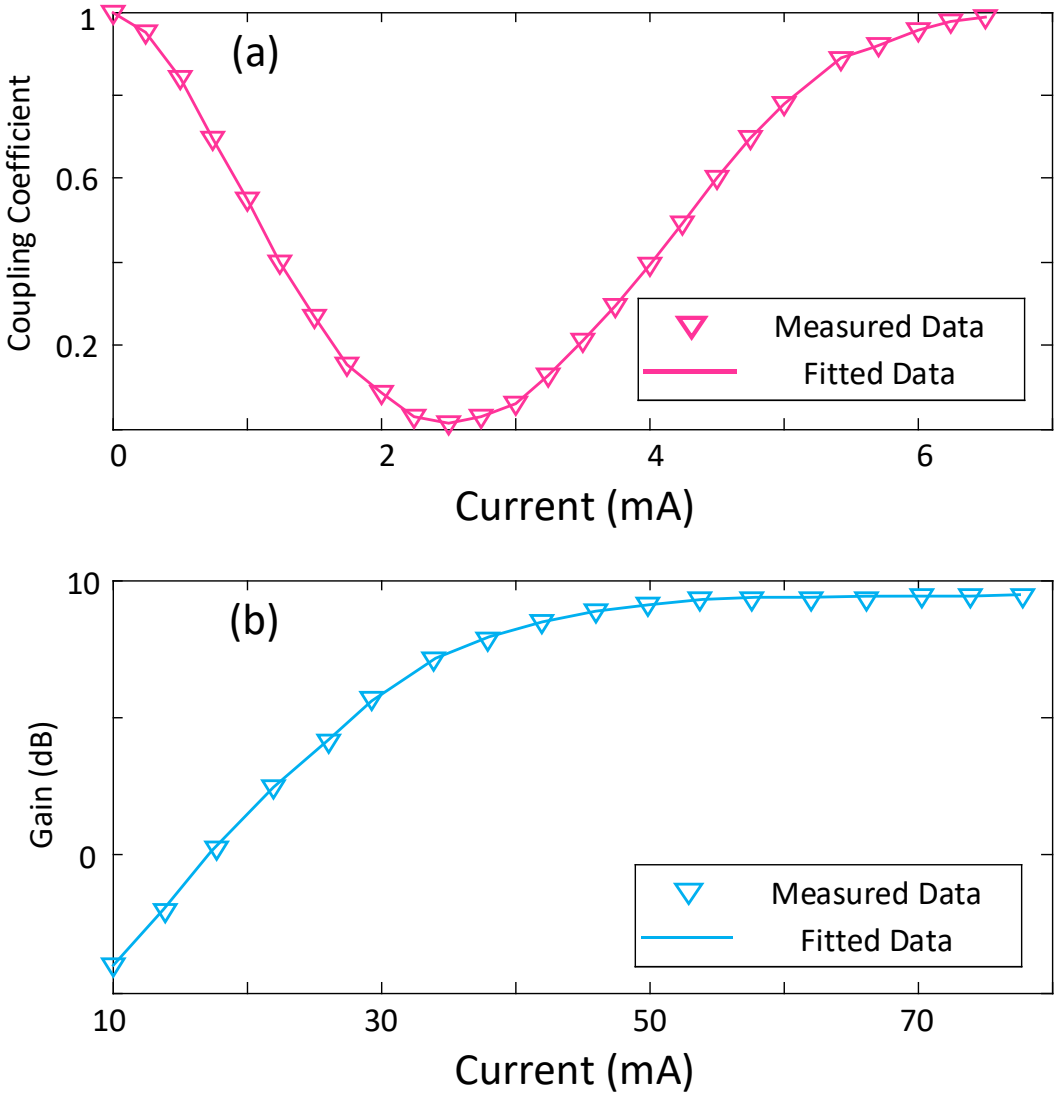

Fig. 4-5. (a) Tunable coupling coefficient of an MMI MZI coupler at different injection current of one PM on one of the two arms. (b) The gain profile of an SOA as a function of the injection current.

The coupling coefficients of the tunable couplers are measured at different injection currents to the PMs, which can be controlled from 0 to 100% when one of the PMs in each of the tunable couplers is injected with a current from 0 to 3.5 mA. Fig. 4-

5(a) shows the measured coupling coefficient of tunable coupler 2 as a function of the injection current to PM2, from 0 to 6.5 mA. The large signal gain profile of an SOA is also measured. As can be seen the SOA has a maximum gain of 9.6 dB when the injection current is above 70 mA, as shown in Fig. 4-5(b). The FSR of the on-chip ring is measured to be 27.2 GHz as shown in Fig. 4-6(a). By changing the injection current to the PM (PM5) in the ring, the spectral response of the ring is laterally shifted, thus the notch location is also shifted, as shown in Fig. 4-6(b). In the experiment, the chip is working at 22 ^{o}C with a temperature controlling unit to maximize the stability of the ring resonator.

As discussed in Chapter 4.2, the *Q*-factor is a critical parameter to the operation of the integrator. In the experiment, we also test the operation of the integrator when it is configured to operate close to the lasing threshold, with the injection currents to the PMs and the SOAs given in Table IV-II. Under this condition of operation, three different input waveforms are generated and applied to the input of the integrator, to study the performance of the integration operation of the device.

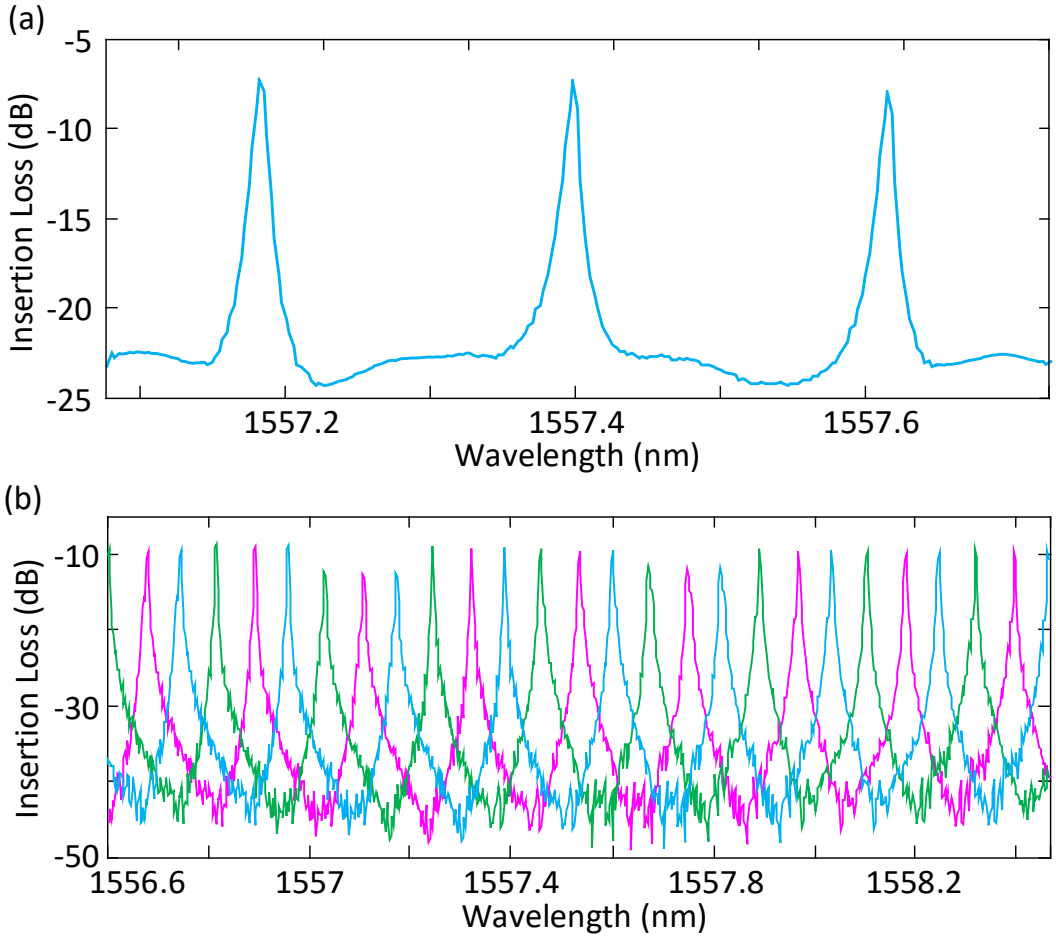

Fig. 4-6. The measured spectra response of the fabricated ring resonator. (a) The spectra response without injection current to the PM in the ring. (b) The spectral response of the integrator when the injection current to the PM in the ring is tuned at three different currents.

TABLE IV-II

THE INJECTION CURRENTS TO THE PMS AND SOAS

Components	Integrator	Lasing Condition
SOA01	50.000 mA/2.4992V	N/A
SOA02	28.300 mA/2.1197V	39.800 mA/2.3012V
SOA03	34.202 mA/2.4209V	34.202 mA/2.4209V
SOA04	50.000 mA/2.4644V	N/A
PM01	0	0
PM02	3.7867 mA/1.7758V	3.7867 mA/1.7758V
PM03	2.1291 mA/1.7361V	2.1291 mA/1.7361V
PM04	0	0

A. Gaussian Pulse

We first test the integration of a Gaussian pulse by the photonic temporal integrator. The Gaussian pulse is generated by a mode locked laser (MLL) source which is filtered by an optical bandpass filter (Finisar, WaveShaper 4000S) with a bandwidth of 0.12 nm and a central wavelength at 1557.4 nm, as shown in Fig. 4-7(a), to make the Gaussian pulse have a temporal width of 54 ps centered at 1557.4 nm, which is then coupled into the photonic integrator by a lensed fiber. By configuring the photonic temporal integrator with the injection currents to the SOAs and PMs in the

ring with the values given in Table IV-II, a high *Q*-factor of 31 million is achieved and the ring is still under the lasing threshold. As shown in Fig. 4-7(b), the temporal integral of the input Gaussian pulse is realized. The integration window is measured to be 6331 ps.

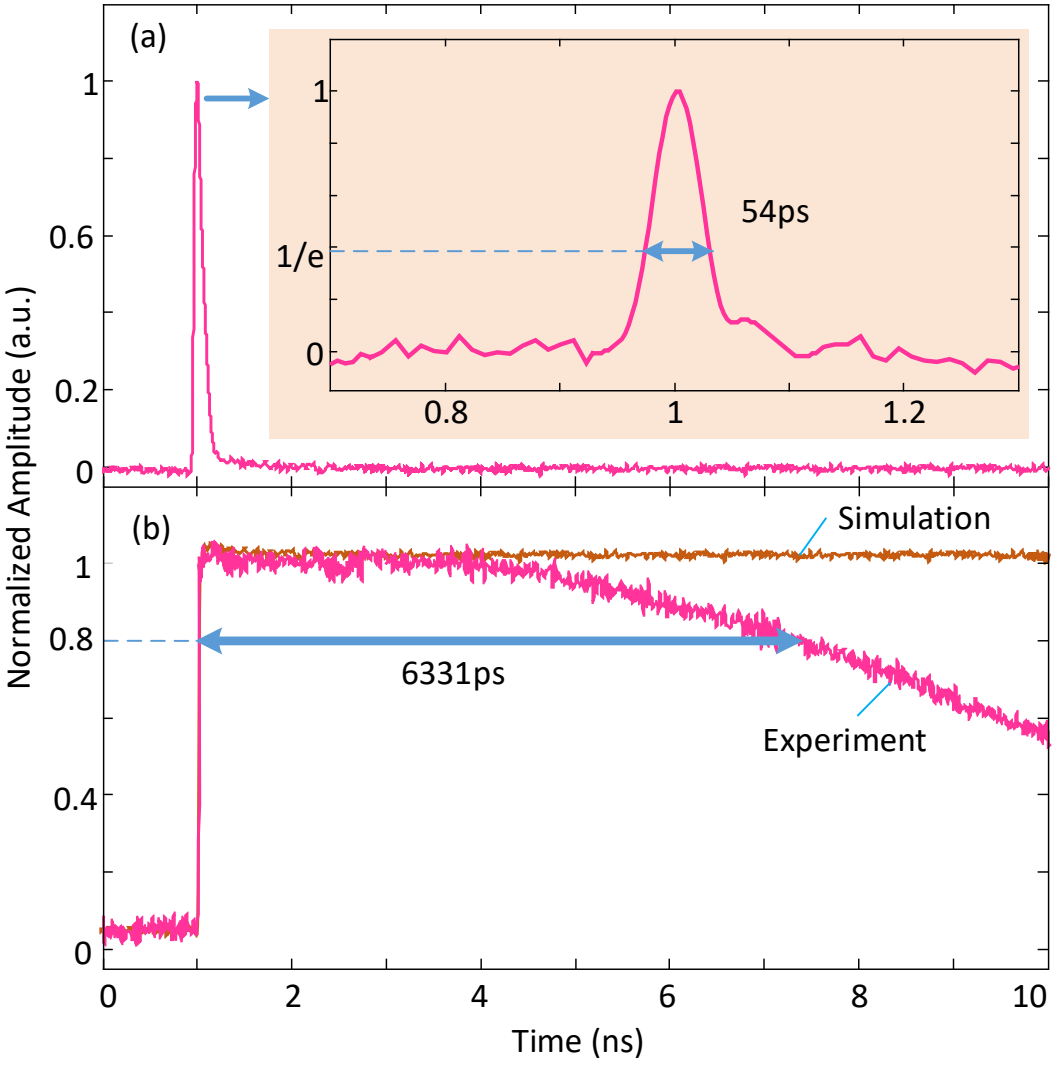

Fig. 4-7. The experimental results. (a) The input Gaussian pulse with a temporal width of 54 ps. (b) The integral of the Gaussian pulse with an integration time window of 6331 ps.

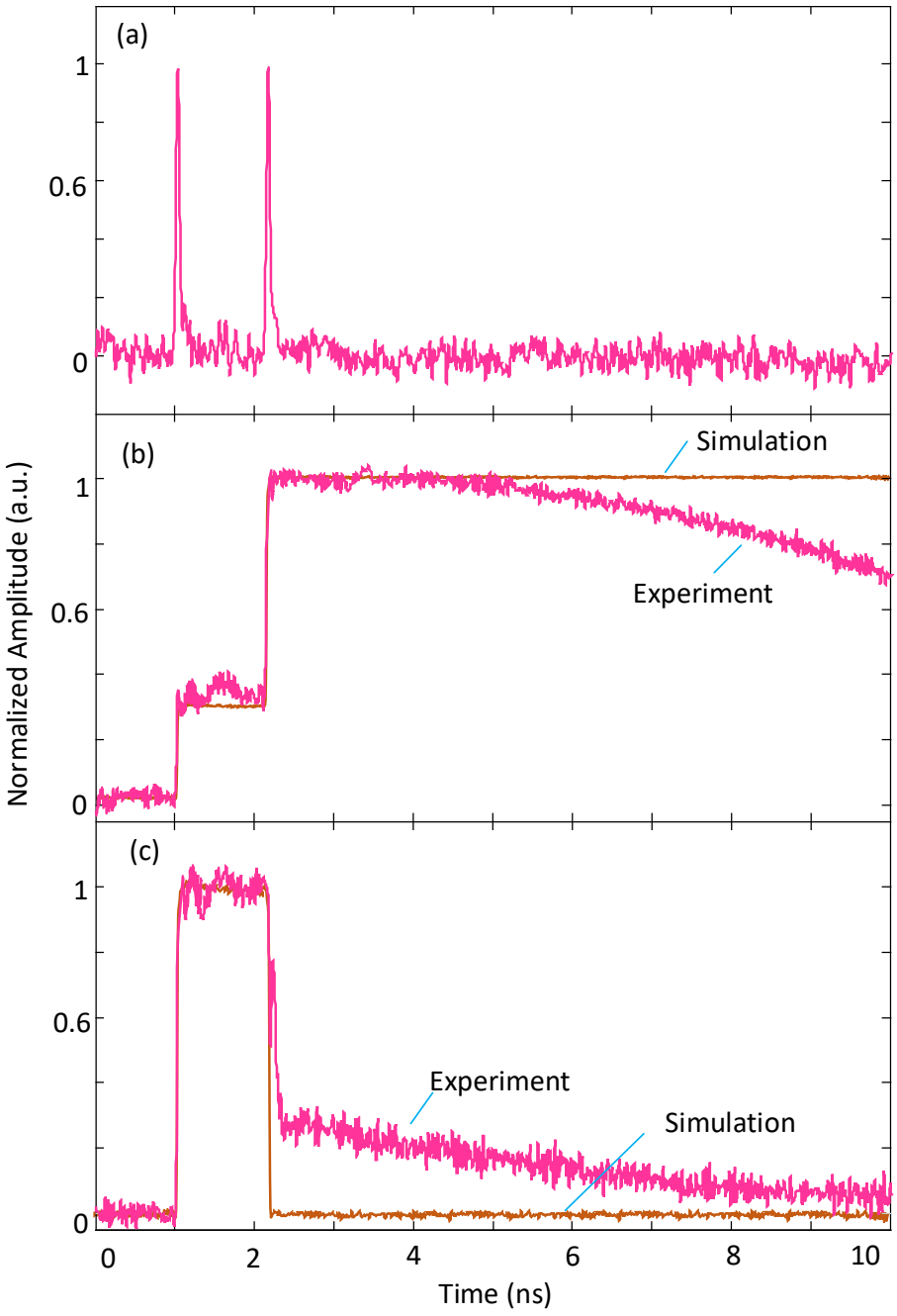

Fig. 4-8. The experimental results. (a) The input in-phase doublet pulse, (b) the integral of the in-phase doublet pulse, and (c) the integral of the out-of-phase doublet pulse.

B. In-phase Doublet

We then test the integration of an in-phase doublet pulse by the proposed photonic temporal integrator. In the experiment, the in-phase doublet pulse is generated by launching a Gaussian pulse into an unbalanced MZI with a length difference between the two arms of 25 cm. As a result, two closely separated pulses, called an in-phase doublet, with a temporal separation of 1.14 ns, as shown in Fig. 4-8(a), are generated and then launched into the integrator. The waveform at the output of the integrator is shown in Fig. 4-8(b). As can be seen the integrator sums up the area of the in-phase doublet, giving two steps corresponding the area of the first pulse and the area of the first and the second pulses, as shown in Fig. 4-8(b).

C. Out-of-phase Doublet

A photonic temporal integrator can be used as a memory device. The ability to reset the memory is a very important function. To validate the operation of the integrator as a memory unit, two closely separated pulses with a π phase shift (out-of-phase), called an out-of-phase doublet, generated by the same unbalanced MZI mentioned are coupled into the input port of the integrator. The π phase shift between the two pulses is introduced by the MZI by controlling the length difference between the two arms of the MZI. The waveform at the output of the integrator is shown in Fig. 4-8(c). As can be seen memory resetting function is performed by the integrator.

D. Discussion

To utilize the proposed integrator as a processing unit in a large system, the power consumptions of the PMs and SOAs and the amplified spontaneous emission (ASE) noise from the SOAs should be considered. In the experiment, the total power consumption of the integrator is 401 mW including 248 mW consumed by the input/output SOAs, which can be avoided in a large system with all units fabricated on a single chip without fiber coupling loss between the units. In addition, a single SOA in a ring resonator is enough to compensate for the total loss. Therefore, a power consumption with a single SOA in a ring resonator and two PMs for tunable coupling would have a power consumption of 93 mW, which is much smaller than the power consumption of the single integrator demonstrated here. When the number of SOAs is reduced, the ASE noise will also be significantly reduced.

4.3 Photonic Temporal Hilbert Transformation

4.3.1 Principle

The ideal transfer function $H_n(\omega)$ of an FHT with an order *n* is given in (2-4). The FHT becomes a conventional HT when $n=1$. For $n=0$, we have $H_0(\omega)=1$, which means that the signal at the output of the transformer is identical to the input signal. For $0<n<1$, the output is a weighted sum of the original signal and its conventional HT.

The FHT with tunable fractional order and central wavelength can be implemented based on a configuration shown in Fig. 4-2, which has a ring structure incorporating two active SOAs and a current injection PM. The frequency response of the ring in Fig. 4-2 can be considered as a periodical narrow-notch filter with its phase response determined by the coupling coefficient between the ring and the waveguide and its FSR determined by the length of the ring. By locating the central frequency of the input signal at one of these notch filters, an FHT of the input signal can be operated with its fractional order determined by the phase response of the notch filter. In our design, to achieve an FHT with a tunable fractional order and operating wavelength, the phase response of the notch filter is achieved by a tunable coupler between the ring and the waveguide, which is realized by the MMI MZI coupler in the configuration. By changing the injection current to the PMs in the tunable coupler, the coupling coefficient can be continuously tuned from 0% to 100%, which allows a continuously tunable fractional order from 0 to 1. In order to change the operating wavelength, the notch location of the FSR can be tuned by changing the injection current into the PM in the ring. In this way, an FHT with continuously tunable fractional order and operating wavelength can be achieved. To compensate for the propagation loss and the MMI splitting loss, there are two active SOAs in the ring, and two additional active SOAs at both input and output waveguides are designed to compensate for the fiber coupling losses.

4.3.2 Experimental Results

An experiment to validate the FHT is implemented. It is worth to mention, the output port in the ring resonator for the FHT is the through port, which is different from the differentiator with the output port located at the drop port. The FSR of the on-chip FHT is measured to be 27.2 GHz by an optical vector analyzer (Luna OVA) as shown in Fig. 4-9(a). By changing the injection current of the PM in the ring, the notch location of the FSR is tuned and the FSR is slightly changed; the phase response corresponding to the fractional order of the FHT can also be tuned by changing the coupling coefficient as shown in Fig. 4-9(b), which is achieved by changing the injection current to the PMs in the tunable MMI MZI coupler. To validate the operation of the FHT, a spectrally tailored Gaussian pulse train as shown in Fig. 4-10(a) generated by a mode-locked laser (MLL) source (IMRA Femtolite 780) with its central frequency at 1559.1 nm and a bandwidth of 0.2 nm is coupled into the FHT chip. By changing the coupling coefficient through controlling the injection current to the PMs in the tunable coupler, the input signal is fractionally Hilbert transformed with a given fractional order from 0.05 to 1, as shown in Fig. 4-10(b) (c) (d) (e) (f). Since an arbitrary fractional order from 0 to 1 can be achieved, the fractional order of the proposed FHT can be continuously tunable from 0 to 1.

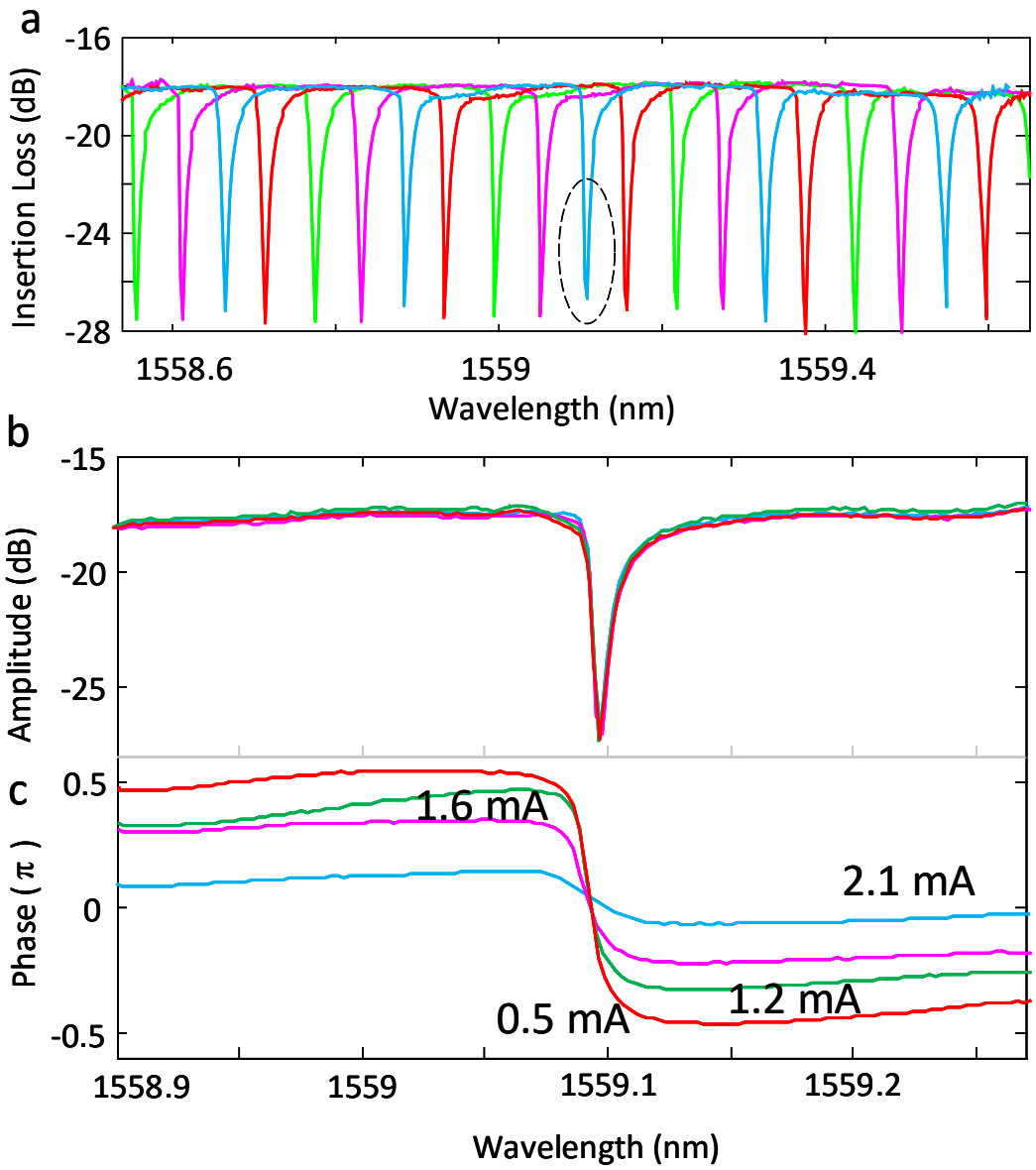

Fig. 4-9. (a) The spectral response of the proposed on-chip FHT at different injection current applied to the PM in the ring (Green, magenta, blue, and red: 0, 1.5 mA, 3.0 mA, and 4.5 mA). (b) The spectral and (c) phase responses of a selected notch at different coupling coefficient.

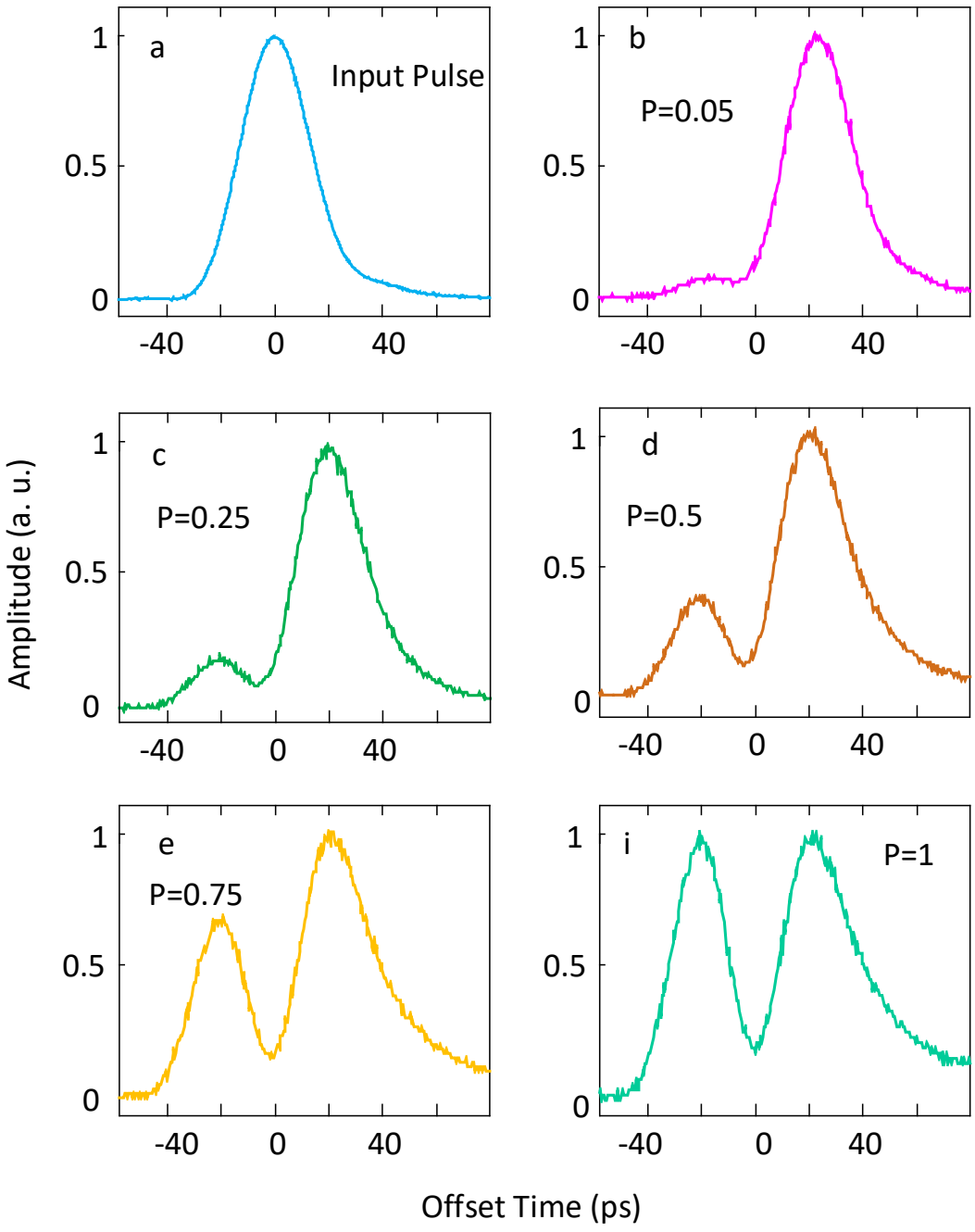

Fig. 4-10 (a) Input signal. FHT signal with a fractional order of 0.05 (b), 0.25 (c), 0.5 (d), 0.75 (e), and 1 (f).

4.4 Summary

A photonic integrated temporal integrator that provides an ultra-long integration time window and a continuously tunable working wavelength on a single PIC was proposed and experimentally demonstrated. A temporal integration window of 6331 ps with a bandwidth of 0.12 nm was obtained, which is far better than an electronic integrator. Compared with the previously reported photonic solutions, the proposed integrator provides an integration time window that is an order of magnitude longer. The temporal integration of different input waveforms was also investigated, which confirmed the effective operation of the proposed temporal integrator. This work represents an important step towards the realization of efficient optical signal-processing circuits capable of overcoming the limitation in the integration time window, bandwidth and power consumption imposed by electronics.

A photonic integrated FHT based on the proposed ring resonator was also experimentally demonstrated, which provides both continuously tunable fractional order and tunable operation wavelength on a chip-scale device.

Chapter 5

Photonic Temporal Signal Processing Based on III-V Coupled Ring Resonators

5.1 Principle

In Chapter 4, a photonic signal processor based on a single ring resonator was demonstrated to function as a photonic temporal integrator and a Hilbert transformer, which presented high application performance. However, the optical geometry of the photonic processor cannot be reconfigured once it is fabricated.

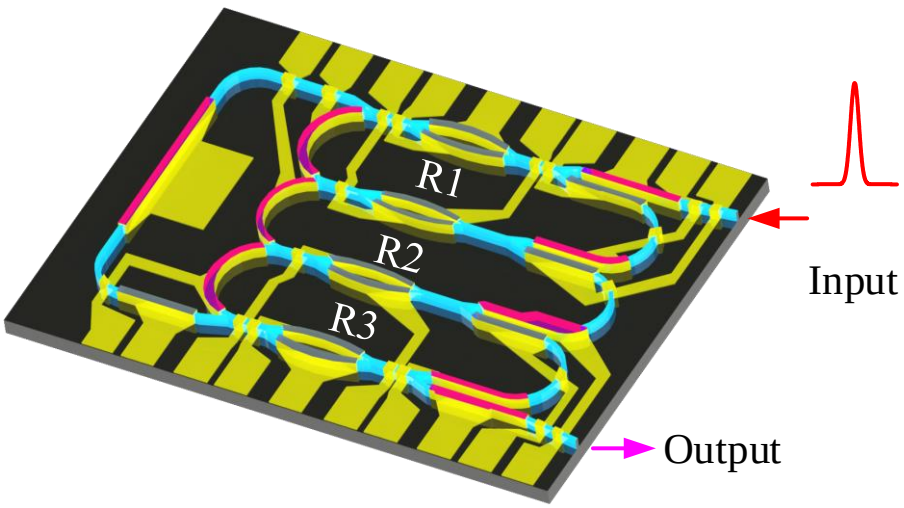

Fig. 5-1. The schematic diagram of the photonic integrated signal processor as a unit cell.

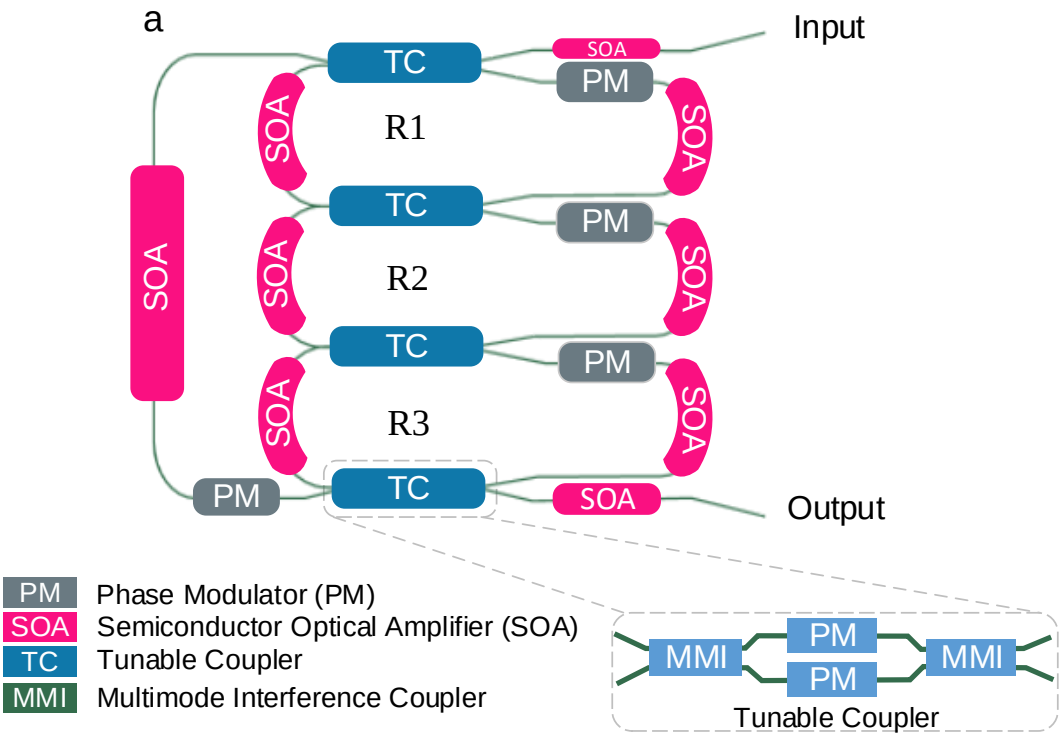

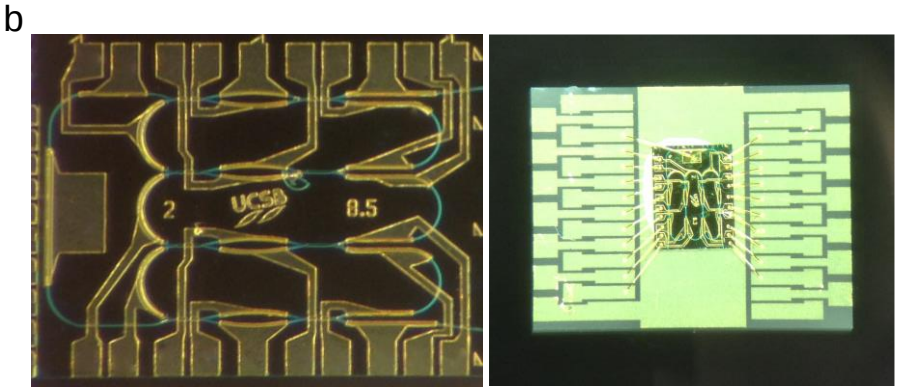

Fig. 5-2. (a) A schematic representation of the photonic integrated signal processor consisting of three coupled rings and a bypass waveguide. (b) The fabricated on-chip photonic signal processor prototype. The lower image shows the chip wire bonded to a carrier for experimental test.

In this chapter, a fully reconfigurable photonic integrated signal processor is reported, which includes the design, fabrication and experimental demonstration. The photonic signal processor consists of three active microring resonators (R1, R2, and R3) and a bypass waveguide as a processing unit cell, as shown in Fig. 5-1(a) and Fig. 5-2(a).

To obtain on-chip reconfigurability, we incorporate nine SOAs and twelve current-injection PMs in the unit cell, as shown in Fig. 5-2(a). The tunable coupling between two neighboring rings and between the outer ring and the bypass waveguide is realized using four TCs with each consisting of two MMI couplers and two PMs, as shown in the inset in Fig. 5-2(a). The coupling ratio in each TC can be tuned by adjusting the injection currents to the two PMs in the TC. Within each ring, there are two SOAs used to compensate for the waveguide propagation loss, and the MMI splitting loss and insertion loss. When an SOA is forward biased, it can create an optical gain. On the other hand, an SOA can operate as an optical absorber when it is reverse biased, which is the key to achieve the configurability of the processor. Consequently, with the SOAs utilized in this design, a waveguide path could effectively be on or off to facilitate the synthesis of various circuit geometries. By reverse biasing one SOA in each of the three ring resonators, for example, the three mutually coupled rings are reduced to a single optical path. With the bypass waveguide incorporated in the design, the chip can be reconfigured as a MZI. The

signal processing functions including temporal integration, temporal differentiation, and Hilbert transformation can be implemented by configuring the unit cell with a specific geometry. In addition, there is a current-injection PM in each ring resonator, and a PM in the bypass waveguide, which are used to achieve wavelength tunability. Furthermore, the order of the signal processor, either a fractional or higher order, can be tuned by tuning the coupling ratio of the TC. The actually fabricated device is shown in Fig. 5-2(b), which is wire-bonded to a carrier to enable an easily access to the SOAs and PMs with the assistance of a customized probe station. In the following, the proposed integrated photonic signal processor reconfigured to achieve three different functions for fast signal processing is discussed.

5.1.1 Photonic temporal integrator

An *n*th-order temporal integrator is a linear time-invariant (LTI) system with a transfer function given by (2-2). A first-order photonic temporal integrator can be implemented using an optical resonator, for example, an add-drop ring resonator [35]. If the input and drop ports are used, the ring resonator would have a spectral response that is close to that given in (2-2) for $n = 1$, and it is a first-order temporal integrator. A higher-order (with $n = 2, 3, \ldots$) temporal integrator can be implemented by cascading or coupling n first-order integrators [35]. An *n*th-order

temporal integrator is capable of calculating the *n*th time integral of an arbitrary optical waveform.

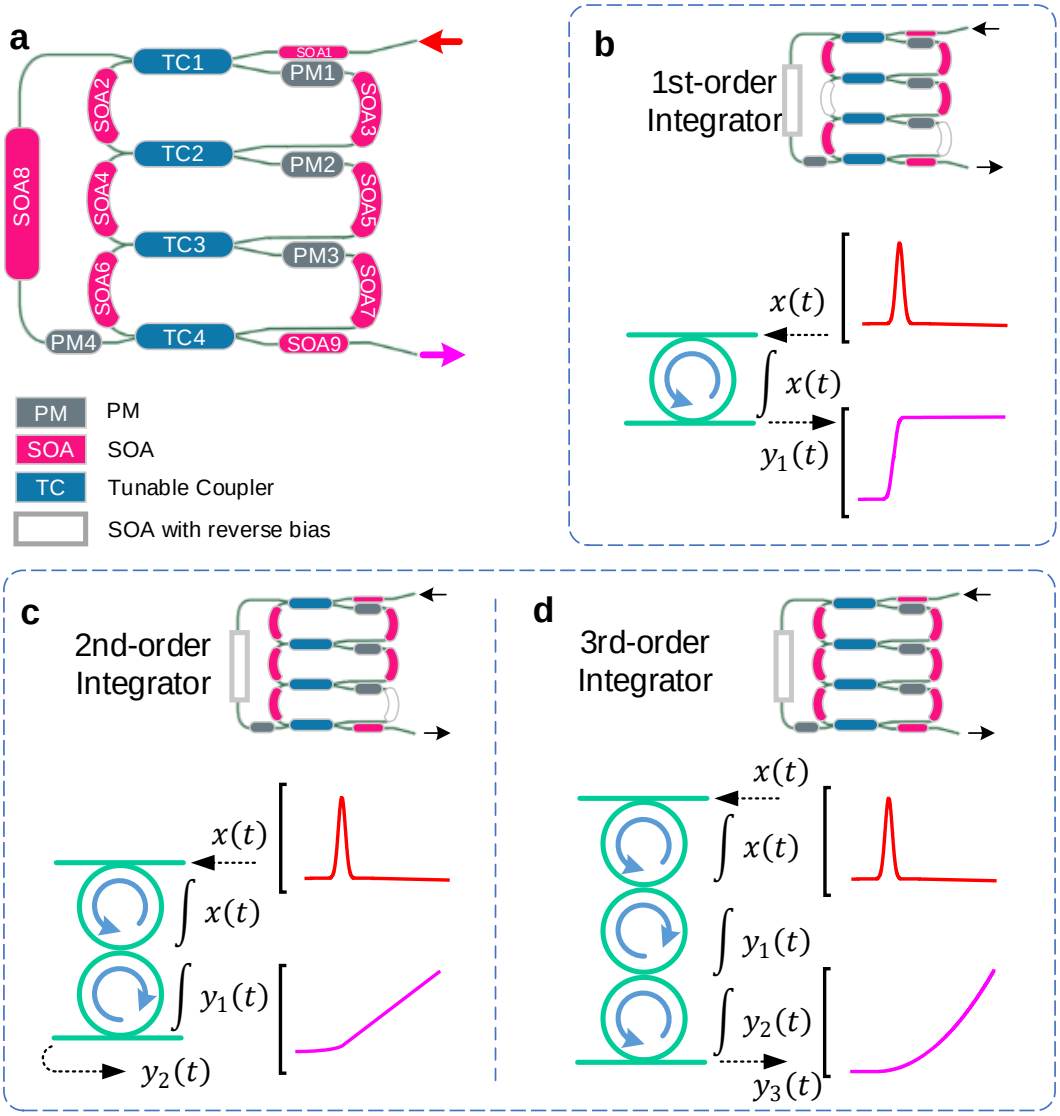

Fig. 5-3. (a) The general configuration of the signal processor is reconfigured as a (b) first-, (c) second-, and (d) third-order integrator.

The photonic integrated signal processor shown in Fig. 5-1 and Fig. 5-2 can be configured as a temporal integrator with an order of 1, 2 and 3, depending on the number of rings used as shown in Fig. 5-3. In the unit cell, there are three mutually coupled ring resonators with two active SOAs in each ring resonator. If one SOA in a ring resonator is reverse biased to shut off the waveguide, the ring resonator simply becomes a waveguide. By controlling the number of rings in the unit cell to be 1, 2 or 3, a temporal integrator with an order of 1, 2 or 3 is achieved as shown in Fig. 5-3. For example, a temporal integrator with an order of 1 is configured by shutting off two ring resonators, as shown in Fig. 5-2(a). In each ring resonator, a current injection PM is incorporated, which is used to tune the resonance frequency of the ring resonator, thus achieving wavelength tunability. In addition, the tunable coupling between two adjacent rings, and between an outer ring (R1 or R3) and the bypass waveguide, can offer tunable spectral response of the coupled-ring resonator, which can be used to achieve higher order integrators.

5.1.2 Photonic temporal differentiator

An *n*th-order temporal differentiator provides the *n*th order time derivative of the envelope of an optical signal. An *n*th-order temporal differentiator can be considered as an LTI system with a transfer function given by (2-3). An optical filter with a frequency response given by (2-3) can be implemented using an MZI

(24). By controlling the coupling coefficients of the input and output couplers in an MZI, a tunable phase shift from 0 to 2π can be achieved, thus a temporal differentiator with a tunable fractional order can be implemented. The photonic integrated signal processor shown in Fig. 5-1 can be configured to have an MZI structure as shown in Fig. 5-4. One arm of the MZI is formed by shutting off the three ring resonators in the unit cell, by applying a reverse bias to one of the two SOAs in each of the three ring resonators. The other arm is the bypass waveguide. The tuning of the fractional order is achieved by changing the coupling coefficients at both the input and output couplers. The operation wavelength can also be tuned, which is done by tuning the injection current applied to the PM in one of the MZI arms.

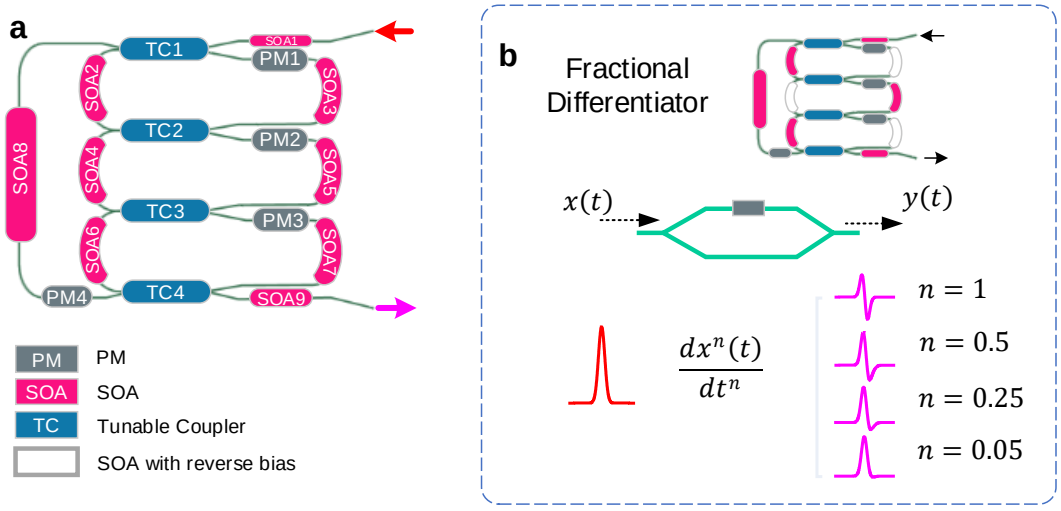

Fig. 5-4. The reconfigurable photonic integrated signal processor is configured as a fractional differentiator.

5.1.3. Photonic temporal Hilbert transformer

A *n*th order Hilbert transformer is an LTI system with a transfer function given (2-4). As can be seen an *n*th-order Hilbert transformer has a magnitude response of 1 and a phase jump of $n\pi$ at ω_0. A fractional Hilbert transformer becomes a conventional Hilbert transformer when $n = 1$. For $n = 0$, we have $H_0(\omega) = 1$, which is an all-pass filter. For $0 < n < 1$, the output is a weighted sum of the input signal and its conventionally Hilbert transformed signal [68]. In addition, a fractional Hilbert transformer with an order of n is equivalent to two cascaded fractional Hilbert transformers with fractional orders of α and β if $\alpha+\beta = n$. A ring resonator can be used to implement a Hilbert transformer if the Q-factor is high. For a ring resonator with a high Q-factor, the spectral response is close to all pass, except a narrow notch, which is small enough and would contribute negligible error to the transform [74]. Fig. 5-5 shows the configuration. Although the three ring resonators in the processor can be independently enabled or disabled, they are coupled in series. As a result, only one fractional Hilbert transformer or two cascaded fractional Hilbert transformers can be configured in the unit cell corresponding to a single-ring or two-cascaded-ring structure with all-pass configuration.

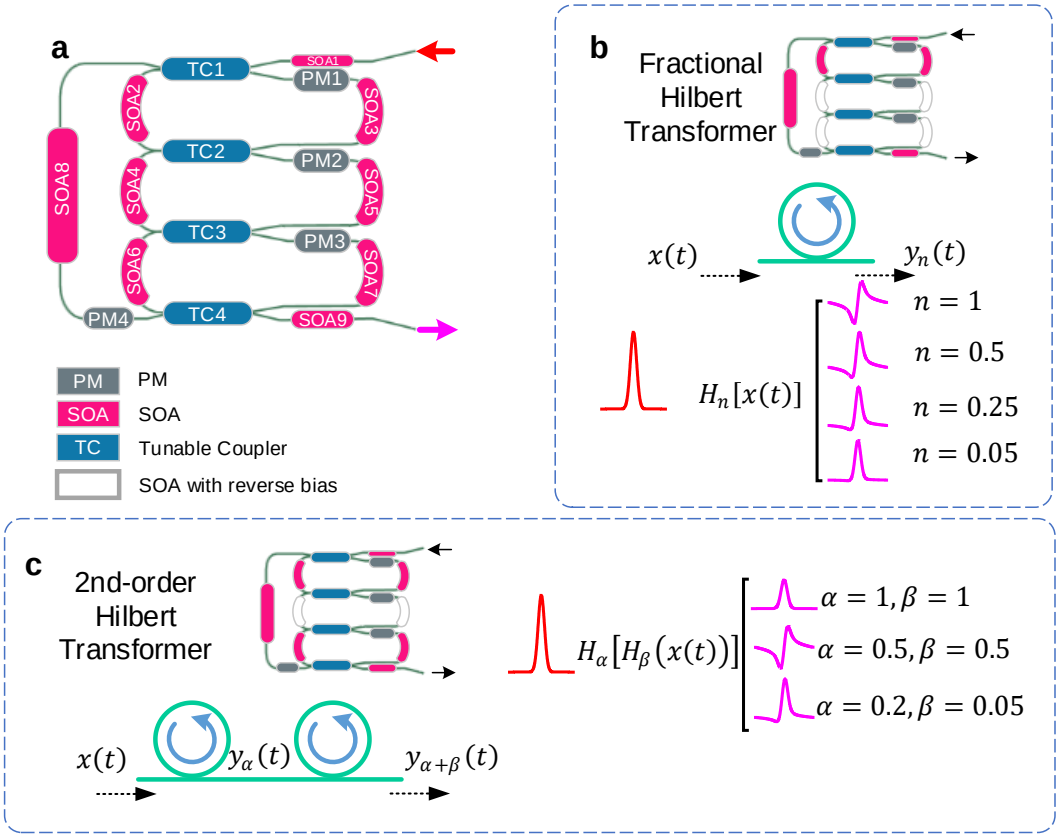

Fig. 5-5. The reconfigurable photonic integrated signal processor is configured as a single and two cascaded factional Hilbert transformers.

5.2 Reconfigurable Function Demonstration

The proposed signal processor is fabricated in an InP-InGaAsP material system, which is wire-bonded to a carrier for experimental demonstration, as shown in Fig. 5-2(b). The SOAs in each ring are measured to have a peak gain of 9.6 dB per SOA, which can be used to compensate for the insertion loss or to shut off the ring. The coupling coefficients of the TCs are measured at different injection currents to the PMs, which can be controlled from 0 to 100% when one of the PMs in each of the

TCs is injected with a current from 0 to 3.5 mA. There are twenty-one active components (SOAs and PMs) in a unit cell. When injection currents are applied, they will generate heat, which will shift the resonance wavelengths of the ring resonators and degrade the system stability. In the experiment, the chip is temperature controlled by a temperature control unit to ensure the working temperature is 22 ^{o}C, to maintain a stable operation.

5.2.1 Integrator

We first test the operation of the photonic temporal integrator with an order of n = 1. As a first-order integrator, the photonic integrated signal processor is configured to operate as a single ring resonator (R1 is on, R2 and R3 are off), as shown in Fig. 5-3(b) and Fig. 5-6(a), where the output optical signal is converted to an electrical signal at a photodetector and monitored by an oscilloscope. The free spectral range (FSR) is measured by an optical vector analyzer (OVA, Luna) to be 0.22 nm, as shown in Fig. 5-6(b). By changing the injection current to the PM in the ring (the PM in R1), the spectral response of the ring is laterally shifted, thus the peak location is also shifted, as shown in Fig. 5-6(c), which confirms the tuning of the working wavelength. In the experiment, an optical Gaussian pulse generated by a mode-locked laser (MLL) source and spectrally shaped by an optical bandpass filter (Finisar, WaveShaper 4000S) with a full width at half maximum (FWHM) of 54 ps

centered at 1557.4 nm, as shown as the red curve in Fig. 5-6(b) and the inset in Fig. 5-7(a), is then coupled into the temporal integrator via a lensed fiber. Fig. 5-7(a) shows the first-order temporal integral of the input Gaussian pulse. The integration time is measured to be 10.9 ns, which is more than one order of magnitude longer than the result reported in [34]. With a rising time of 48 ps, the proposed photonic integrator offers a time-bandwidth product [34] (TBWP, a principal figure of merit, represents the throughput limit for an optical system determined by the product of the bandwidth and the time-bandwidth of the optical system) of 227, which is much higher than an advanced electronic integrator (TBWP<10) [75], and also more than two-times greater than the previously reported photonic integrator (TBWP~100) [34]. The *Q*-factor is also calculated based on the integration time, which is ~50 million.

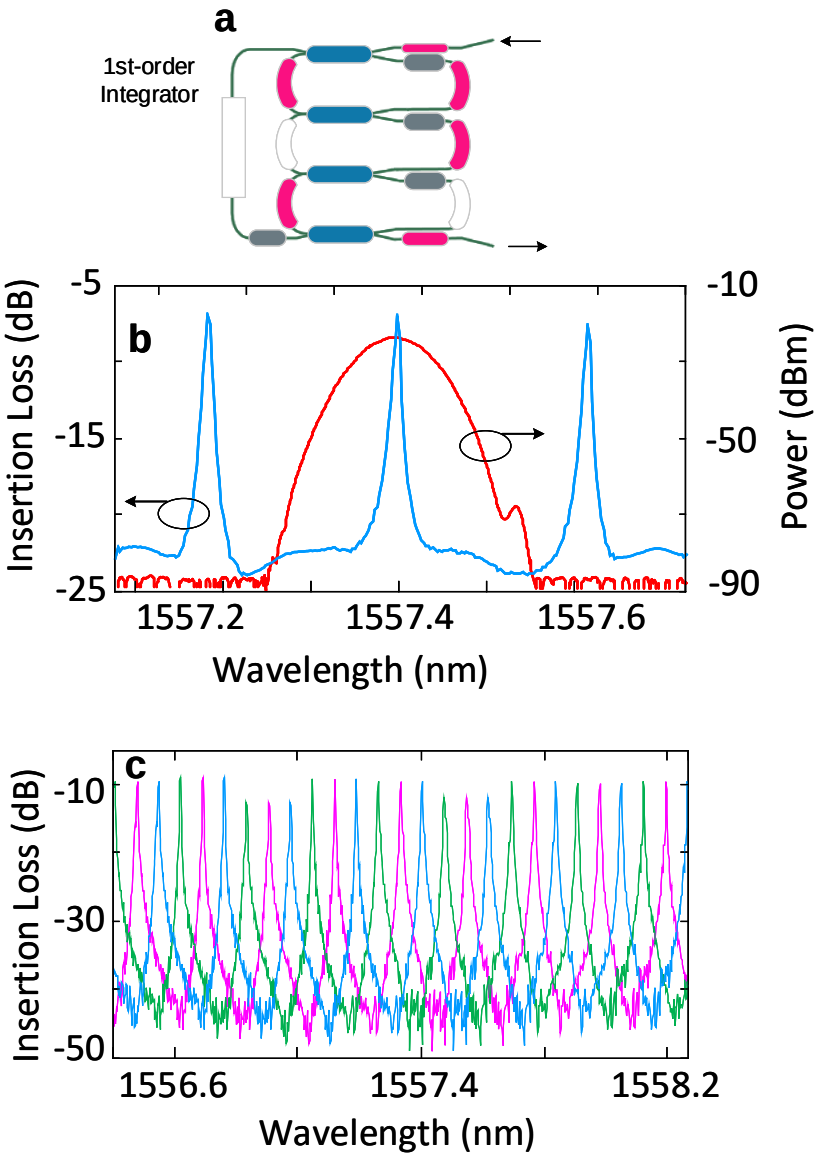

Fig. 5-6. Experimental results when the photonic integrated signal processor is configured as a temporal integrator. (a) The configuration of the first-order integrator. (b) The spectral response without injection current to the PM in the working ring resonator. (c) The spectral response of the integrator when the injection current to the PM in the ring is tuned at 0, 2 mA and 4 mA (green, magenta, blue).

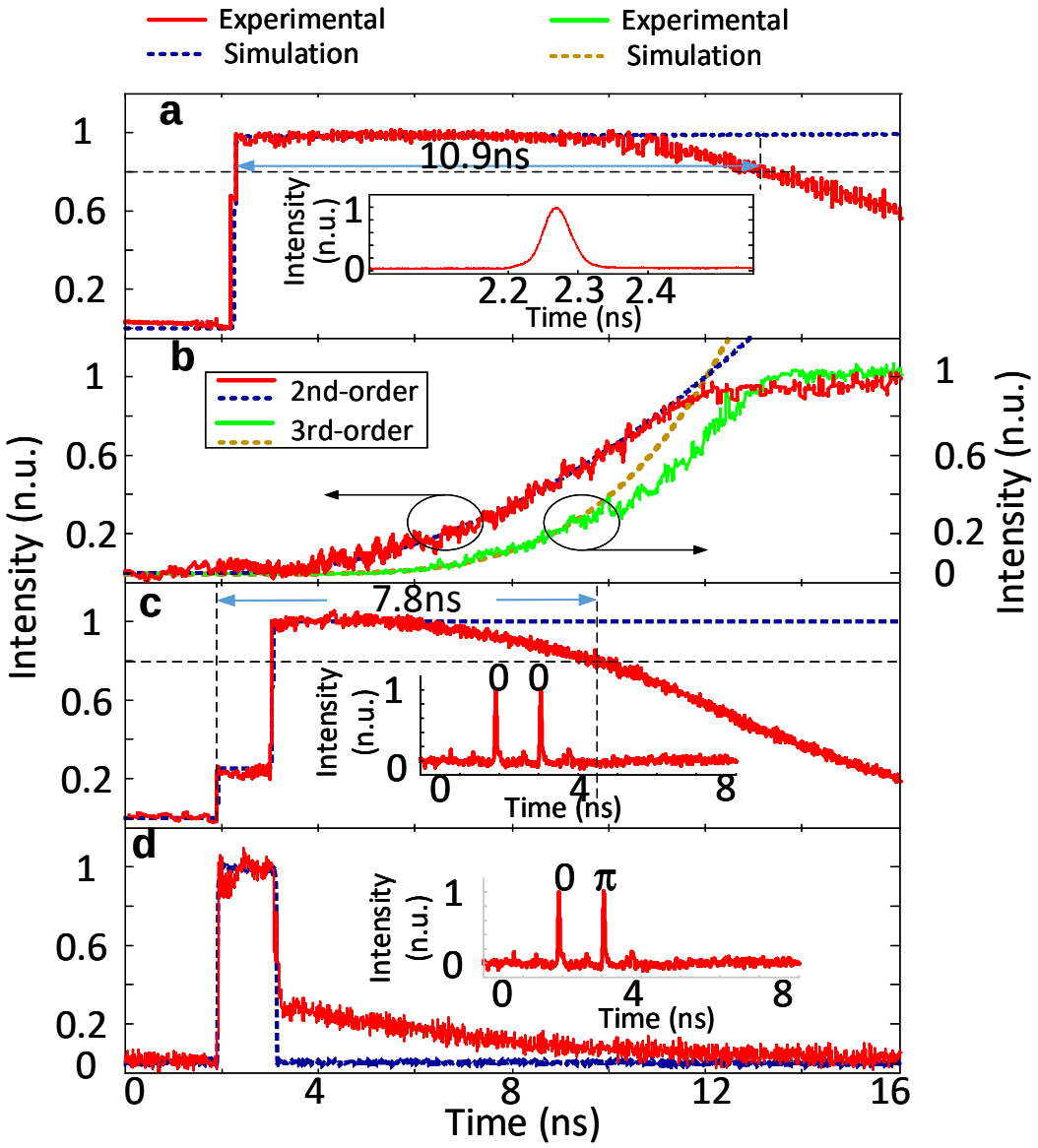

Fig. 5-7. Experimental results when the photonic integrated signal processor is configured as a temporal integrator. (a) The first-order integration of the Gaussian pulse with an integration time of 10.9 ns. The input Gaussian pulse with a temporal width of 54 ps is shown in the inset. (b) The second-order and third-order integration of the Gaussian pulse. (c) The first-order integration of an in-phase doublet pulse, which is shown in the inset. (d) The first-order integration of an out-of-phase doublet pulse.

Then, the photonic integrated signal processor is configured as a second-order (where R1 and R2 are on and R3 is off), and a third-order (where R1, R2 and R3 are all on) temporal integrator with two and three coupled ring resonators on the chip. The integration of the input Gaussian pulse at the outputs of the second- and third-order temporal integrator is then obtained, which are shown in Fig. 5-7(b). A higher order integrator, such as a second- and third-order integrator, can be used, for example, to solve higher order ordinary differential equations [34] [35]. A second-order integrator can also be used for arbitrary waveform generation [26]. The first-order integral of an in-phase and out-of-phase doublet pulse is also computed by the proposed first-order temporal integrator. An in-phase/out-of-phase doublet consists of two temporally separated in-phase/out-of-phase Gaussian waveforms with identical amplitude profile. As shown in Fig. 5-7(c) and (d), the temporal integrator sums up the area under the two field amplitude waveforms for the case of in-phase doublet pulse. Since the phase relationship between the two pulses of the in-phase doublet is not maintained during multiple round-trips in the ring resonator due to the dynamic intensity-dependent refractive index variations, the magnitude of the integration output is not well maintained, which leads to a reduced integration time of 7.8 ns. For the case of out-of-phase doublet pulse, the time integral of the second waveform in the doublet pulse cancels that of the first waveform, leading to a square-like profile with the duration determined by the time

delay between the two waveforms of the doublet pulse. As shown in Fig. 5-7(d), the two out-of-phase pulses do not subtract completely, this is because the two pulses are not perfectly identical in amplitude and phase due to a slight asymmetry of the MZI used to generate the two pulses (the two pulses are generated by splitting a single pulse to two pulses and recombining the time-delayed pulses at the output of the MZI). These results suggest important applications of a photonic integrator as a memory unit, such as "write" and "erase" operations [34]. Simulations are also performed to calculate the temporal integral of the input pulse and the results are plotted with dashed line as shown in Fig. 5-7(a)-(d). As can be seen, the experimental results agree well with the simulation results. The active components such as the SOAs and PMs in the processor offer a precise control of the resonance peak and the *Q*-factor of each ring resonator, which is indispensable for achieving higher order integration [19]. This is the first time that a higher order (up to 3) photonic temporal integrator is implemented on an integrated chip.

5.2.2 Differentiator

The photonic integrated signal processor is then configured to have an MZI structure to implement a fractional order temporal differentiator (where R1, R2 and R3 are all off, forming one arm of the MZI, the bypass waveguide forms another arm of the MZI), as shown in Fig. 5-8(a).

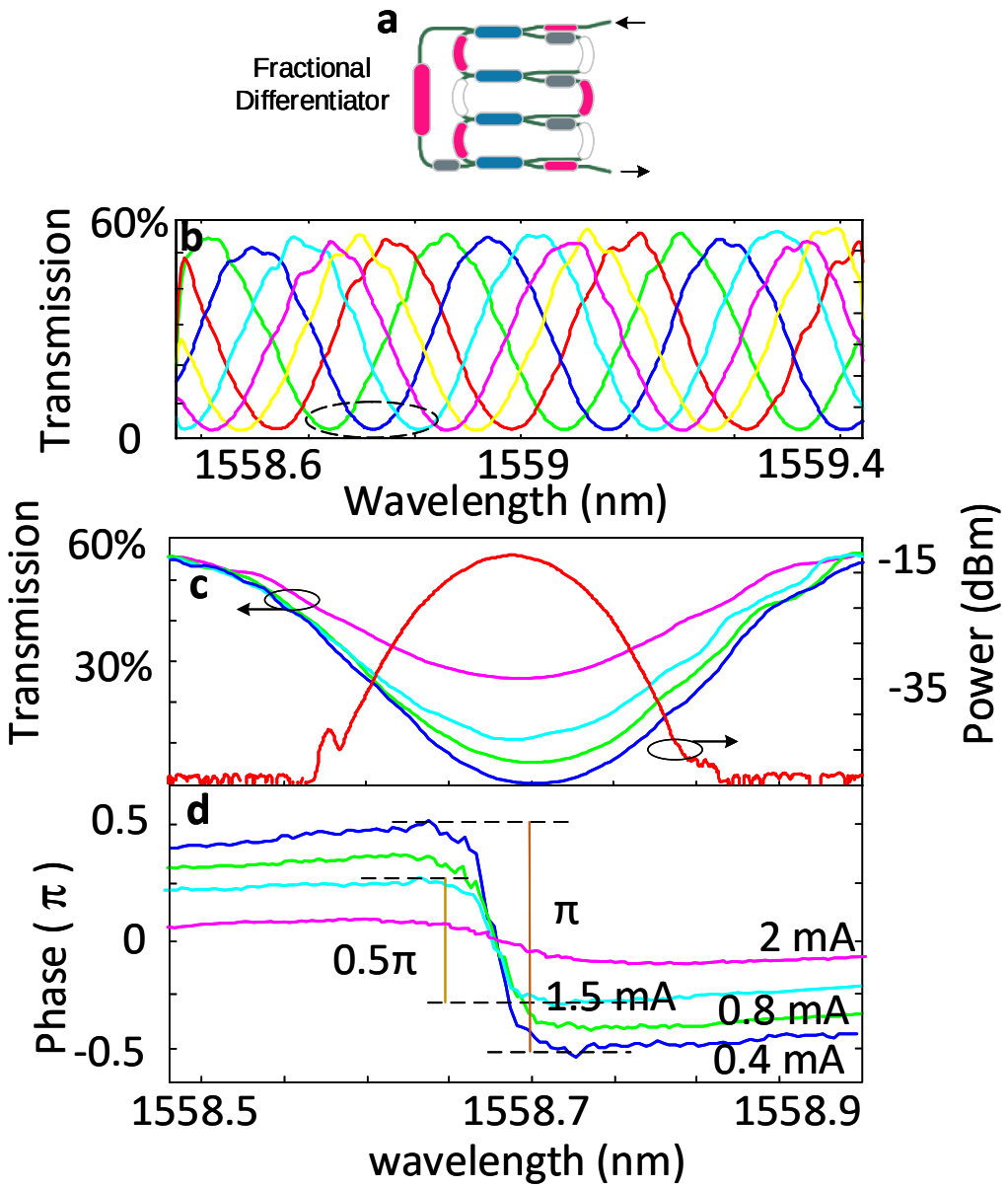

Fig. 5-8. Experimental results when the photonic integrated signal processor is configured as a fractional differentiator. (a) The configuration. (b) The spectral response with six different injection currents to the PM in the input tunable coupler of the MZI. (Blue, cyan, magenta, red, and green: 0, 1.2 mA, 2.3 mA, 3.7 mA, and 4.6 mA) (c) The spectral response and (d) phase response of the differentiator when the injection current to the PM in the MZI is tuned at four different values.

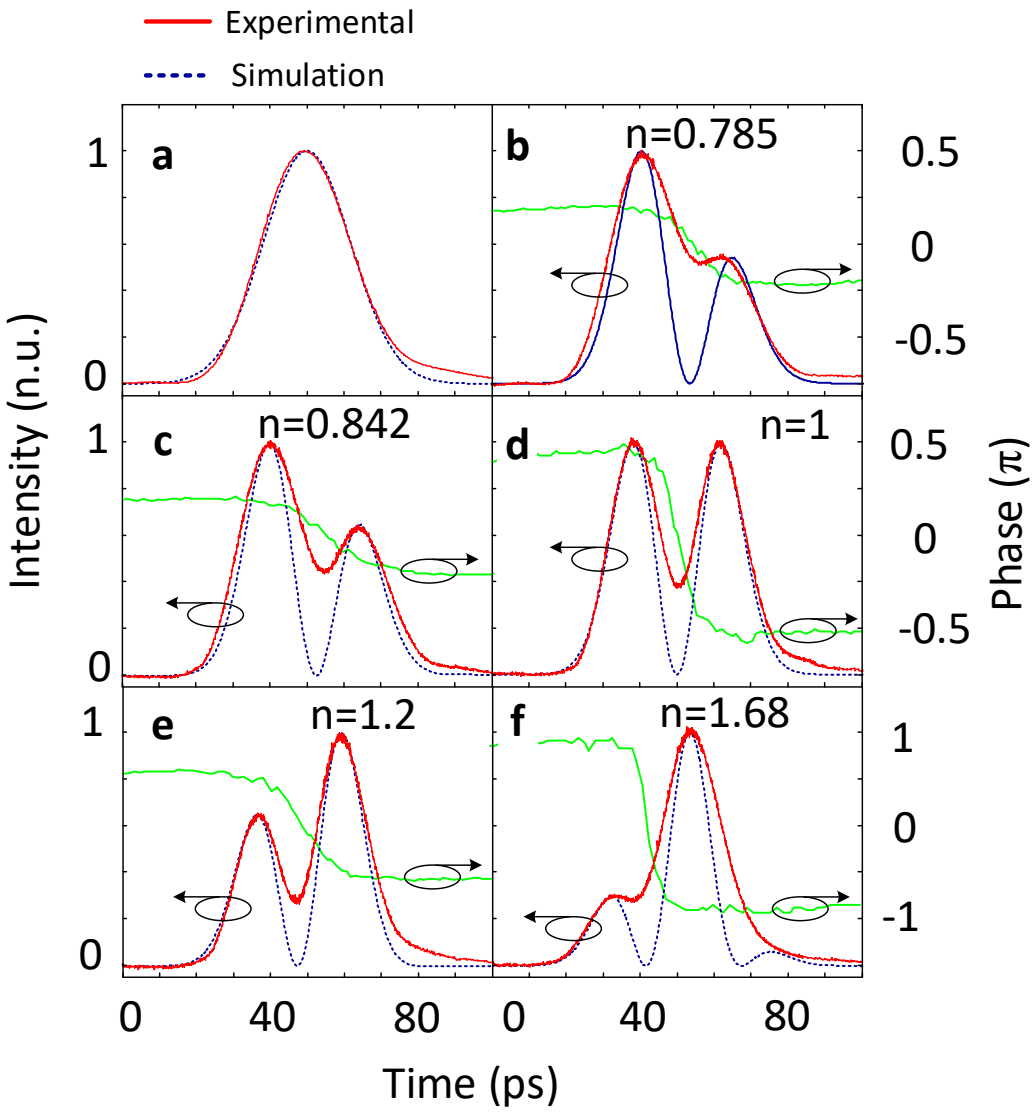

Fig. 5-9. Experimental results when the photonic integrated signal processor is configured as a fractional differentiator. (a) The input Gaussian pulse with a temporal width of 33 ps. (b) to (f) The fractional differentiation of the input Gaussian pulse with a fraction order of (b) 0.785, (c) 0.842, (d) 1, (e)1.2, and (f) 1.68.

Again, a photodetector is connected at the output of the chip to convert the optical signal to an electrical signal. The spectral response of the MZI is shown in Fig. 5-8(b). It has an FSR of 0.44 nm. By changing the injection current to the PM in one of the two arms, the spectral response is then laterally shifted, as shown in Fig. 5-8(b). The relationship between the phase shift in the PM and injection current is quite linear with a 6 mA injection current to provide a 2π phase change. By changing the injection current to the PMs in the tunable couplers at the input or output of the MZI, the coupling coefficient can be tuned to achieve tunable phase shift at the transmission notch. Fig. 5-8(c) and (d) shows the measured transmission notch with a phase jump from 0 to π by an optical vector network analyzer (OVA, Luna). A Gaussian pulse with a temporal width of 33 ps centered at 1558.7 nm, shown in Fig. 5-8(c) and Fig. 5-9(a), is coupled into the chip. By changing the injection current applied to the PM in the tunable coupler, the fractional order can be tuned. Five differentiated pulses corresponding to five differentiation orders of 0.785, 0.842, 1, 1.2, and 1.68 are obtained, which are shown in Fig. 5-9(b) to (f), respectively. The phase information of the differentiated pulses is also shown. Again, simulations are also performed to calculate the temporal differentiation of the input Gaussian pulse with five differentiation orders of 0.785, 0.842, 1, 1.2, and 1.68. The results are also shown in Fig. 5-9(b)-(f). As can be seen, the experimental results agree well with the simulation results. The slightly mismatch in the dip between the simulation and experimental output waveforms is due to the limited

bandwidth of the photodetector. The proposed differentiator can provide an analog processing bandwidth of 55 GHz, as can be seen from Fig. 5-8(c), which is significant larger than an electronic microwave differentiator [76]. With such a large bandwidth, the photonic differentiator can provide fast signal processing and signal coding [41]). In addition, the differentiation order is also tunable, which provides better flexibility in signal processing, such as tunable image enhancement [67].

5.2.3 Hilbert transformer

The photonic integrated signal processor can also be configured to have a single ring or two cascaded ring structure to implement a fractional Hilbert transformer or two cascaded fractional Hilbert transformers. Fig. 5-10(a) shows the configuration as a single-ring fractional Hilbert transformer (R1 is on, R2 and R2 are off). The spectral response of the single-ring fractional Hilbert transformer is measured and shown in Fig. 5-10(b) with an FSR of 0.22 nm. By changing the injection current to the PM in the ring, the notch location is tuned and the FSR is slightly changed as shown in Fig. 5-10(b). The phase response which determines the fractional order of the Hilbert transform can also be tuned by changing the coupling coefficient between the ring and the bypass waveguide, as shown in Fig. 5-10(c) and (d), which is achieved by changing the injection current to the PMs in the TCs.

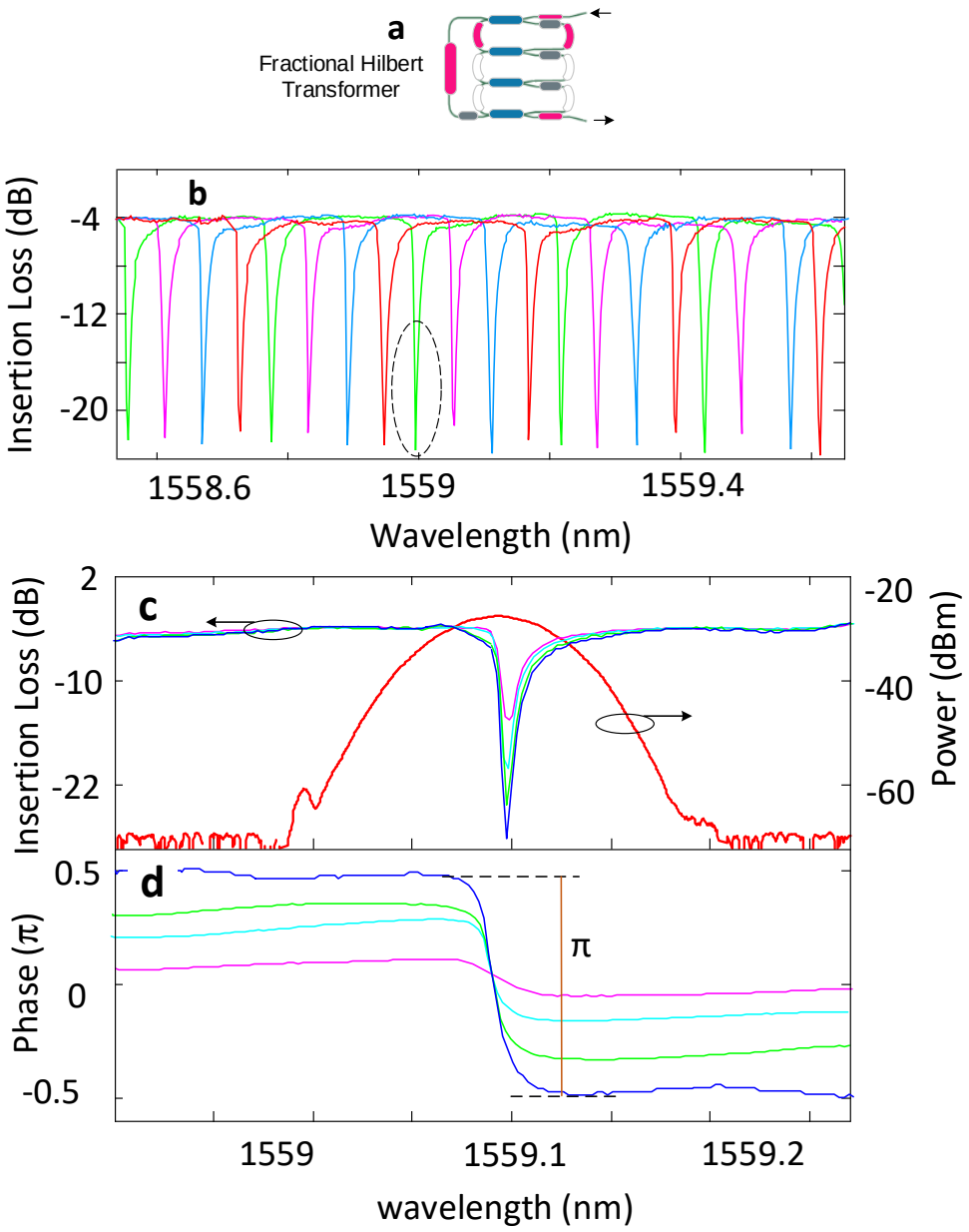

Fig. 5-10. Experimental results when the photonic integrated signal processor is configured as a Hilbert transformer. (a) The configuration. (b) The spectral response with four different injection currents to the PM in working ring resonator. (c) The spectral response and (d) phase response of the differentiator when the injection current to the PM in the working ring is tuned at four different values.

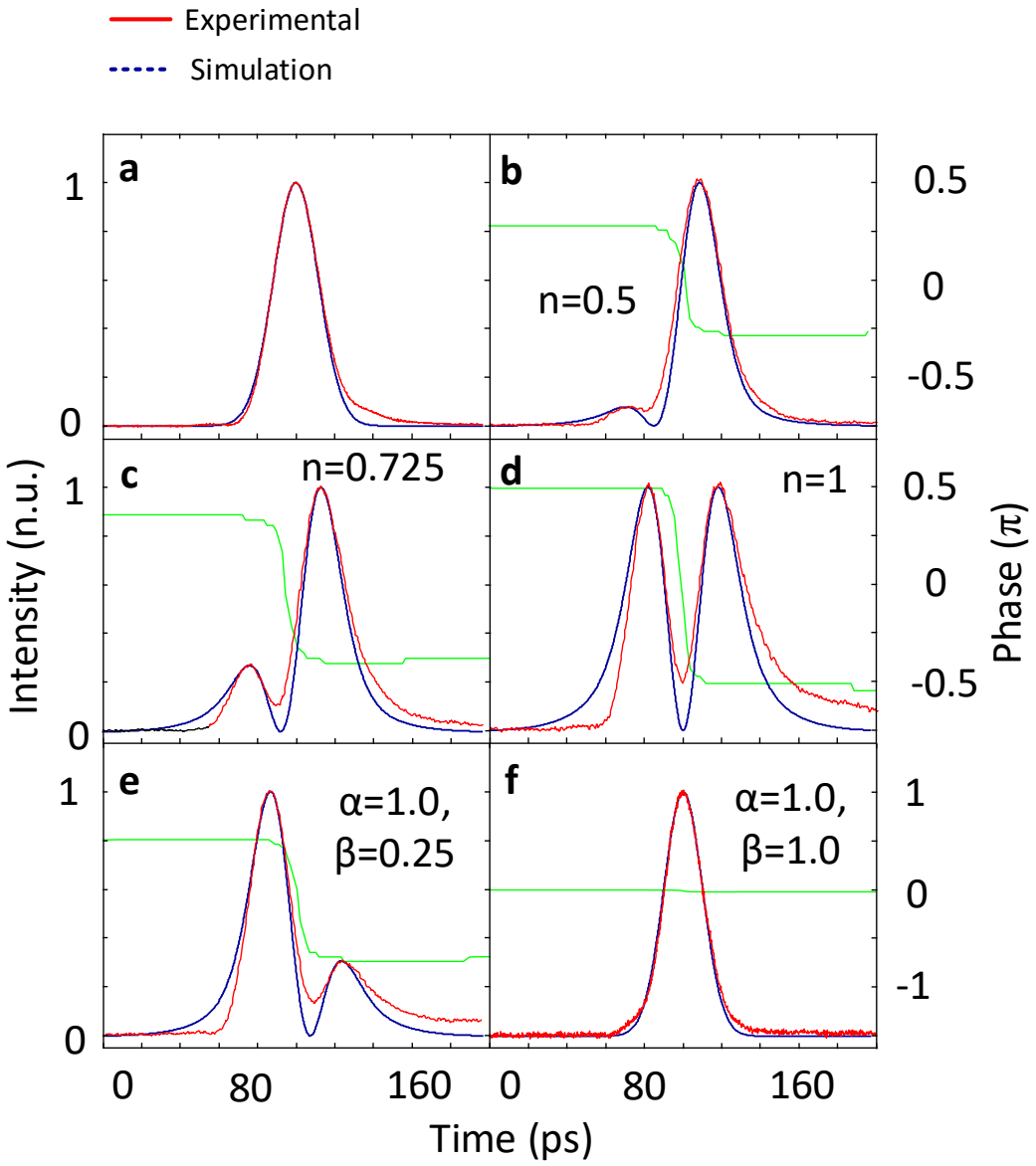

Fig. 5-11. Experimental results when the photonic integrated signal processor is configured as a Hilbert transformer. (a) The input Gaussian pulse with a temporal width of 33 ps. (b) to (f) The fractional Hilbert transform of the input Gaussian pulse with a fraction order of (b) 0.5, (c) 0.725, and (d) 1. (e) and (f) shows the results of the cascaded Hilbert transformers with fraction orders of (1.0, 0.25) and (1.0, 1.0).

To validate the operation of the processor as a fractional Hilbert transformer, an optical Gaussian pulse with a central wavelength at 1559.1 nm and a temporal width of 33 ps, shown in Fig. 5-11(a), is coupled into the chip. The fractional order of the Hilbert transformer is continuously tunable from 0 to 1 by changing the coupling coefficient through controlling the injection currents to the PMs in the TC. Fig. 5-11(b), (c), and (d) shows the fractionally Hilbert transformed pulses with a tunable fractional order from 0.5 to 1. The fractional order Hilbert transformer can be used to construct a secure communication system [68], in which the fractional order *n* is used as a secret key for demodulation. If the order *n* is unknown in the demodulation, the signal cannot be recovered. The proposed fractional order Hilbert transformer can also provide fast tunability of the fractional order, which can be used in secure communications with dynamic secrets.

The signal processor can also be configured as two cascaded Hilbert transformers (R1 and R3 are on, and R2 is off). Fig. 5-11(e) and (f) shows the output pulses with the fractional orders of (1.0, 0.25) and (1.0, 1.0) which are equivalent to a single Hilbert transformer with a fractional order of 1.25 and 2. Again, the tuning is achieved by changing the coupling coefficients through controlling the injection currents to the PMs in the tunable couplers. Comparing to the most recently reported tunable fractional Hilbert transformer in a chip-scale device [21], the

proposed Hilbert transformer offers a much easier control of the tunable fractional order through tuning the injection current instead of changing the polarization states of the input signal.

The proposed photonic signal processor can be reconfigured as a photonic temporal integrator, differentiator, and Hilbert transformer, which are basic building blocks for general-purpose signal processing. The proposed photonic signal processor can be used to provide high-speed processing to break the speed and bandwidth bottleneck of an electronic processor. For example, a photonic temporal integrator is one of the most important components in a delta-sigma converter for optical analog to digital conversion [29]. A photonic temporal differentiator can be used in demultiplexing an OTDM signal [43] and performing real-time amplitude and phase measurement of an optical signal. A Hilbert transformer can be used to generate a wideband SSB modulated signal, which is useful in a RoF link to avoid dispersion-induced power penalty [40]. If the designed photonic signal processor is employed in an optical network, the above-mentioned functionalities can be achieved with a single integrated photonic chip. More importantly, with the development of all-optical networks, photonic signal processors can be incorporated into an optical network to perform fast signal processing without digital sampling, and OE and EO conversions. Thus, the proposed photonic signal

processor can provide a potential cost-effective solution for signal processing in future all-optical networks.

5.3 Error Performance Evaluation

In real applications, the proposed high speed processor should be able to provide accurate signal processing with small errors. To evaluate the error performance, an error analysis is performed using the measured transfer functions of the photonic signal processor that is reconfigured as an integrator, a differentiator, and a Hilbert transformer. We assume that the input pulse is an ideal Gaussian pulse and the mean absolute errors are calculated as the averaged difference between the intensities of the simulated output waveform based on the measured transfer functions and the numerically calculated waveform. Since an ideal integrator has a temporal output extending to infinity if the input is a Gaussian pulse, and our proposed integrator can provide a finite integration time of 10.9 ns, the errors in the analysis are measured in a time duration of 20 ns. The mean absolute errors of the processor to perform each of the functions can be found in Fig. 5-12. As can be seen, the integrator, differentiator, and Hilbert transformer can operate with a minimum error for an input Gaussian pulse with a bandwidth of 19.11, 19.72, and 30.84 GHz, respectively.

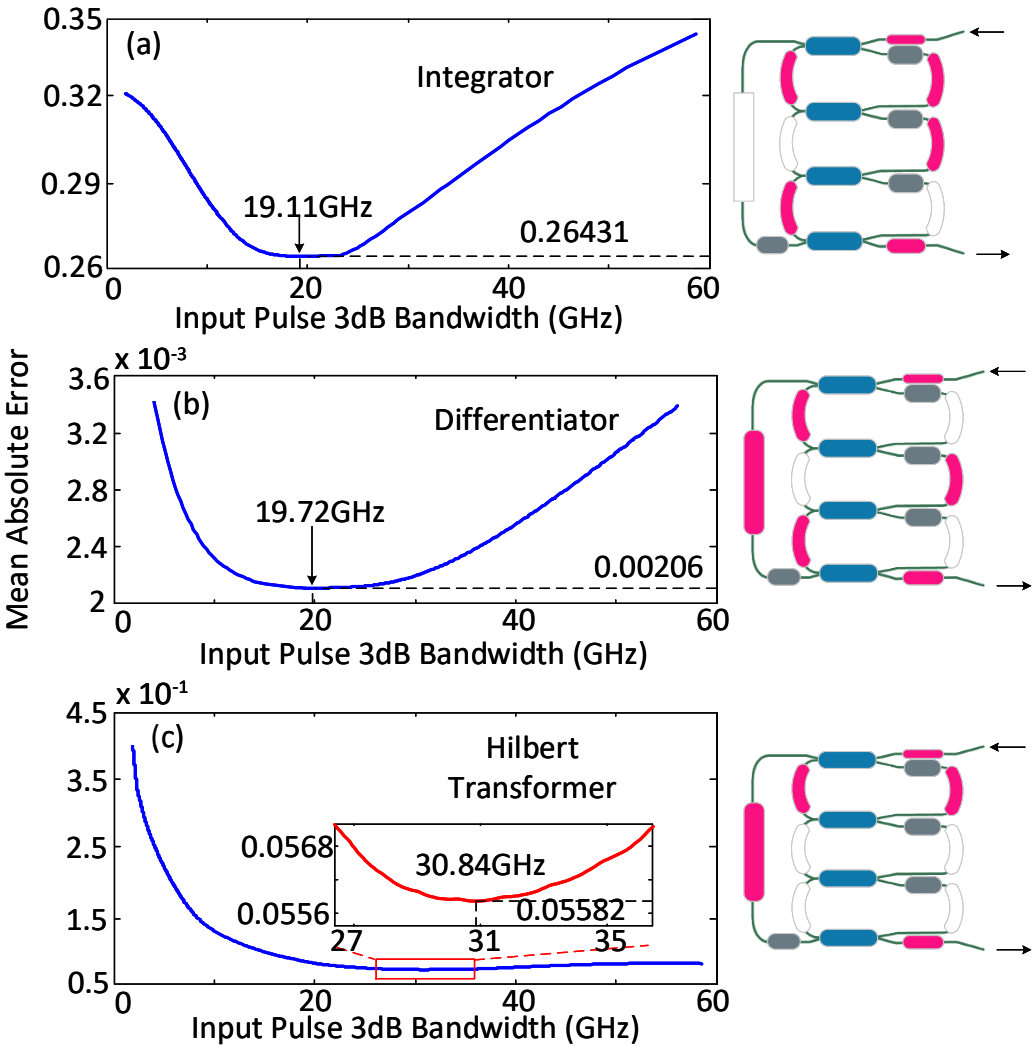

Fig. 5-12. Estimated processing error as a function of the input pulse bandwidth for a (a) temporal integrator, (b) temporal differentiator, and (c) Hilbert transformer.

The proposed photonic signal processor can work for a pulse with a different bandwidth, at the cost of increased mean absolute errors. The processing of a rectangular pulse sequence as an input signal is also evaluated. For example, for a rectangular pulse sequence the Hilbert transformer has an optimal processing bandwidth of 30.84 GHz. A binary rectangular pulse sequence with a duty cycle of

50% and a period of 57 ps can be processed with a minimum error, which corresponds to a data rate of 17.5 Gbps. If a multilevel signal is used, the data rate can be higher.

5.4 Power Budget

By adjusting the injection currents to the SOAs and PMs, the photonic signal processor can be reconfigured to operate as an integrator, differentiator, and Hilbert transformer. The injection currents and the power consumptions are summarized in Table V-I, Table V-II, and Table V-III.

In the experiment, the power of the input optical pulses is controlled below -10 dBm, and the SOAs inside the ring resonators are working with small injection currents to provide small gain to compensate for the insertion losses, thus the nonlinear effects in the rings are small and negligible. However, nonlinear effects such as self-phase modulation and four-wave mixing have to be considered if the power of the input signal is high. To utilize the proposed processing unit cell in a large system, the power consumptions of the PMs and SOAs, and the ASE noise from the SOAs should be also considered. In the experiment, for example, the total power consumption of the first-order integrator is 350 mW including 148 mW consumed by the input/output SOAs, which can be significantly reduced in a large

system where all units are fabricated on a single chip without fiber coupling loss between the units. In addition, the SOAs have a length of 400 μm, therefore, the SOAs in the ring resonators only operate at a low current density. This low-current-density operation increases the ASE noise. A potential solution to reduce the ASE noise and further increase the integration time is to use SOAs with shorter lengths, thus the SOAs can operate at a much higher operation current density. Operating at a high current density, a single SOA is sufficient to compensate for the insertion loss inside each ring resonator, therefore, the number of SOAs can also be reduced for large scale integration, and the power consumption is reduced. As can be seen from Fig. 5-6(b), Fig. 5-8(b), and Fig. 5-10(b) in Chapter 5.2, the bandwidth of the proposed photonic signal processor when reconfigured as an integrator and a Hilbert transformer is 27 GHz or 0.22 nm at 1550 nm, limited by the FSR of the ring resonators. When reconfigured as a differentiator, the bandwidth is 55 GHz or 0.44 nm at 1550 nm, limited by the FSR of the MZI. A shortened length of the ring resonators will lead to a greater FSR and further increase the bandwidth of the signal processor.

Since the reconfigurability and tunability of the proposed photonic signal processor are achieved by tuning the injection currents to the active components (nine SOAs and twelve PMs) on the chip, the processor needs twenty-one current injection sources to realize full system reconfigurability and wavelength tunability. In the

experiment, the SOAs and PMs on the chip are controlled by adjusting the injection currents from multiple source measurement units (SMUs). Those SMUs, for practical applications, can be replaced by a customized electronic unit with programmable current control, such as a field-programmable gate array (FPGA). By programming the FPGA, the signal processor can be reconfigured for different signal processing functions. In the proposed photonic signal processor, a stable resonance wavelength and a high *Q*-factor are critical for achieving a long integration time. However, the ambient temperature change can shift the resonance wavelength of the ring resonators and change the gain profiles of the SOAs, which will alter the working wavelengths and decrease the *Q*-factors of the ring resonators. To maintain a stable temperature in the signal processor for good stability, a thermoelectric cooler (TEC) is added in the electronic unit to improve the stability, and thus to increase the integration time.

Table V-I. The injection currents when the processor is configured as an integrator.

Components	**1**st-order	**2**nd-order	**3**rd-order
SOA1	28.806 mA	28.806 mA	28.806 mA
SOA2	20.504 mA	20.504 mA	20.504 mA
SOA3	19.325 mA	19.325 mA	19.325 mA
SOA4	-1.005 μA	21.412 mA	21.412 mA
SOA5	24.000 mA	19.822 mA	19.822 mA
SOA6	24.532 mA	24.532 mA	21.001 mA
SOA7	-1.130 μA	-1.130 μA	22.851 mA
SOA8	-10.213 μA	-10.213 μA	-10.213 μA
SOA9	29.006 mA	29.006 mA	29.006 mA
PM1	0	0	0
PM2	0	1.290 mA	1.290 mA
PM3	0	0	0.752 mA
PM4	0	0	0
TC1	1.950 mA	1.950 mA	1.950 mA
TC2	1.942 mA	1.942 mA	1.942 mA
TC3	0	1.833 mA	1.833 mA
TC4	0	0	1.906 mA
Power	350.475 mW	381.851 mW	419.695 mW

Table V-II. The injection currents when the processor is configured as a fractional differentiator.

	n=0.785	n=0.842	n=1.000	n=1.200	n=1.680
SOA1	28.806 mA	28.806 mA	28.806 mA	28.806 mA	28.806 mA
SOA2	25.131 mA	25.131 mA	25.131 mA	25.131 mA	25.131 mA
SOA3	-1.005 µA	-1.005 µA	-1.005 µA	-1.005 µA	-1.005 µA
SOA4	-1.133 µA	-1.133 µA	-1.133 µA	-1.133 µA	-1.133 µA
SOA5	24.000 mA	24.000 mA	24.000 mA	24.000 mA	24.000 mA
SOA6	24.532 mA	24.532 mA	24.532 mA	24.532 mA	24.532 mA
SOA7	-1.142 µA	-1.142 µA	-1.142 µA	-1.142 µA	-1.142 µA
SOA8	33.617 mA	33.617 mA	33.617 mA	33.617 mA	33.617 mA
SOA9	29.006 mA	29.006 mA	29.006 mA	29.006 mA	29.006 mA
PM1 PM2 PM3 PM4	0	0	0	0	0
TC1	1.051 mA	1.051 mA	1.051 mA	1.051 mA	1.051 mA
TC2 TC3	0	0	0	0	0
TC4	0.276 mA	0.535 mA	1.028 mA	1.505 mA	1.811 mA
Power	419.296 mW	419.650 mW	420.201 mW	421.604 mW	422.126 mW

Table V-III. The injection currents when the processor is configured as a fractional Hilbert transformer.

	n=0.500	n=0.725	n=1.000	α=1.000, β=0.250	α=1.000, β=1.000
SOA1	28.806 mA	28.806 mA	28.806 mA	28.806 mA	28.806 mA
SOA2	20.504 mA	20.504 mA	20.504 mA	20.504 mA	20.504 mA
SOA3	19.519 mA	19.519 mA	19.519 mA	19.519 mA	19.519 mA
SOA4	-0.002 μA	-0.006 μA	-0.007 μA	-0.007 μA	-0.007 μA
SOA5	-0.004 μA	-0.018 μA	-0.113 μA	-0.113 μA	-0.113 μA
SOA6	-0.006 μA	-0.006 μA	-0.008 μA	21.001 mA	21.001 mA
SOA7	-0.015 μA	-0.023 μA	-0.051 μA	22.851 mA	22.851 mA
SOA8	33.617 mA	33.617 mA	33.617 mA	33.617 mA	33.617 mA
SOA9	29.006 mA	29.006 mA	29.006 mA	29.006 mA	29.006 mA
PM1	0	0	0	0	0
PM2	0	0	0	0	0
PM3	0	0	0	0.752 mA	0.752 mA
PM4	0	0	0	0	0
TC1	0.539 mA	0.871 mA	1.051 mA	1.051 mA	1.051 mA
TC2	2.390 mA	2.390 mA	2.390 mA	2.390 mA	2.390 mA
TC3	0	0	0	2.173 mA	2.173 mA
TC4	2.337 mA	2.337 mA	2.337 mA	0.273 mA	2.437 mA
Power	324.935 mW	325.385 mW	325.652 mW	418.919 mW	423.79 mW

5.5 Application Examples

5.5.1. Image processing

Image processing such as edge enhancement by differentiation can be implemented by the proposed photonic signal processor. For example, an image can be encoded in a temporally stretched optical pulse based on wavelength to space mapping [77], which can then be processed by the proposed photonic signal processor. To demonstrate the image enhancement concept, here we use five temporal waveforms to emulate five analog image signals, as shown in Fig. 5-13(a), (b), (c), (d) and (e). The differentiations of the five waveforms by the proposed photonic signal processor are shown in Fig. 5-13(f), (g), (h), (i) and (j). As can be seen, the transitions (corresponding to the edges in an image) in a square, a sawtooth, a triangular, a trapezoidal, and a stepped waveform are enhanced. The experimental results are also consistent with the simulation results as shown in Fig. 5-13(k), (l), (m), (n), and (o).

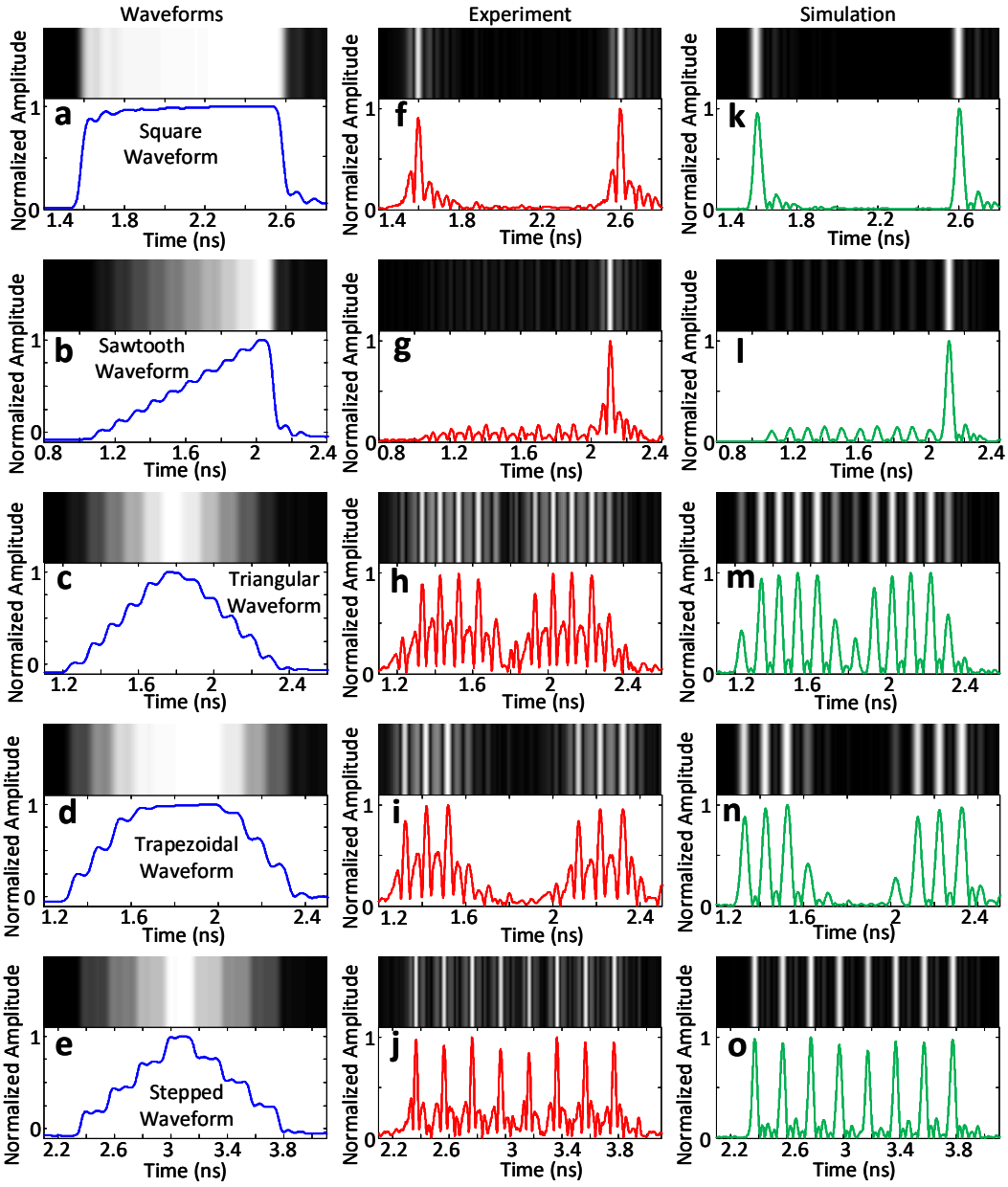

Fig. 5-13. Experimental results (red) to show the transition enhancement by the proposed photonic signal processor. Simulation results (green) are also shown for comparison. Transitions in a (a) square, (b) sawtooth, (c) triangular, (d) trapezoidal, and (e) stepped waveform, are enhanced by the proposed photonic signal processor as shown in (f), (g), (h), (i), and (j). The simulation results are shown in (k), (l), (m), (n), and (o) for comparison.

5.5.2. Hilbert transform for SSB modulation

To achieve SSB modulation, the proposed photonic signal processor is reconfigured as a Hilbert transformer, which is incorporated in an MZI, as shown in Fig. 5-14.

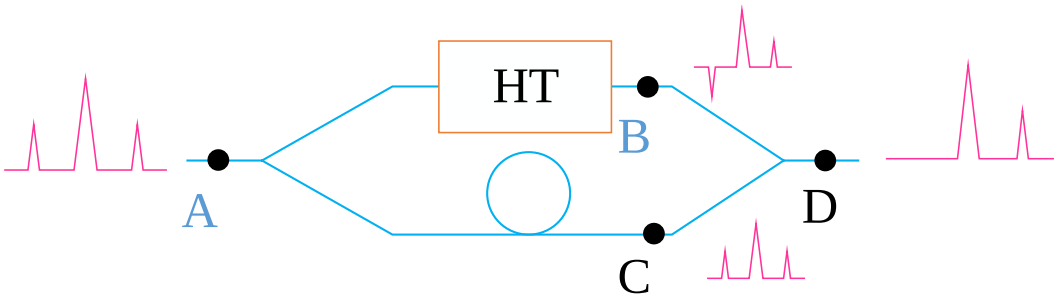

Fig. 5-14. Experimental setup for the demonstration of SSB modulation using the proposed signal processor reconfigured as a Hilbert transformer. HT: Hilbert transformer.

A double-sideband (DSB) modulated optical signal is sent into the MZI. A Hilbert transformer can provide a π phase shift to one sideband of the DSB modulated optical signal, thus the combination of two DSB modulated signals at the output of the MZI will cancel one sideband, and an SSB modulated optical signal is thus obtained. The spectrum of the generated SSB modulated optical signal is measured by an optical spectra analyzer (OSA), which is shown in Fig. 5-14.

As can be seen from Fig. 5-15, an optical SSB-modulated signal is generated. The sideband suppression ratio is 12.7 dB, 16.1 dB, and 13.8 dB when the frequency of the modulation signal is 10 GHz, 15 GHz, and 20 GHz, respectively.

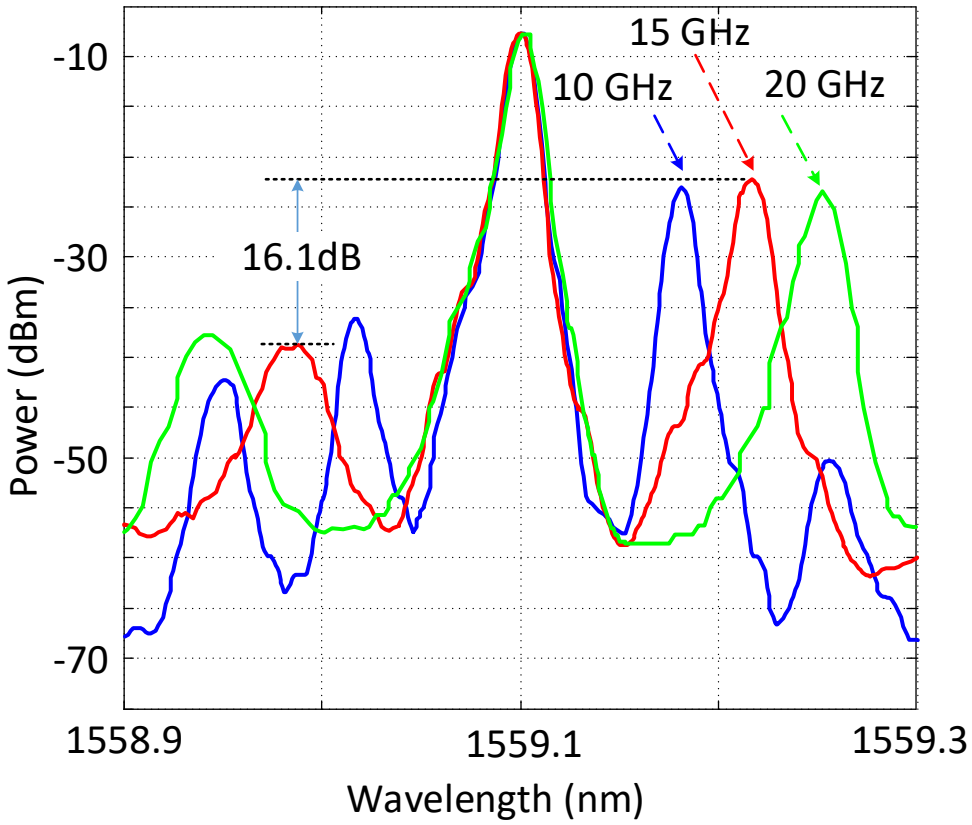

Fig. 5-15. The spectrum of the experimentally generated SSB modulated optical signal.

5.5.3. Optical filter with a flat top and a tunable passband and center frequency

The proposed photonic signal processor can also be reconfigured to operate as an optical filter with a flat top and a tunable passband and center frequency. The tunability is achieved by adjusting the currents applied to the active components including the SOAs and PMs in the processor. For example, to implement a tunable DWDM filter, the signal processor can be reconfigured to have a structure with three coupled rings, as shown in Fig. 3-1(c). A simulation based on the three-coupled-ring structure is implemented [78]. As shown in Fig. 5-16(a), the filter has a flat top which is achieved by tuning the gain/loss in each of the ring resonators, A1, A2, A3, A4, A5, and A6, and the width of a passband of the DWDM filter is continuously tunable from 5 to 10 GHz by adjusting the coupling coefficients C2 and C3, as indicated in Fig. 3-1(c). The center frequency of a bandpass is also continuously tunable by adjusting the phase changes in the ring resonators, which are ϕ_1, ϕ_2, and ϕ_3 as indicated in Fig. 3-1(c). For example, the center frequency of a bandpass can be shifted by ~10.5 GHz or ~21 GHz if $\phi_1=\phi_2=\phi_3=2\pi/3$ or $\phi_1=\phi_2=\phi_3=4\pi/3$, as shown in Fig. 5-16(b). Comparing with a thin film DWDM filter [79], the DWDM filter implemented by the proposed photonic signal processor offers both continuously tunable bandwidth and center frequency. Since the adjacent channel spacing of the implemented DWDM filter is determined by the

FSR of the ring resonators, the lengths of the ring resonators have to be selected to have an FSR corresponding to the wavelength spacing specified by the ITU grid.

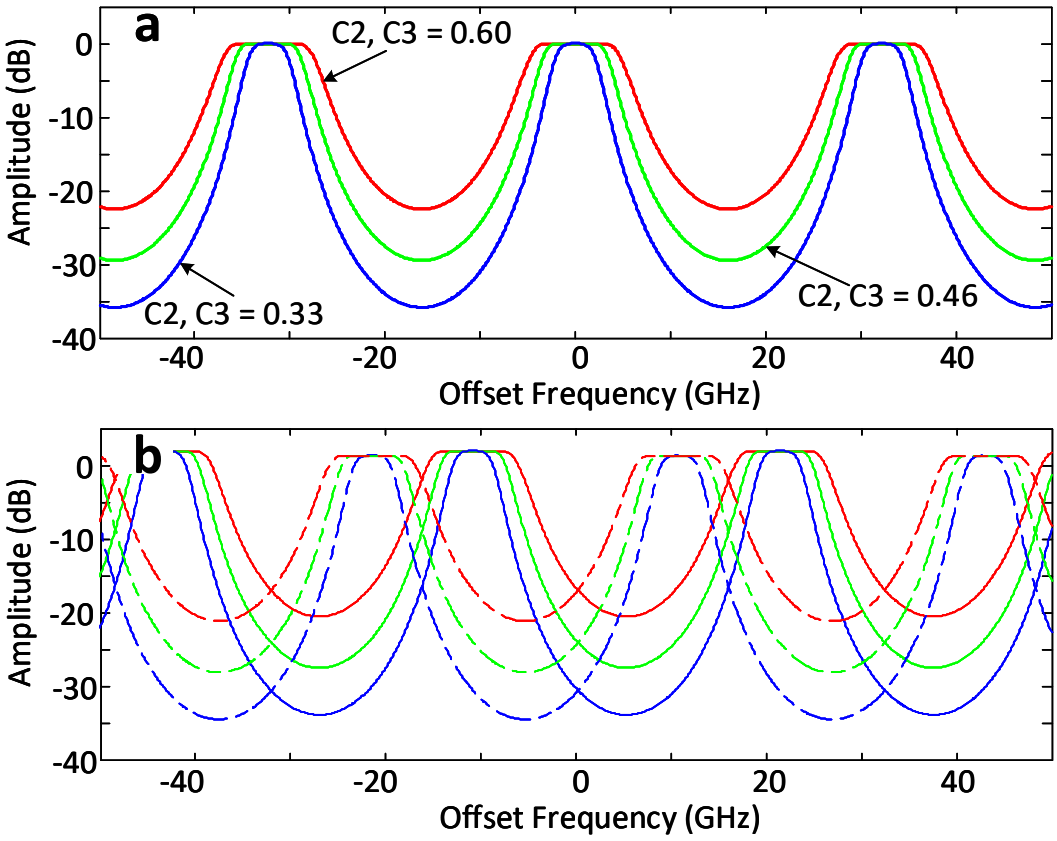

Fig. 5-16. Three coupled rings for implementing a tunable DWDM filter and the simulation results. (a) The structure. (b) Continuously tunable 3-dB bandwidth from 5 to 10 GHz for a passband with a minimum extinction ratio of 22 dB by adjusting the coupling coefficients C2 and C3. (c) Continuously tunable center frequency of a bandpass by adjusting the phase terms (dashed line, $\phi_1 = \phi_2 = \phi_3 = 2\pi/3$; solid line, $\phi_1 = \phi_2 = \phi_3 = 4\pi/3$) via the controlling the injection currents to the PMs in the ring resonators.

5.6 Summary

In summary, a fully reconfigurable photonic integrated signal processor based on a photonic integrated circuit was designed, fabricated and demonstrated in this chapter. The operation of the signal processor reconfigured as a temporal integrator, a temporal differentiator and a Hilbert transformer with a tunable order and a tunable operation wavelength was demonstrated experimentally. In particular, a temporal integrator over a bandwidth of 0.22 nm with an integration time of 10.9 ns was achieved, which is the longest integration time ever reported. Although some photonic signal processing functions, such as arbitrary waveform generation and optical dispersion compensation, are not implemented with the current design, this work represents an important step towards the realization of a fully programmable high speed and wideband general-purpose photonic signal processors that can overcome the inherent speed limitation of electronic signal processors.

Chapter 6

Photonic Temporal Signal Processing Based on SOI Interferometers

Photonic temporal signal processing functions, such as temporal integration, temporal differentiation, and temporal Hilbert transformation, based on a III-V material system have been discussed in the previous chapters. The III-V material system can provide both passive and active components integration in a single chip, which includes waveguides, tunable couplers, PMs, and SOAs. A reconfigurable photonic signal processor is achievable in such an integration platform; however, the size of the processor is large, and the fabrication cost is high comparing to the CMOS enabled silicon photonic chips. In this Chapter, photonic temporal differentiation is investigated based on SOI interferometers, which has a compact footprint due to the strong refractive index contrast between silicon and silica. The fabrication cost for CMOS compatible silicon chips can be largely reduced for massive production.

6.1 Photonic Temporal Differentiation Based on Passive and Active SOI Interferometers

In this chapter, two photonic integrated tunable fractional order temporal differentiator based on MZI structures implemented in a CMOS compatible SOI

platform are proposed. In the passive design, an MMI is used as one of the two couplers in the MZI. By changing the polarization state of the input signal, the coupling coefficient of the MMI can be tuned [80]. Correspondingly, the phase shift in the destructive-interference wavelength is changed, which leads to a tunable fractional order of the photonic temporal differentiator. In the active design, the photonic temporal differentiator uses two cascaded MZIs, a balanced MZI and an unbalanced MZI. A phase modulator (PM) is incorporated in one of the two arms of each MZI, as a result, the balanced MZI with a PM forms a tunable coupler, which is used to tune the fractional order of the active differentiator. The PM in the unbalanced MZI is used to tune the operation wavelength. The two photonic temporal differentiators are designed and fabricated in a CMOS compatible SOI platform, and their performance is evaluated experimentally. The experimental results show that both differentiators can have a tunable fractional order from 0 to 1. In addition, the use of the active temporal differentiator to perform high speed coding with a data rate of 16 Gbps is also experimentally evaluated.

6.2 SOI Design for Photonic Temporal Differentiation

An *n*-th order temporal differentiator provides the *n*-th order time derivate of the envelope of an optical signal, which can be implemented by an MZI as discussed in Chapter 2 and 3, and shown in Fig. 6-1 (a), (b), and (c).

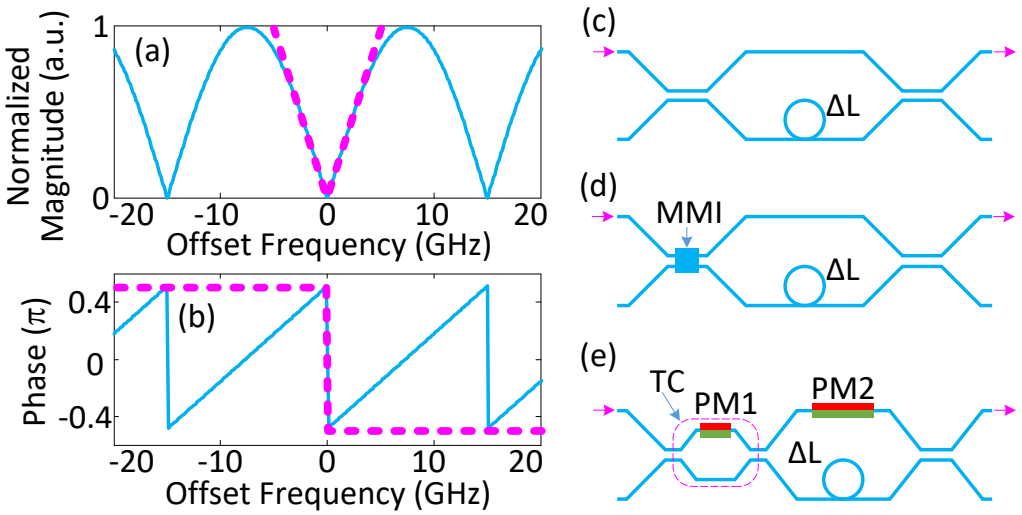

Fig. 6-1. (a) The spectral and (b) phase responses of an MZI (solid line) and a photonic temporal differentiator (dashed line). (c) An MZI with a length difference between the two arms. (d) The passive and (e) active design concept of a tunable fractional photonic temporal differentiator based on an SOI MZI. MMI: multimode interference; PM: phase modulator; TC: tunable coupler.

To achieve a tunable fractional order in a photonic temporal differentiator, a tunable coupler has to be used as one of the two couplers in the MZI to achieve a tunable phase shift at a destructive-interference wavelength. In a CMOS compatible SOI platform, a tunable coupler can be implemented by a 2×2 MMI in the passive approach as shown in Fig. 6-1(d) or by an MZI coupler with a PM in one of its two arms in an active approach as shown in Fig. 6-1(e).

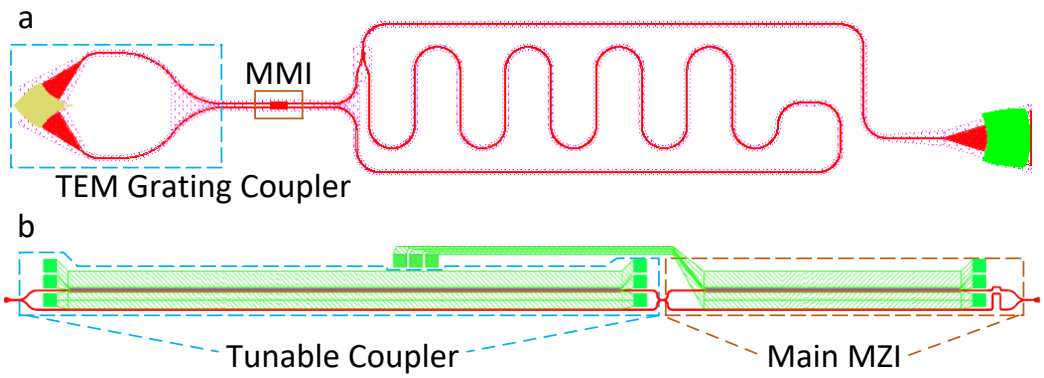

Fig. 6-2. (a) The passive design layout of the proposed photonic temporal differentiator based on an MZI with an MMI coupler. The length difference between the two MZI arms is ΔL =780 μm. (b) The active design layout of the photonic temporal differentiator based on two cascaded MZIs with a PM on one of the two arms for each MZI. The PM is designed with a PN junction. The length difference of the two MZI arms for the two designs is ΔL =160 μm.

The design of a photonic temporal differentiator based on an MZI in a passive SOI platform is given in Fig. 6-2(a). A TEM grating coupler supporting both TE and TM modes is used to couple optical signal from a cleaved optical fiber into the chip. The first coupler in the MZI is implemented by a 2×2 MMI with a dimension of 7.5 μm × 3 μm to provide a 3 dB power splitting ratio for a TE input optical signal. By changing the polarization state of the input optical signal, the coupling coefficient of the MMI can be tuned, which provides a phase shift change in the destructive-

interference wavelengths and leads to a tunable fractional order of the photonic temporal differentiator. The length difference between the two MZI arms is 780 μm which corresponds to a free spectral range (FSR) of ~110 GHz in the frequency response of the MZI. With such a compact design, the footprint of the passive photonic differentiator has a dimension of 450 μm × 65 μm. The tuning of the fractional order is achieved by adjusting the polarization states of the input optical signal, and the operation wavelength is not tunable.

The design of a photonic temporal differentiator based on an MZI in an active SOI platform is given in Fig. 6-2(b). As shown in Fig. 6-2(b), a tunable coupler implemented by an MZI with a PM in one of its two arms is used as the first coupler in the main MZI with a length of 1 mm. The PM is implemented by a pn junction in the SOI platform, which has a bandwidth of ~25 GHz with a length of 4 mm. By applying a DC voltage or a radio frequency (RF) signal to the PM, the coupling coefficient of the tunable coupler can be changed, which leads to the tuning of the fractional order. Followed by the tunable coupler, the two arms of the main MZI has a length difference of 500 μm, which corresponds to a FSR of ~170 GHz in the frequency response of the MZI. A second PM with a length of 2.3 mm is also incorporated in one of the two arms of the main MZI to provide a tunable operation wavelength for the photonic temporal differentiator. A first grating coupler is used to couple optical signal from a cleaved optical fiber into the chip and a second

grating coupler is used to couple the differentiated optical signal out of the chip. Due to the large size of the PMs used in the design, the footprint of such an active photonic temporal differentiator has a dimension of 0.32 mm × 7.7 mm, which is smaller than the InP chip with a size of 1.5 mm × 2 mm. But the SOI device lacks of reconfigurability for different functions.

6.3 Experimental Results

The proposed photonic temporal differentiators as shown in Fig. 6-2 are fabricated using a CMOS compatible process with 193-nm deep ultraviolet lithography. The strip waveguides in the device have a width of 500 nm and a height of 220 nm, which are fabricated on top of a buried oxide layer (2 μm thick) on a silicon wafer. The silicon rib waveguide for phase modulation has an etching depth of 70 nm. The doping concentrations in the p- and n-doped regions of the PIN diode were standard from the shared wafer project managed by CMC across Canada. Fig. 6-3 presents the SEM and microscope pictures of the fabricated devices. Specifically, Fig. 6-3(a) shows a passive photonic temporal differentiator. The 2-D grating coupler is standard device from the IMEC PDK library, which is shown in Fig. 6-3(b) and (c), and the fabricated MMI is shown in Fig. 6-3(d) which has a dimension of 8.130 μm × 3.088 μm closely matched with the design dimension of 7.5 μm × 3 μm. Fig. 6-3(e) shows the fabricated active photonic temporal differentiator.

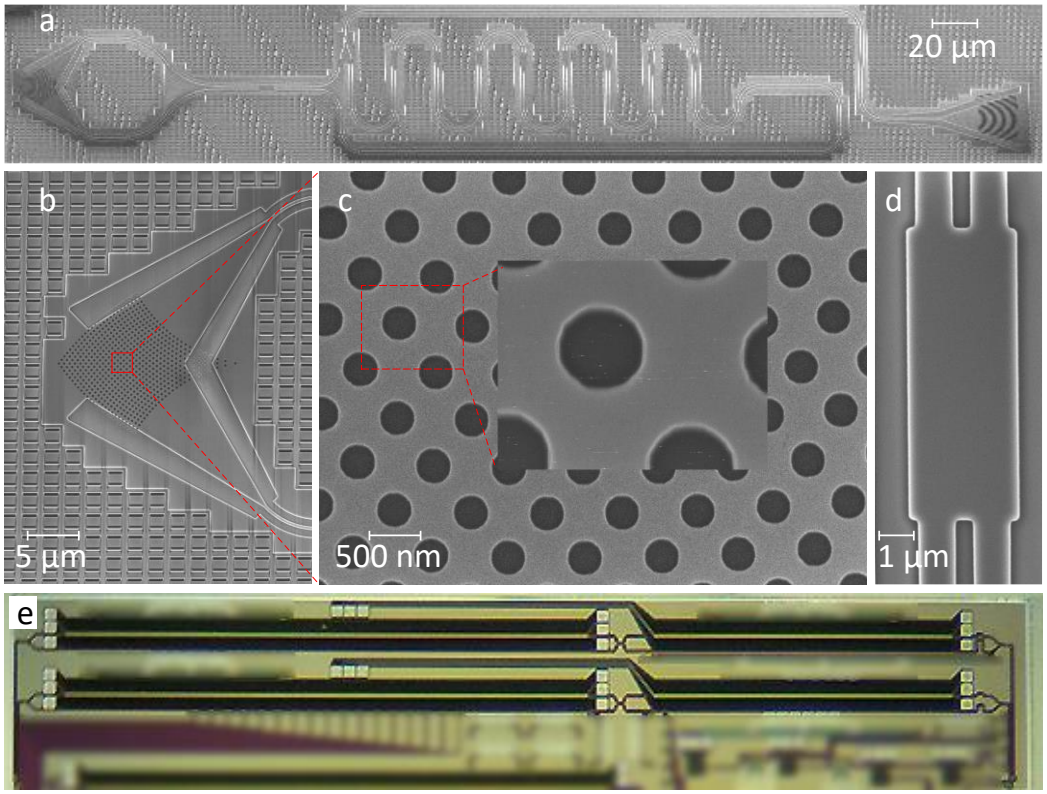

Fig. 6-3. Fabrication results. (a) SEM picture of the fabricated passive photonic temporal differentiator based on an MZI, (b) the TEM grating coupler, (c) the zoom-in view of the 2-D grating coupler, and (d) the MMI with an actual fabricated dimension of 8.130 μm×3.088 μm. (e) The microscope view of the fabricated active photonic temporal differentiator.

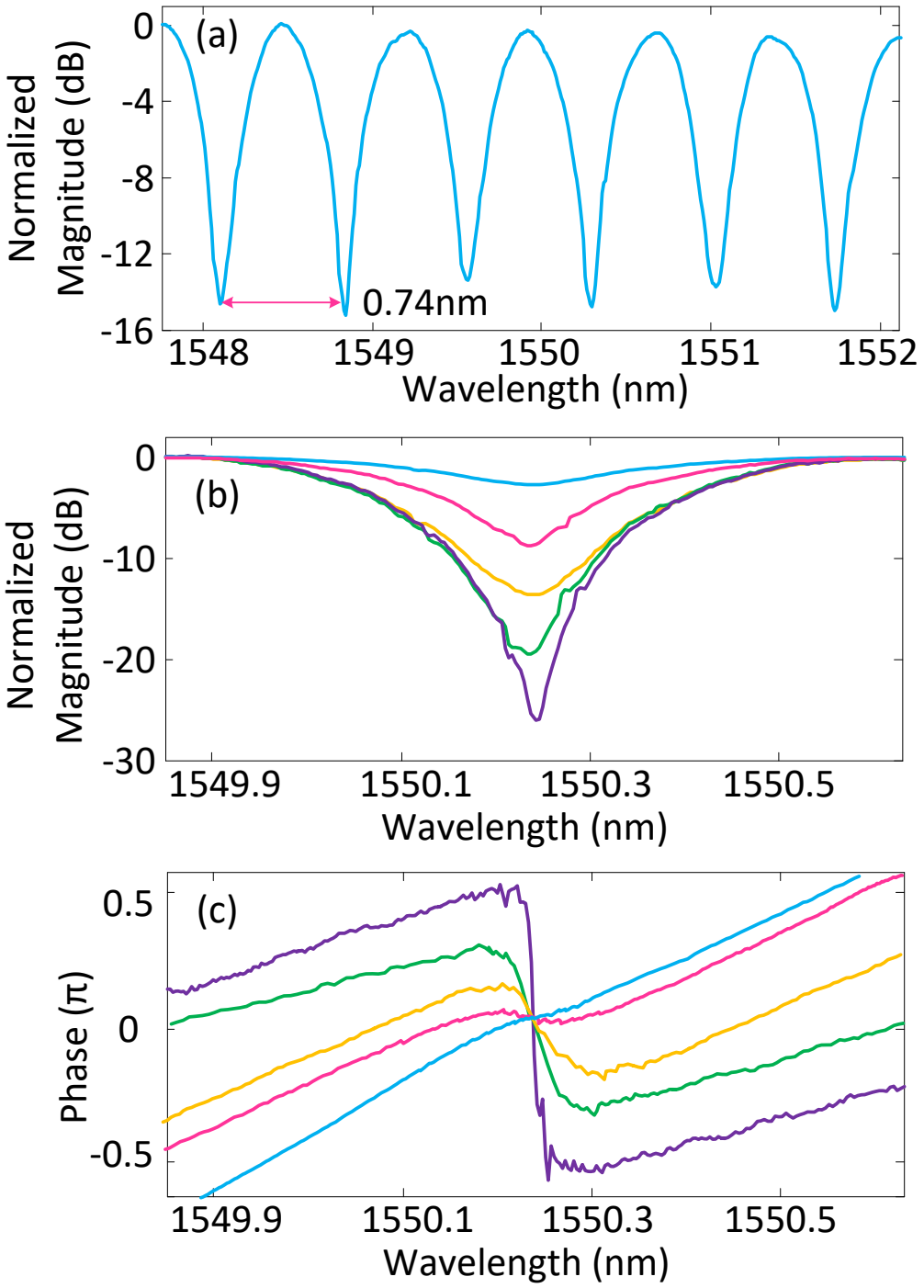

Fig. 6-4. Experimental results of the passive photonic temporal differentiator. (a) The spectral response of the of the MZI photonic temporal differentiator. (b) The spectral response and (c) phase response of the differentiator when tuning the polarization state of the input optical signal.

A. Passive Design

An experiment to measure and demonstrate the fabricated passive photonic temporal differentiator is implemented. The spectral response of the differentiator is firstly measured by an optical vector analyzer (OVA, Lunar) as shown in Fig. 6-4(a). As can be seen, the measured FSR is 0.74 nm (or 92.4 GHz), which is the maximum processing bandwidth of the differentiator. By changing the polarization state of the input optical signal, the spectral response and phase shift at the destructive-interference wavelength are changed as shown in Fig. 6-4(b) and (c).

An optical Gaussian pulse train generated by a mode-locked laser (MLL, Pritel 1550-nm Picosecond and Femtosecond Fiber Lasers) with a pulse width of 11.8 ps and a repetition rate of 40 MHz is sent to the passive differentiator through a polarization controller (PC). Fig. 6-5(a) shows a single Gaussian pulse in the pulse train. By controlling the polarization state of the input Gaussian pulse, a temporal differentiated pulse with a tunable fractional order is obtained. To observe the differentiated pulse, the optical signal at the output of the on-chip differentiator is applied to a 53-GHz photodetector (PD) and monitored by a sampling oscilloscope (OSC, Agilent 86100C). Fig. 6-5(b), (c), and (d) shows the differentiated pulse with a fractional order of 0.55, 0.85, and 1, respectively. Simulation results of an ideal differentiator are also given in Fig. 6-5(b), (c), and (d) (dashed lines). As can be seen, the experimental results have a good agreement with the simulated results. It

should be noted that the difference in the notch between experimental and simulation results is caused mainly by the limited bandwidth of the PD (53 GHz), and the difference in the tail is due to the non-ideal Gaussian profile of the input pulse as shown in Fig. 6-5(a).

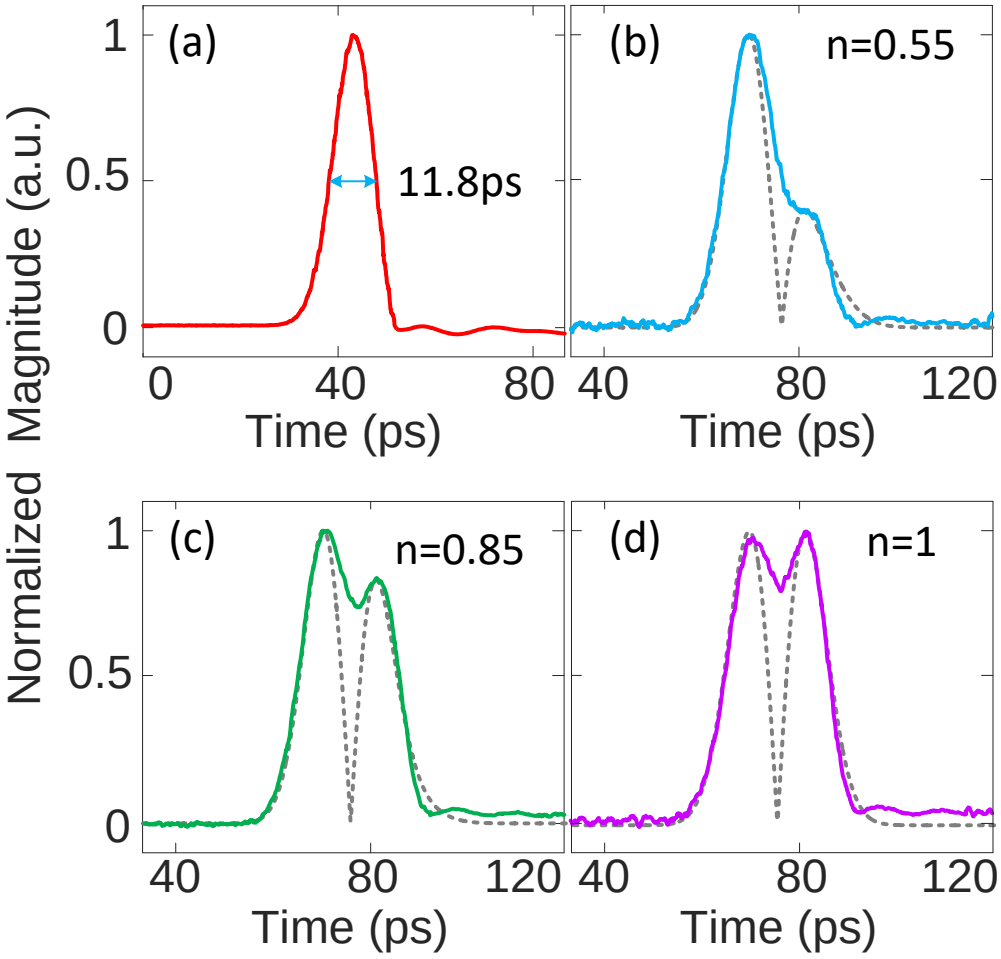

Fig. 6-5. Experimental results of the passive photonic temporal differentiator. (a) The input Gaussian pulse with temporal width of 11.8 ps. (b-d). The measured (solid) and simulated (dashed) fractional differentiation of the input Gaussian pulse with a fractional order of (b) 0.55, (c) 0.85, and (d) 1.

B. Active Design

An experiment to measure and demonstrate the fabricated active photonic temporal differentiator is also implemented. The spectral responses of the active differentiator while applying a voltage of -1.0, -2, and -3V to the PM in the second MZI (PM2), as shown in Fig. 6-1(e), are measured by an optical vector analyzer (OVA, Lunar Technologies), as shown in Fig. 6-6(a). As can be seen, the measured FSR is 1.37 nm (or 171.1 GHz), which is the maximum processing bandwidth of the differentiator. By changing the voltage applied to the PM in the first MZI (PM1), the spectral response and phase shift at the destructive-interference wavelength are changed as shown in Fig. 6-6(b) and (c). The 3dB bandwidths of PM1 and PM2 are also measured to be 24.2 GHz and 5 GHz, respectively. PM2 is used for wavelength tuning with an injection current (low speed). The two PMs are different in design, the termination ports of PM2 have been re-routed to the edge (Layout given in the Appendix), which is not length matched. Therefore, its bandwidth is lower than PM1 due to strong reflection.

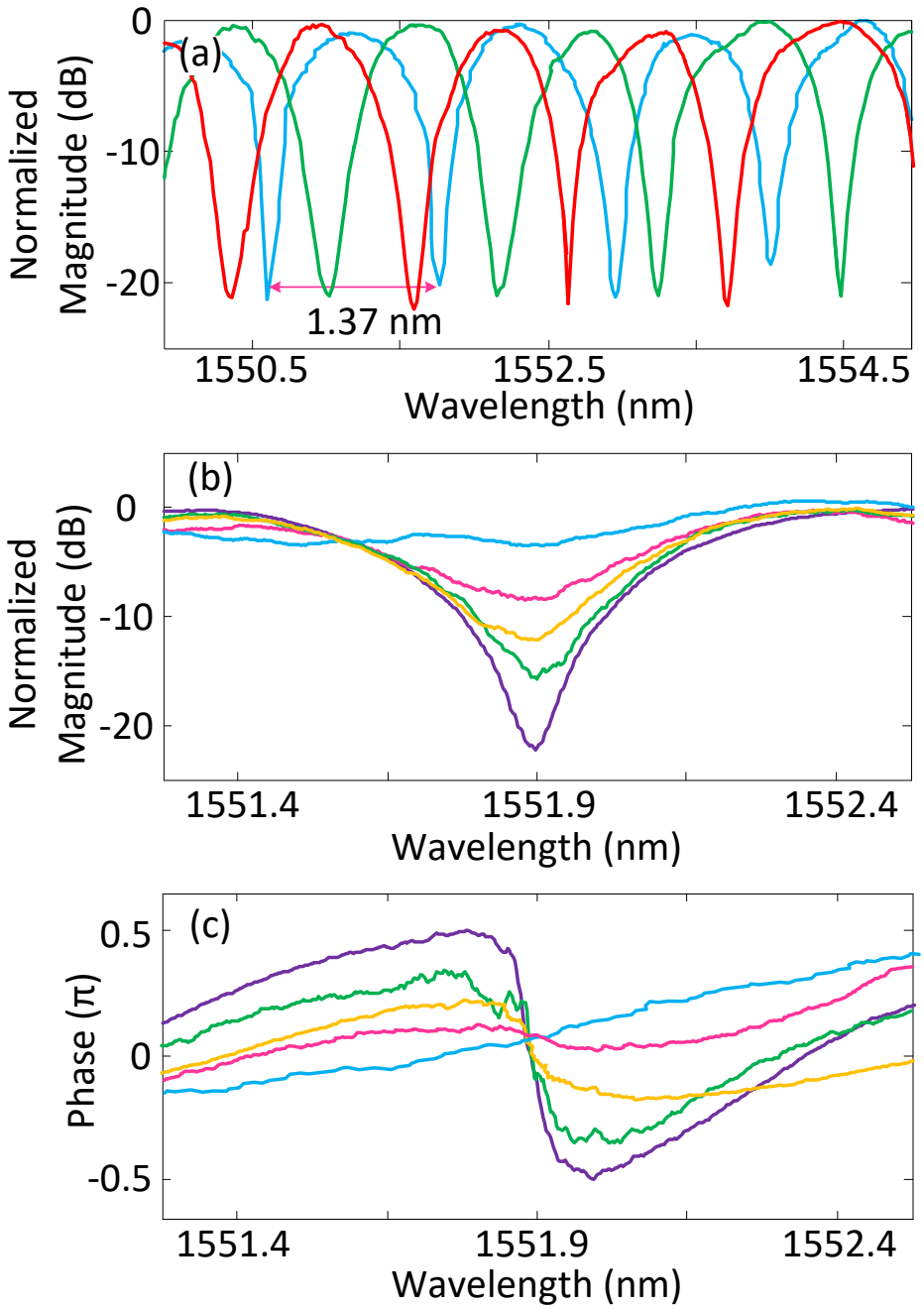

Fig. 6-6. Experimental results of the active photonic temporal differentiator. (a) The spectral response of the of the MZI photonic temporal differentiator when applying three different voltages to the PM in the second MZI. (b) The spectral response and (c) phase response of the differentiator when the voltage to the PM in the first MZI is tuned at five different values.

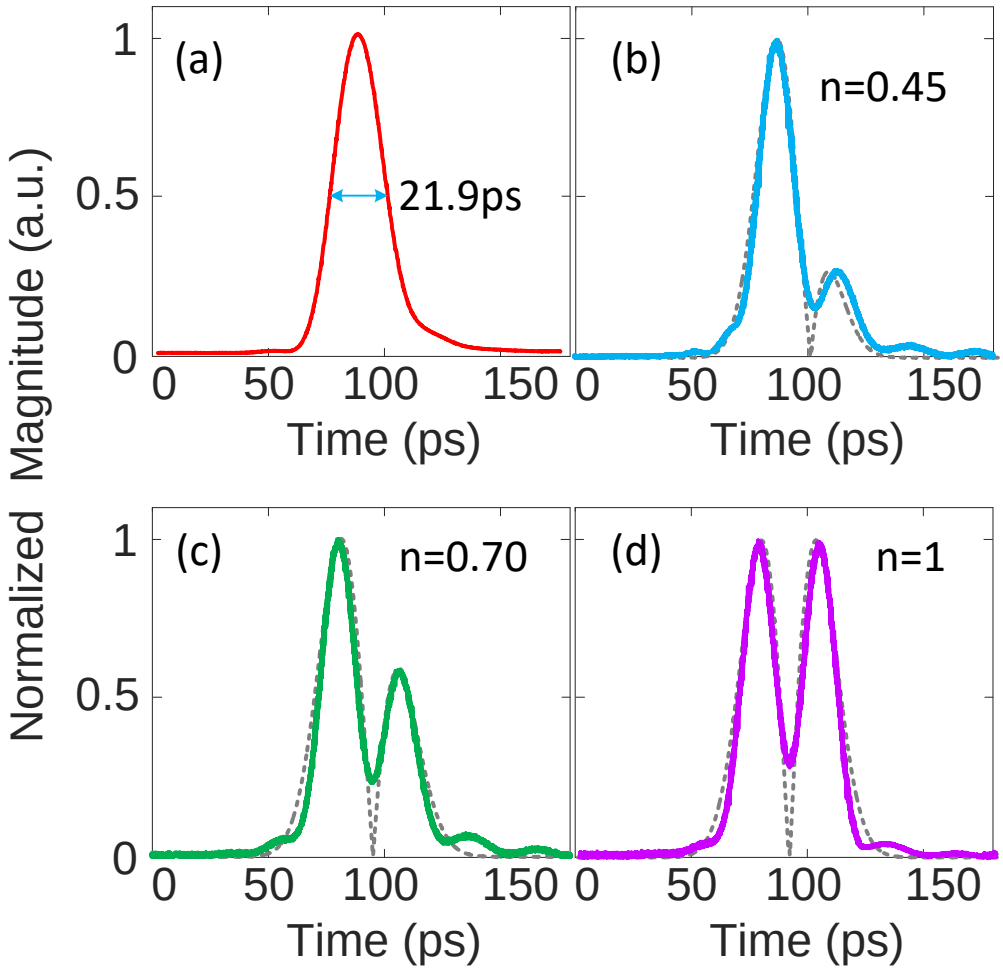

Fig. 6-7. Experimental results of the active photonic temporal differentiator. (a) The input Gaussian pulse with temporal width of 21.9 ps. The measured (solid) and simulated (dashed) fractional differentiator of the input Gaussian pulse with a fractional order of (b) 0.45, (c) 0.70, and (d) 1.

An optical Gaussian pulse train generated by an MLL (Pritel 1550-nm Picosecond and Femtosecond Fiber Lasers) with a pulse width of 21.9 ps and a repetition rate

of 40 MHz is sent to the active photonic temporal differentiator through a PC, as shown in Fig. 7(a). By changing the voltage applied to PM1, temporally differentiated pulses with a fractional order of 0.45, 0.70, and 1 are obtained, which are detected by using a 53-GHz PD and observed by an OSC (Agilent 86100C), as shown in Fig. 6-7(b), (c), and (d), respectively. Simulation results of an ideal photonic temporal differentiator are also given in Fig. 6-7(b), (c), and (d) (dashed lines). As can be seen, the experimental results have a good agreement with the simulated results except some small difference in notch depth. It should be noted that the small difference in the notch depth between the experimentally generated and simulated pulses are also resulted from the limited bandwidth of the PD, which has a bandwidth of 53 GHz.

C. High Speed Coding

As shown in Fig. 6-7, a tunable fraction order photonic temporal differentiator can shape a Gaussian pulse into a differentiated pulse with a tunable fractional order. Therefore, a high-speed coding system can be implemented based on such a differentiator, in which the coding can be done by applying a coding signal to PM1, as shown in Fig. 6-8(a). Fig. 6-8(b) shows the coding map. To represent a 2-bit data sequence, a Gaussian pulse train can be differentiated with a fractional order of 0, 0.5, 1, and 1.5 by applying a 4-level data sequence to PM1. As shown in Fig. 6-8(a), a continuous wave (CW) light wave with a wavelength of 1551.9 nm is

generated by a tunable laser source (TLS, Agilent N7714A) and sent to a Mach-Zehnder modulator (MZM) through a PC. The light wave is modulated by an electric Gaussian pulse train with a repetition rate of 8 GHz generated by an arbitrary waveform generator (AWG, Keysight M8195A) as shown in Fig. 6-9(a). The modulated light wave is then sent to the active photonic temporal differentiator by a cleaved optical fiber through a grating coupler. A synchronized 4-level data sequence generated by the AWG, as shown in Fig. 6-9(b), is applied to PM1 in the differentiator with a controllable DC bias by a bias tee. A coded pulse train is obtained is obtained at the output of the differentiator, which is monitored by a digital storage oscilloscope (DSO, Agilent DSO-X 93204A), as shown in Fig. 6-9(c). A close view of the coded pulse train from in a 1 ns scale is also shown in Fig. 6-9(d). As can be seen, the proposed active photonic temporal differentiator can be used for high speed coding with a data rate of 16 Gbps.

To decode the received signal, the correlation between the received encoded signal and a signature sequence is required, which can be performed by an analog correlator or a digital correlator. For the use of an analog correlator, sampling before decoding is not needed, however, sampling and digitization are required if digital processing for correlation is used.

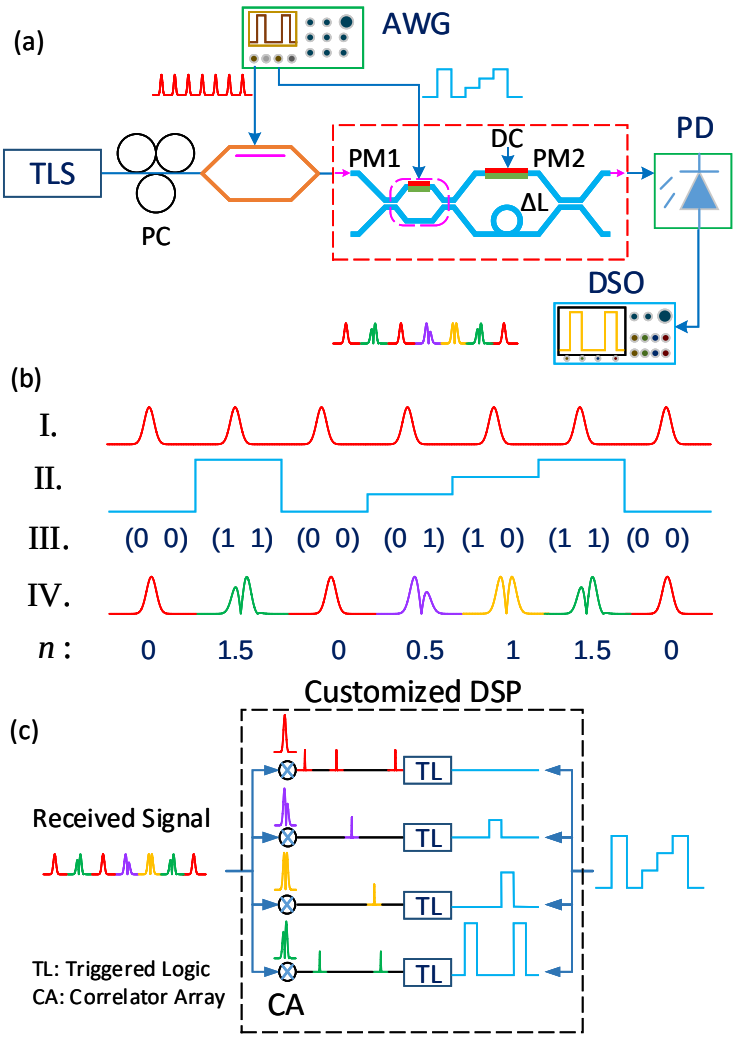

Fig. 6-8. (a) Schematic of a high-speed coding system based on the active photonic temporal differentiator. (b) The coding map of the proposed high speed coding system with (I) a Gaussian pulse train, (II) a 4-level data sequence, (III) a mapping 2-bit data sequence, and (IV) the coded differentiation pulse train. (c) The diagram of a digital decoding receiver.

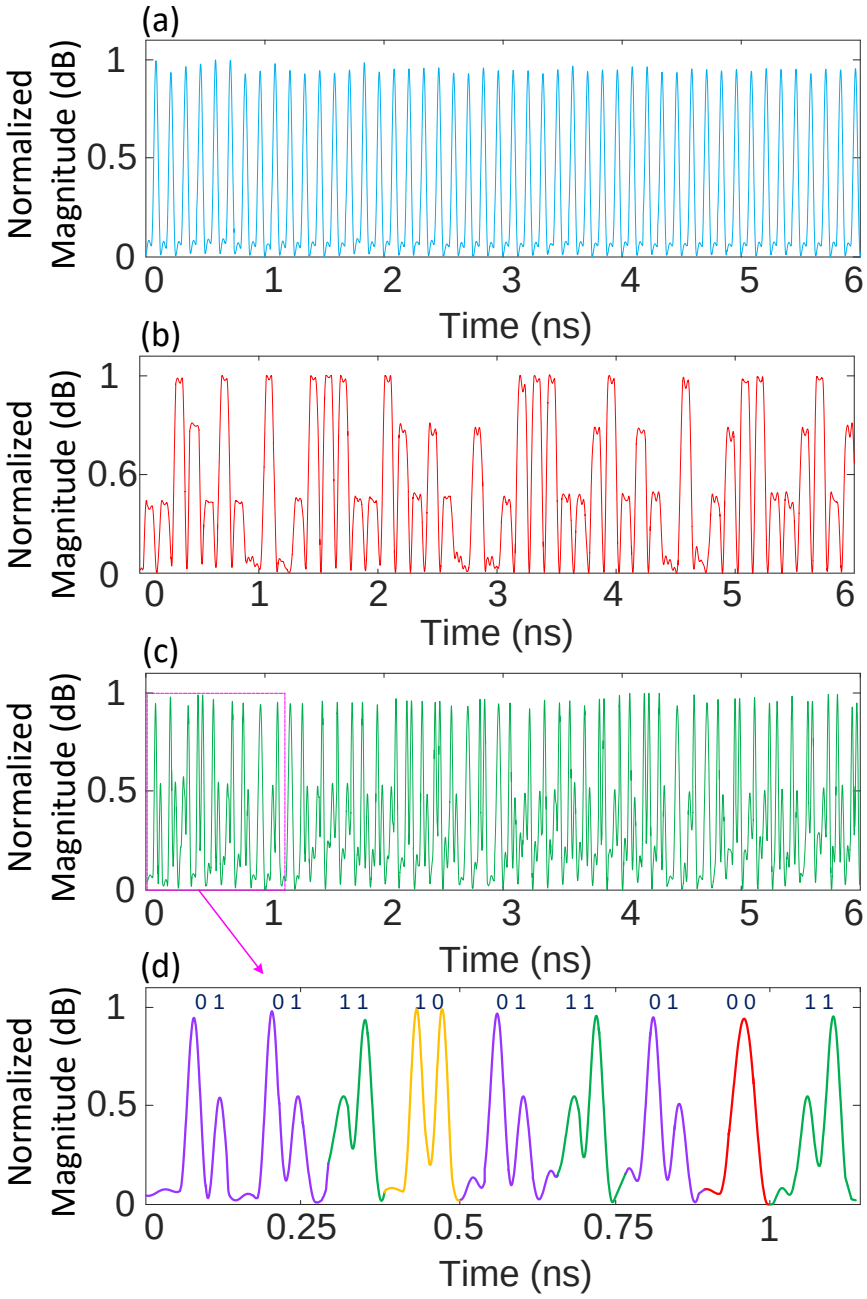

Fig. 6-9. Experimental results of high speed coding based on the active photonic differentiator. (a) The Gaussian pulse train with a repetition rate of 8 GHz. (b) The synchronized 4-level data sequence used for high speed coding. (c) The generated differentiation pulse train with coded data. (d) A close view of the generated pulse train shown in (c).

For example, the decoding process based on correlation can be performed in a customized DSP as shown Fig. 6-8(c). The digitized received signal is equally split into four sub-signal sequences. For each of the sub-signal sequence, a correlation is performed between the sub-signal sequence and one of the four signature signals, which are determined in the transmitter when the signal is generated and encoded. After the correlation, the four signature signals are found in the four sub-signal sequences with a correlation peak, respectively. The correlation peaks can be converted into multilevel voltage signals by triggered logics, which can be combined into a sequence of multilevel voltage signal. In this way, the encoded signal can be successfully decoded. Those mentioned processes can be implemented in a customized DSP for real time decoding processing.

6.3 Summary

In this chapter, two integrated fractional-order photonic differentiators based on MZI structures implemented on an SOI platform with passive and active tuning of the fractional orders were proposed and experimentally evaluated. In the design of the passive fractional-order photonic temporal differentiator, an MMI was incorporated into the MZI as one of the two couplers. A tunable fractional order from 0 to 1 was achieved by changing the polarization state of the input optical

signal. In the design of the active fractional-order photonic temporal differentiator, two cascaded MZIs were used with each having a PM in one arm to achieve active fractional order and wavelength tuning. The tunable fractional order and the tunable operation frequency were achieved by changing the voltage applied to the two PMs (PM1 and PM2). In the experiment demonstration, for both differentiators, the differentiation of a Gaussian pulse with a pulse width of 21.9 ps was achieved with a fractional order from 0 to 1. The active photonic temporal differentiator was also evaluated for its use for high speed coding. In the experiment, a coding signal with a data rate of 16 Gbps was generated. The coding system can find important applications in secure communications.

Chapter 7

Conclusions and Future Work

7.1 Conclusion

The objectives of this work: 1) to demonstrate a fully reconfigurable photonic signal processor, and 2) to experimentally demonstrate photonic temporal integration, differentiation, and Hilbert transformation in a single PIC. The objectives have been met.

In Chapter 2, a background review of photonic signal processing was presented. The advantages and limitations of the previous photonic signal processing systems were discussed.

In Chapter 3, the theory model for photonic temporal integration, differentiation, and Hilbert transformation was presented. The transfer functions of different optical geometries to implement the mentioned three basic photonic signal processing functions was developed and the design of a reconfigurable photonic signal processor was provided.

In Chapter 4, a single ring resonator was designed and fabricated in the III-V material system, which was experimentally demonstrated to implement a photonic

temporal integrator and a Hilbert transformer. A temporal integration time of 6331 ps with a bandwidth of 0.12 nm was obtained. The temporal integration of different input waveforms was also investigated, which confirmed the effective operation of the proposed temporal integrator. A photonic FHT was also experimentally demonstrated based on the ring resonator, which provides both continuously tunable fractional order and tunable operation wavelength.

In Chapter 5, a fully reconfigurable photonic integrated signal processor based on a photonic integrated circuit was designed, fabricated and demonstrated. The operation of the signal processor reconfigured as a temporal integrator, a temporal differentiator and a Hilbert transformer with a tunable order and a tunable operation wavelength was demonstrated experimentally. In particular, a temporal integrator over a bandwidth of 0.22 nm with an integration time of 10.9 ns was achieved, which is the longest integration time ever reported. This work represents an important step towards the realization of a fully programmable high speed and wideband general-purpose photonic signal processors that can overcome the inherent speed limitation of electronic signal processors.

In chapter 6, a passive and an active tunable fractional order photonic temporal differentiator based on an MZI in a CMOS compatible SOI platform were proposed and experimentally demonstrated. By using an MMI as one of the two couplers in

the passive MZI, a tunable fractional order from 0 to 1 was achieved by changing the polarization state of the input optical signal. By incorporating two PMs into the MZIs in the active design, a tunable fractional order and a tunable operation frequency were achieved by changing the voltage applied to the PMs (PM1 and PM2). A differentiation operation of a Gaussian pulse train with a pulse width of 21.9 ps was experimented demonstrated with a fractional order from 0 to 1. A high speed coding system based on the active differentiator was also experimentally demonstrated with a data rate of 16 Gbps. The coding system can find important applications in secure communications.

7.2 Future Work

The implementations of a photonic integrator and Hilbert transformer require a ring resonator with a high *Q* factor, which can be achieved by using a gain medium in the ring resonator. However, the implementation of such a gain ring resonator in a SOI platform is not feasible due to the indirect band-gap nature of silicon. On the other hand, an SOI platform does provide a much smaller device footprint, a lower insertion loss, and a lower cost for massive production compared with the III-V material system. To combine the advantages offered by III-V and SOI material systems, the next generation photonic signal processors can be implemented based on a hybrid approach, in which the III-V and Silicon are combined to both light

generation and processing, to make photonic signal processors have a higher bandwidth, a smaller footprint, and a lower power consumption. To date, there are two techniques to integrate III-V components on a SOI platform.

1) Chip bonding. In this technique, a III-V component or functional block (a die or wafer) is bonded onto a target silicon chip by flip chip bonding [81]. The flip-chip bonding process is simple and mature, however, the coupling loss between the III-V components and the silicon waveguides is large.
2) Hetero-epitaxy growth. In this technique, heteroepitaxial growth of high quality III-V material on Si is used to integrate active III-V components on a SOI platform [82]. This technique reduces the coupling loss between III-V components and silicon waveguides. However, differences in atomic lattice constants and thermal expansion coefficients between the III-V and silicon leads to increased fabrication defects.

Those techniques are being intensively developed, but there are challenges to increase the yields. As a future work, a fully integrated reconfigurable signal processor based on a hybrid III-V and SOI platform will be developed, to provide a larger processing bandwidth, a smaller size, and a lower cost.

REFERENCES

[1] J. M. F. Moura, "What is Signal Processing?," *IEEE Signal Processing magazine,* vol. 26, no. 6, pp. 6-6, Nov. 2009.

[2] A. Antoniou, Digital Signal Processing: Signals, Systems, and Filters., New York: McGraw-Hill, 2006.

[3] D. F. Elliott, Handbook of Digital Signal Processing: Engineering Applications, New York: Academic Press, 2013.

[4] M. B. Yeary, R. J. Fink, D. Beck, D. Guidry and M. Burns, "A DSP-based mixed-signal waveform generator," *IEEE Trans. Instrum. Meas.*, vol. 53, no. 3, pp. 665-671, Jun. 2004.

[5] X. Zhou, J. Huo, K. Zhong, L. WANG, J. Yuan, H. Cheng, K. Long, A. P. T. Lau and C. Lu, "PDM PAM-4 with IM-DD using a simple MIMO DSP-based receiver for short reach communications," in *Asia Communications and Photonics Conference 2015*, Hong Kong, 2015.

[6] T. B. Welch, C. H. G. Wright and M. G. Morrow, "The DSP of money," in *IEEE International Conference on Acoustics, Speech and Signal Processing*, Taipei, 2009.

[7] F. K. Schneider, A. Agarwal, Y. Yoo, T. Fukuoka and Y. Kim, "A Fully Programmable Computing Architecture for Medical Ultrasound Machines,"

IEEE Trans. Information Technology in Biomedicine, vol. 14, no. 2, pp. 538-540, Mar. 2010.

[8] S. Kuo and B. Lee, Real-Time Digital Signal Processors: Implementations, Applications and Experiments with the TMS320C55x, New York: Wiley, 2001.

[9] "TI simplifies direct RF sampling system architecture with the highest dynamic range, widest bandwidth and fastest 14-bit ADC," Texas Instruments, 18 May 2016. [Online]. Available: http://newscenter.ti.com/2016-05-18-TI-delivers-the-industrys-first-RF-sampling-14-bit-3-GSPS-analog-to-digital-converter. [Accessed 13 May 2017].

[10] R. A. Minasian, "Photonic signal processing of microwave signals," *IEEE Trans. Microw. Theory Tech.*, vol. 54, no. 2, pp. 832-846, Feb. 2006.

[11] J. Capmany, J. Mora, I. Gasulla, J. Sancho, J. Lloret and S. Sales, "Microwave photonic signal processing," *J. Lightwave Technol.*, vol. 31, no. 4, pp. 571-586, Oct. 2012.

[12] M. Kahn, H. Shen, Y. Xuan, L. Zhao, S. Xiao, D. Leaird, A. Weiner and M. Qi, "Ultrabroad-bandwidth arbitrary radiofrequency waveform generation with a silicon photonic chip-based spectral shaper," *Nature Photon.*, vol. 4, no. 2, pp. 117-122, Feb. 2010.

[13] R. Yu, S. Cheung, Y. Li, K. Okamoto, R. Proietti, Y. Yin and S. J. B. Yoo, "A scalable silicon photonic chip-scale optical switch for high performance computing systems," *Opt. Express*, vol. 21, no. 26, pp. 32655-32667, Dec. 2013.

[14] A. E. Willner, S. Khaleghi, M. R. Chitgarha and O. F. Yilmaz, "All-optical signal processing," *J. Lightwave Technol.*, vol. 32, no. 4, pp. 660-680, Feb. 2014.

[15] C. Koos, P. Vorreau, T. Vallaitis, P. Dumon, W. Bogaerts, R. Baets, B. Esembeson, I. Biaggio, T. Michinobu, F. Diederich, W. Freude and J. Leuthold, "All-optical high-speed signal processing with silicon-organic hybrid slot waveguides," *Nat. Photonics*, vol. 3, no. 4, pp. 216-219, Apr. 2009.

[16] A. M. Weiner, "Ultrafast optical pulse shaping: A tutorial review," *Opt. Commun.*, vol. 284, no. 15, p. 3669–3692, Jul. 2011.

[17] V. R. Almeida, C. A. Barrios, R. Panepucci and M. Lipson, "All-optical control of light on a silicon chip," *Nature*, vol. 431, no. 7012, p. 1081–1084, Oct. 2004.

[18] C. R. Doerr and K. Okamoto, "Advances in silica planar lightwave circuits," *J. Lightwave Technol.*, vol. 24, no. 12, pp. 4763-4789, Dec. 2006.

[19] R. Slavík, Y. Park, N. Ayotte, S. Doucet, T. Ahn, S. LaRochelle and J. Azaña, "Photonic temporal integrator for all-optical computing," *Opt. Express,* vol. 16, no. 22, pp. 18202-18214, Oct. 2008.

[20] N. Q. Ngo, S. F. Yu, S. C. Tjin and C. H. Kam, "A new theoretical basis of higher-derivative optical differentiators," *Opt. Comm.,* vol. 230, no. 1-2, pp. 115-129, Jan. 2004.

[21] H. Shahoei, P. Dumais and J. P. Yao, "Continuously tunable photonic fractional Hilbert transformer using a high-contrast Germanium-doped silica-on-silicon microring resonator," *Opt. Lett.,* vol. 39, no. 9, pp. 2778-2781, May 2014.

[22] L. A. Coldren and S. W. Scorzinne, Diode Lasers and Photonic Integrated Circuits, Hoboken: Wiley, 1995.

[23] T. L. Koch, U. Koren, M. Dagenais, R. F. Leheny and J. Crow, Integrated Optoelectronics, Academic, 1995, pp. 557-626.

[24] D. Pérez, I. Gasulla, J. Capmany, J. S. Fandiño, P. Muñoz and H. Alavi, "Figures of merit for self-beating filtered microwave photonic systems," *Opt. Express,* vol. 24, no. 9, pp. 10087-10102 , Apr. 2016.

[25] D. Pérez, I. Gasulla, J. Capmany and R. A. Soref, "Reconfigurable lattice mesh designs for programmable photonic processors," *Opt. Express,* vol. 24, no. 11, pp. 12093-12106, May 2016.

[26] R. Ashrafi, M. R. Dizaji, L. R. Cortés, J. Zhang, J. P. Yao, J. Azaña and L. R. Chen, "Time-delay to intensity mapping based on a second-order optical integrator: application to optical arbitrary waveform generation," *Opt. Express,* vol. 23, no. 12, pp. 16209-16223, Jun. 2015.

[27] N. Q. Ngo and L. N. Binh, "Optical realization of Newton-Cotes-based integrators for dark soliton generation," *J. Lightw. Technol.,* vol. 24, no. 1, pp. 563-572, Jan. 2006.

[28] M. T. Hill, H. J. S. Dorren, T. d. Vries, X. J. M. Leijtens, J. H. d. Besten, B. Smallbrugge, S. Oei, J. J. M. Binsma, G. D. Khoe and M. K. Smit, "A fast low power optical memory based on coupled micro-ring lasers," *Nature,* vol. 432, no. 7014, p. 206–209, 206–209.

[29] E. Reeves, P. Costanzo-Caso and A. Siahmakoun, "Theoretical study and demonstration of photonic asynchronous first-order delta-sigma modulator for converting analog input to NRZ binary output," *Microw. Opt. Technol. Lett.,* vol. 57, no. 3, pp. 574-578, Mar. 2015.

[30] M. H. Asghari and J. Azaña, "Design of all-optical high-order temporal integrators based on multiple-phase-shifted Bragg gratings," *Opt. Express,* vol. 16, no. 15, p. 11459–11469, Jul. 2008.

[31] M. H. Asghari and J. Azaña, "On the design of efficient and accurate arbitrary-order temporal optical integrators using fiber Bragg gratings," *J. Lightwave Technol.*, vol. 27, no. 17, p. 3888–3895, Sep. 2009.

[32] M. H. Asghari, C. Wang, J. Yao and J. Azaña, "High-order passive photonic temporal integrators," *Opt. Lett.*, vol. 35, no. 8, p. 1191–1193, Apr. 2010.

[33] Y. Park and J. Azaña, "Ultrafast photonic intensity integrator," *Opt. Lett.*, vol. 34, no. 8, p. 1156–1158, Apr. 2009..

[34] M. Ferrera, Y. Park, L. Razzari, B. E. Little, S. T. Chu, R. Morandotti, D. J. Moss and J. Azaña, "On-chip CMOS-compatible all-optical integrator," *Nature Commun.*, vol. 1, no. 29, pp. 1-5, Jun. 2010.

[35] M. Ferrera, Y. Park, L. Razzari, B. E. Little, S. T. Chu, R. Morandotti, D. J. Moss and J. Azaña, "All-optical first and second-order integration on a chip," *Opt. Express*, vol. 19, no. 23, pp. 23153-23161, Oct. 2011.

[36] F. Liu, T. Wang, L. Qiang, T. Ye, Z. Zhang, M. Qiu and Y. Su, "Compact optical temporal differentiator based on silicon microring resonator," *Opt. Express*, vol. 16, no. 20, p. 15880–15886, Sep. 2008.

[37] D. Hillerkuss, M. Winter, M. Teschke, A. Marculescu, J. Li, G. Sigurdsson, K. Worms, S. Ben Ezra, N. Narkiss, W. Freude and J. Leuthold, "Simple all-optical FFT scheme enabling Tbit/s real-time signal processing," *Opt. Express*, vol. 18, no. 9, pp. 9324-9340, Apr. 2010.

[38] D. Hillerkuss, R. Schmogrow, T. Schellinger, M. Jordan, M. Winter, G. Huber, T. Vallaitis, R. Bonk, P. Kleinow, F. Frey, M. Roeger, S. Koenig, A. Ludwig, A. Marculescu, J. Li, M. Hoh, M. Dreschmann, J. Meyer, S. Ben Ezra, N. Narkis, B. Nebendahl, F. Parmigiani, P. Petropoulos, B. Resan, A. Oehler, K. Weingarten, T. Ellermeyer, J. Lutz, M. Moeller, M. Huebner, J. Becker, C. Koos, W. Freude and J. Leuthold, "26 Tbps line-rate super-channel transmission utilizing all-optical fast Fourier transform processing," *Nature Photon.*, vol. 5, no. 6, p. 364–371, May 2011.

[39] F. Li, Y. Park and J. Azaña, "Complete temporal pulse characterization based on phase reconstruction using optical ultrafast differentiation (PROUD)," *Opt. Express*, vol. 32, no. 22, pp. 3364-3366, Nov. 2007.

[40] C. Sima, J. C. Gates, H. L. Rogers, P. L. Mennea, C. Holmes, M. N. Zervas and P. G. R. Smith, "Phase controlled integrated interferometric single-sideband filter based on planar Bragg gratings implementing photonic Hilbert transform," *Opt. Express*, vol. 38, no. 5, pp. 727-729, Mar. 2013.

[41] Y. Park, J. Azaña and R. Slavík, "Ultrafast all-optical first- and higher-order differentiators based on interferometers," *Opt. Lett.*, vol. 32, no. 6, pp. 710-712, Mar. 2007.

[42] M. H. Asghari and J. Azana, "Photonic integrator-based optical memory unit," *IEEE Photon. Technol. Lett.*, vol. 23, no. 4, pp. 209-211, Dec. 2010.

[43] R. Slavík, L. K. Oxenløwe, M. Galili, H. Mulvad, Y. Park, J. Azaña and P. Jeppesen, "Demultiplexing of 320 Gbit/s OTDM data using ultrashort flat-top pulses," *IEEE Photon. Technol. Lett.*, vol. 19, no. 22, pp. 1855-1857, Nov. 2007.

[44] M. Kulishov and J. Azaña, "Long-period fiber gratings as ultrafast optical differentiators," *Opt. Lett.*, vol. 30, no. 20, pp. 2700-2702, Oct. 2005.

[45] R. Slavík, Y. Park, M. Kulishov, R. Morandotti and J. Azaña, "Ultrafast alloptical differentiators," *Opt. Express*, vol. 14, no. 22, p. 10699–10707, Oct. 2006.

[46] L. M. Rivas, K. Singh, A. Carballar and J. Azaña, "Arbitrary-order ultrabroadband all-optical differentiators based on fiber Bragg gratings," *IEEE Photon. Technol. Lett.*, vol. 19, no. 16, pp. 1209-1211, Aug. 2007.

[47] R. Wang, R. Lin, M. Tang, H. Zhang, Z. Feng, S. Fu, D. Liu and P. Ping Shum, "Electrically programmable all-fiber structured second order optical temporal differentiator," *IEEE Photon. J.*, vol. 7, no. 3, pp. 1-11, Apr. 2015.

[48] C. Cuadrado-Laborde and M. V. Andrés, "In-fiber all-optical fractional differentiator," *Opt. Lett.*, vol. 34, no. 6, pp. 833-835, Mar. 2009.

[49] W. Zhang, W. Li and J. P. Yao, "Optical differentiator based on an integrated sidewall phase-shifted Bragg grating," *IEEE Photon. Technol. Lett.*, vol. 26, no. 23, pp. 2383-2386, Dec. 2014.

[50] J. Dong, A. Zheng, D. Gao, L. Li, D. Huang and X. Zhang, "Compact, flexible and versatile photonic differentiator using silicon Mach-Zehnder interferometers," *Opt. Exp.*, vol. 21, no. 6, pp. 7014-7024, Mar. 2013.

[51] M. H. Asghari and J. Azaña, "All-optical Hilbert transformer based on a single phase-shifted fiber Bragg grating: Design and analysis," *Opt. Lett.*, vol. 34, no. 3, p. 334–336, Feb. 2009.

[52] M. Li and J. P. Yao, "All-fiber temporal photonic fractional Hilbert transformer based on a directly designed fiber Bragg grating," *Opt. Lett.*, vol. 35, no. 2, pp. 223-225, Jan. 2010.

[53] M. Li and J. P. Yao, "Experimental demonstration of a wideband photonic temporal Hilbert transformer based on a single fiber Bragg grating," *IEEE Photon. Technol. Lett.*, vol. 22, no. 21, pp. 1529-1561, Nov. 2010.

[54] Y. Han, Z. Li, S. Pan, M. Li and J. P. Yao, "Photonic-assisted tunable microwave pulse fractional Hilbert transformer based on a temporal pulse shaping system," *IEEE Photon. Technol. Lett.*, vol. 23, no. 9, pp. 570-572, May 2011.

[55] Z. Li, W. Li, H. Chi, X. Zhang and J. P. Yao, "A continuously tunable microwave fractional Hilbert transformer based on a photonic microwave delay-line filter using a polarization modulator," *IEEE Photon. Technol. Lett.*, vol. 23, no. 22, pp. 1694-1699, Nov. 2011.

[56] Z. Li, Y. Han, H. Chi, X. Zhang and J. P. Yao, "A continuously tunable microwave fractional Hilbert transformer based on a nonuniformly-spaced photonic microwave delay-line filter," *J. Lightw. Technol.*, vol. 30, no. 12, pp. 1948-1953, Jun. 2012.

[57] C. Cuadrado-Laborde, "Proposal and design of a photonic in-fiber fractional Hilbert transformer," *IEEE Photon. Technol. Lett.*, vol. 22, no. 1, pp. 33-35, Jan. 2010.

[58] J. Dong, A. Zheng, Y. Zhang, J. Xia, S. Tan, T. Yang and X. Zhang, "Photonic Hilbert transformer employing on-chip photonic crystal nanocavity," *J. Lightw. Technol.*, vol. 32, no. 20, pp. 3704-3709, Oct. 2014.

[59] B. Liu, C. Sima, W. Yang, B. Cai, D. Liu, Y. Yu, J. Gates, M. Zervas and P. Smith, "Experimental investigation of large time–bandwidth product photonic Hilbert transformer based on compact Bragg grating," *IEEE Photon. Technol. Lett.*, vol. 8, no. 4, pp. 1-8, Aug. 2016.

[60] Y. Zhao, Z. Chen, Z. Ding, H. Ren and J. Stuart Nelson, "Real-time phase-resolved functional optical coherence tomography by use of optical Hilbert transformation," *Opt. Lett.*, vol. 27, no. 2, pp. 98-100, Apr. 2002.

[61] D. Cotter, R. J. Manning, K. J. Blow, A. D. Ellis, A. E. Kelly, N. Nesset, I. D. Phillips, A. J. Poustie and D. C. Rogers, "Nonlinear optics for high-speed

digital information processing," *Science*, vol. 286, no. 5444, p. 1523–1528, Nov. 1999.

[62] Y. Ding, X.-B. Zhang, X.-L. Zhang and D. Huang, "Active microring optical integrator associated with electroabsorption modulators for high speed low light power loadable and erasable optical memory unit," *Opt. Express*, vol. 17, no. 15, p. 12835–12848, Jul. 2009.

[63] J. Azaña, "Ultrafast analog all-optical signal processors based on fiber-Grating devices," *IEEE Photon. J.*, vol. 2, no. 3, pp. 359-386, Jun. 2010.

[64] Y. Park, T.-J. Ahn, Y. Dai, J. Yao and J. Azaña, "All-optical temporal integration of ultrafast pulse waveforms," *Opt. Express*, vol. 16, no. 22, p. 17817–17825, Oct. 2008.

[65] M. A. Preciado and M. A. Muriel, "Ultrafast all-optical integrator based on a fiber Bragg grating: proposal and design," *Opt. Lett.*, vol. 33, no. 12, pp. 1348-1350, Jun. 2008.

[66] R. Slavík, Y. Park, N. Ayotte, S. Doucet, T.-J. Ahn, S. LaRochelle and J. Azaña, "Photonic temporal integrator for all-optical computing," *Opt. Express*, vol. 16, no. 22, pp. 18202-18214, Oct. 2008.

[67] B. Mathieu, P. Melchior, A. Oustaloup and C. Ceyral, "Fractional differentiation for edge detection," *Signal Process.*, vol. 83, no. 11, p. 2421–2432, Nov. 2003.

[68] C. C. Tseng and S. C. Pei, "Design and application of discrete-time fractional Hilbert transformer," *IEEE Trans. Circuits Syst. II, Analog Digital Signal Process.*, vol. 47, no. 12, p. 1529–1533, Dec. 2000.

[69] P. Saeung and P. P. Yupapin, "Generalized analysis of multiple ring resonator filters: Modeling by using graphical approach," *Optik*, vol. 119, no. 10, pp. 465-472, Dec. 2006.

[70] W. Liu, M. Li, R. S. Guzzon, E. J. Norberg, J. S. Parker, L. A. Coldren and J. P. Yao, "A microwave photonic temporal integrator based on an InP-InGaAsP integrated tunable coupled ring," in *IEEE International Topical Meeting on Microwave Photonics*, Alexandria, Virginia, USA, Oct. 28-31, 2013.

[71] D. G. Rabus, Integrated Ring Resonators: The Compendium, Springer, 2007.

[72] J. Heebner, R. Grover and T. Ibrahim, Titre Optical Microresonators: Theory, Fabrication, and Applications, New York: Springer, 2008.

[73] E. J. Norberg, R. S. Guzzon, J. S. Parker, S. P. DenBaars and L. A. Coldren, "An InGaAsP/InP integration platform with low loss deeply etched waveguides and record SOA RF-linearity," in *ECOC*, Geneva, 2011.

[74] W. Liu, M. Li, R. S. Guzzon, E. J. Norberg, J. S. Parker, L. A. Coldren and J. P. Yao, "A photonic integrated fractional Hilbert transformer with continuous tunability," in *Optical Fiber Communication*, San Francisco, 2014.

[75] L.-C. Tsai and H.-S. Fang, "Design and implementation of second-order microwave integrators," *Microw. And Opt. Tech. Lett.*, vol. 53, no. 9, pp. 1983-1986, Sep. 2011.

[76] C.-W. Hsue, L.-C. Tsai and K.-L. Chen, "Implementation of first-order and second-order microwave differentiator," *IEEE Trans. Microw. Theory Tech.*, vol. 52, no. 5, p. 1443–1447, May 2004.

[77] K. T. K. &. J. B. Goda, "Serial time-encoded amplified imaging for real-time observation of fast dynamic phenomena," *Nature*, vol. 458, no. 7242, p. 1145–1149, Apr. 2009.

[78] C. Madsen and J. Zhao, Optical Filter Design and Analysis: A Signal Processing Approach, New York: Wiley, 1999.

[79] R. Parmentier and M. Lequime, "Substrate-strain-induced tunability of dense wavelength-division multiplexing thin-film filters," *Opt. Lett.*, vol. 28, no. 9, pp. 728-730, May 2003.

[80] H. Shahoei, D. Xu, J. Schmid and J. P. Yao, "Photonic fractional-order differentiator using an SOI microring resonator with an MMI coupler," *IEEE Photon. Technol. Lett.*, vol. 25, no. 15, pp. 1408-1411, Aug. 2013.

[81] G. Roelkens, L. Liu, D. Liang, R. Jones, A. Fang, B. Koch and J. Bowers, "III-V/silicon photonics for on-chip and intra-chip optical interconnects," *Laser Photon. Rev.*, vol. 9999, no. 1, pp. 1-29, Jan. 2010.

[82] Z. Wang, B. Tian, M. Pantouvaki, W. Guo, P. Absil, J. V. Campenhout, C. Merckling and D. V. Thourhout, "Room-temperature InP distributed feedback laser array directly grown on silicon," *Nature Photon.*, vol. 9, no. 10, pp. 837-842, Oct. 2015.

[83] A. Gonzalez, J. A. Belloch, F. J. Martinez, P. Alonso, V. M. Garcia, E. S. Quintana-Orti, A. Remon and A. M. Vidal, "The impact of the multi-core revolution on signal processing," *Waves,* vol. 2, pp. 74-85, 2010.

[84] J. L. Horner, Optical Signal Processing, San Diego: Academic Press, Inc., 1987.

[85] H. Sunnerud, M. Karlsson and P. A. Andrekson, "Analytical theory for PMD-compensation," *IEEE Photon. Technol. Lett.*, vol. 12, no. 1, p. 50–52, Jan. 2000.

[86] W. Liu and J. P. Yao, "Photonic generation of microwave waveforms based on a polarization modulator in a Sagnac loop," *J. Lightwave Technol.*, vol. 32, no. 20, pp. 3637-3644, Oct. 2014.

[87] J. P. Yao, "Microwave photonics," *J. Lightw. Technol.*, vol. 27, no. 3, pp. 314-225, Feb. 2009.

Appendix

1. Layout of the SOI Devices.

1.1 The passive photonic temporal differentiator

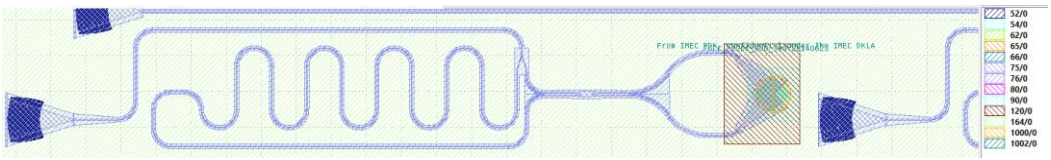

1.2 The active photonic temporal differentiator

2. Equations.

2.1 Derivation of (3-1)

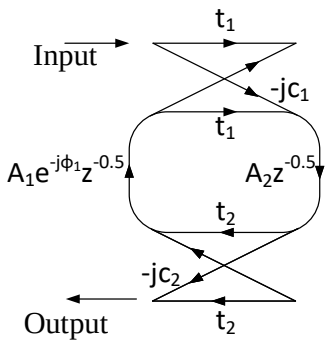

Fig. A-1. Signal flow graphs of a single add/drop ring rings [69].

As shown in Fig. A-1, there is only one forward path transmittance from the input to the output for the drop port and this forward path also touches loop $t_1 t_2 A_1 A_2 z^{-1}$,

we have the delta [69] given as $-c_1c_2A_2z^{-1/2}$. Thus, the transfer function can be written as

$$H_1(z) = -\frac{c_1c_2A_2z^{-1/2}}{1-t_1t_2A_1A_2z^{-1}} \tag{A-1}$$

As we have $z = e^{j\omega\tau}$, (A-1) can be rewritten as

$$H_1(z) = \frac{c_1c_2A_2e^{-\frac{1}{2}j\omega\tau}}{1-t_1t_2A_1A_2e^{-j\omega\tau}} \tag{A-2}$$

By multiplying $e^{-\frac{1}{2}j\omega\tau}$ on both the denominator and numerator, we have

$$H_1(z) = \frac{c_1c_2A_2}{e^{\frac{1}{2}j\omega\tau} - t_1t_2A_1A_2e^{-\frac{1}{2}j\omega\tau}} \tag{A-3}$$

2.2 Derivation of (3-2)

$$\begin{aligned} H_1(\omega) &= \frac{c_1c_2A_2}{e^{\frac{1}{2}j\omega\tau} - e^{-\frac{1}{2}j\omega\tau}} \\ &= \frac{c_1c_2A_2}{2j\sin\left[\frac{1}{2}(\omega-\omega_0)\tau + m\pi\right]} \end{aligned} \tag{A-4}$$

Assuming that m=0, we have

$$H_1(\omega) = \frac{c_1c_2A_2}{2j\sin\left[\frac{1}{2}(\omega-\omega_0)\tau\right]} \tag{A-5}$$

For a small $(\omega-\omega_0)\tau$, the $\sin\left[\frac{1}{2}(\omega-\omega_0)\tau\right] \approx \frac{1}{2}(\omega-\omega_0)\tau$, thus

$$H_1(\omega) = \frac{c_1 c_2 A_2}{2j \sin\left[\frac{1}{2}(\omega - \omega_0)\tau\right]} \approx \frac{c_1 c_2 A_2 / \tau}{j(\omega - \omega_0)} \tag{A-6}$$